Master Thesis Report

Large-Eddy Simulation of a Floating Offshore Wind Turbine with imposed motion

by

Robin Combette

to obtain the degree of Master of Aerospace Engineering
with a profile in Aerodynamics
at the Delft University of Technology,

Student number: 5596661

Supervisor: Axelle Viré

Date: September 1, 2023

TU Delft

Abstract

As the urge to decarbonise the energy field becomes increasingly important, a growing interest is shown in wind turbine technologies. In particular, the past few years have seen the development of floating offshore wind turbines for applications in deep waters.

In addition to the harsher environment they are facing, these wind turbines are mounted on floaters and therefore experience motions in the six additional degrees of freedom. As a result, this greatly alters their aerodynamic behaviour. The flow surrounding the rotor gains in complexity, becoming highly unsteady and three-dimensional. Thus, its resolution by numerical means calls for high-fidelity methods such as Large-Eddy Simulations (LES).

The objective of this study is to numerically impose single and coupled motions in the pitch and surge directions on a scale rotor of the DTU 10MW. This scale model was used for an experimental campaign within TU Delft, and particular interest is given to the comparison of the loads obtained. Additionally, numerical simulations permit access to further information, such as the radial distribution of the loads or the wake development.

For this purpose, the LES code YALES 2 is used, implemented with an actuator line approach capable of dealing with imposed motions. Both 1-DOF and 2-DOF harmonic motions are imposed in the pitch and surge directions. Different reduced velocities and frequencies are considered.

On single-imposed surging motion, the loads are found to be well in accordance with the quasi-steady theory (QST), even at high frequency, where much larger fluctuations were encountered during the experiment. Particular phenomena are also captured in the wake, such as the formation of vortex rings when the frequency is sufficiently high. Similar comments are made for 1-DOF pitching. Finally, for combined pitch/surge motions, the loads are also in accordance with the QST predictions made from the 1-DOF results. The influence of each motion on the wake's development is also discussed.

Keywords: Floating offshore wind turbine (FOWT), Large-eddy simulation (LES), Actuator line method (ALM), Coupled imposed motions, pitch, surge

Contents

List of Figures

List of Tables

List of Symbols and Abbreviations

A	Amplitude of motion (index s for surge, p for pitch)	[m or °]
A_R	Actuator disc area	[m^2]
c	Chord length	[m]
C_d	Drag coefficient	[-]
$C_{D,N}$	Nacelle drag coefficient	[-]
$C_{D,T}$	Tower drag coefficient	[-]
C_l	Lift coefficient	[-]
$C_{L,N}$	Nacelle lift coefficient	[-]
$C_{L,T}$	Tower lift coefficient	[-]
c_N	Nacelle width	[m]
C_P	Power coefficient	[-]
C_S	Smagorinsky's constant	[-]
C_T	Thrust coefficient	[-]
D	Rotor diameter	[m]
$D_{e,N}$	Nacelle equivalent diameter	[m]
D_t	Tower diameter	[m]
f	Motion frequency (index s for surge, p for pitch)	[Hz]
f_{AL}	Force at actuator line	[N]
f_r	Motion reduced frequency	[-]
K_{VT}	Partial derivative thrust w.r.t. rotor velocity	[-]
lc	Base cells width on coarse mesh	[m]
L_i	Length domain in $i-th$ direction	[m]
L_N	Nacelle length	[m]
L_T	Tower length	[m]
M	Pope's quality criterion	[$-$]
N_{AL}	Number of AL elements	[-]
N_{grid}	Number of grid elements	[-]
P	Power	[W]
r	Radial position along blade span	[m]
R	Rotor radius	[m]
Re	Reynolds number	[-]
St	Strouhal number	[-]
T	Thrust force	[N]
T_0	Steady-state thrust force	[N]
U_{cor}	Corrected wind tunnel velocity	[m/s]
U_f	Velocity far downstream streamtube	[m/s]
U_p	Platform motion velocity at rotor	[m/s]
U_R	Velocity at actuator disc	[m/s]
U_∞	Freestream velocity	[m/s]
V_{eff}	Effective velocity at blade element	[m/s]
α	Angle of attack	[°]
$\overline{\Delta}$	Filter width	[m]
Δ_{AL}	Actuator line's element width	[m]
Δ_g	Grid width near actuator lines	[m]
ΔV	Variation in rotor speed	[m/s]
ΔV^*	Motion's reduced velocity	[-]
ΔT	Amplitude of variation in thrust	[N]
ΔP	Amplitude of variation in power	[W]
$\Delta\Phi$	Pitch/surge phase shift	[°]
ϵ	Smearing parameter	[m]
ϵ_i	Wind tunnel correction factor	[-]
λ	Tip-speed ratio	[-]
μ	Air dynamic viscosity	[$Pa.s$]
ν	Air kinematic viscosity	[m^2/s]
ν_{SGS}	SGS eddy viscosity	[m^2/s]
ρ	Air density	[km/m^3]
ϕ	Phase shift loads/motion (index T for thrust, P for power	[°]
Ω	Rotor angular velocity	[rad/s]

ALM	Actuator Line Model
AoA	Angle of Attack
BEM(T)	Blade Element Momentum (Theory)
CFD	Computational Fluid Dynamics
CFL	Courant–Friedrichs–Lewy
DNS	Direct Numerical Simulation
DOF	Degree Of Freedom
FOWT	Floating Offshore Wind Turbine
FVW	Free Vortex Wake
HAWT	Horizontal-Axis Wind turbine
LES	Large Eddy Simulation
NS	Navier-Stokes
PWS	Propeller Working State
QST	Quasi-steady Theory
RPM	Rotation Per Minute
SGS	Sub-Grid-Scale
TLP	Tension-Leg Platform
TWS	Turbulent Wake State
(u)RANS	(unsteady) Reynolds- Averaged Navier-Stokes eq.
VAWT	Vertical-Axis Wind turbine
VRS	Vortex Ring State
WWS	Windmill Working State

1 Introduction

1.1. The need for Floating Offshore Wind Energy

As the consequences of climate change become increasingly noticeable, policymakers are put under pressure to take measures in order to reach the objectives of climate neutrality set by the Paris agreements. Production of energy is a key issue, as the global energy system is the largest source of CO2 emissions [1, chapter 2]. Hence, renewable energies such as solar photovoltaic, hydropower or wind energy are to be massively deployed, enabling the share of renewable energy in total final energy consumption to pass from 19% in 2019 to 79% by 2050 [2].

The need for harvesting wind intervenes in that context. The sector is experiencing significant growth, notably due to reducing costs and societal pressure to limit fossil generation [1, chapter 6]. Wind energy is expected to be one of the largest generation sources by 2030, supplying 24% of total electricity needs [2].

Wind energy has particularly thrived onshore so far, but interest in offshore keeps increasing as it presents many advantages: stronger and more consistent wind resources, more space available, better social acceptance, etc. However, this comes at a higher cost, and the wind turbines are placed in a harsher environment. The 56 GW of cumulative installed capacity for offshore in 2021 (including 21 GW installed in 2021) are to be compared with the 769 GW of global onshore wind capacity [3]. According to the predictions of the Global Wind Energy Council (GWEC), the total offshore capacity will reach 370 GW by the end of 2031, falling short of the 380 GW 2030 target defined by GWEC and IRENA to be on track with the Paris agreements [3].

Offshore wind energy is principally installed as fixed-bottom turbines, but those are only economically viable for water depths up to 50-60 metres. However, the major part of coastal waters is deeper than that: according to the GWEC, ”80% of the world’s offshore wind resource potential lies in waters deeper than 60m” [4]. That issue has motivated the development of floating offshore wind turbines (FOWT) and a growing interest has been shown in the field. If the first ever FOWT was built in 2008 in Norway and the first floating wind farm in 2017 in the UK (pilot project with only a few turbines), the total floating capacity in 2021 is estimated at 121 MW [3]. This represents only 0.2% of the total offshore contribution in 2021, but the sector is new and expected to reach 6% of that share in 2030 [3] and much more later. Floating wind farms potentially offer additional environmental benefits compared with fixed-bottom designs due to the reduced impact on the seabed, even though the long-term ecological effects are still unknown [1, chapter 6].

1.2. FOWT technology

Therefore, floating offshore wind turbines represent a promising technology but also come with multiple new challenges, raised principally by the six additional degrees of freedom of the platform. Indeed, subjected to waves, current, wind, etc., the platform will move, and the motion will alter the performances of the rotor, inducing unsteady phenomena of complex nature such as changes in the working state of the rotor or interactions with its own wake.

Then, even though several prototypes and the first wind farms have been built, the technologies are not totally mature yet. There is still a need to prove they are economically viable in comparison with fixed

bottom wind turbines. Nonetheless, studies based on global cost analysis (construction, installation, etc.) tend to highlight the great and promising potential [5]. Indeed, prices for energy are expected to be comparable to the fixed-bottom ones [6]. In order to confirm these studies, multidisciplinary optimisation tools are still required, enabling the optimisation of the floaters, for which construction and installation costs are determining factors [6].

This necessary multidisciplinary approach requires the development of low- to mid-fidelity models as well as high-fidelity simulations of each specific component in order to validate the methods and the results. Concerning the components, FOWT can be divided into three substructures: the rotor+nacelle assembly harvesting the wind energy and converting it into electricity, the floating platform supporting the previous assembly with the tower, and the mooring system maintaining the whole attached to the seabed.

First, on the floating platform, the research for the best floater has led to the investigation of many different designs. They can be divided into four categories: spar-buoy, semi-submersible, tension-leg (TLP), and barge platforms (see Figure 1.1). Each type of floater has its own characteristics (water depth required, dynamic response to waves, installation, etc.) and is generally associated with one type of mooring and anchoring system. A review of the pros and cons of each technology can be retrieved in the work of Barooni et al. [7] or in the report from GWEC [4].

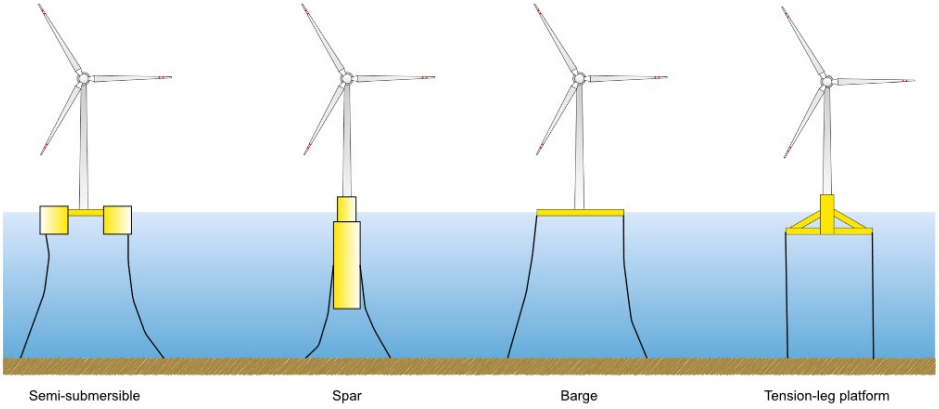

Figure 1.1: Different floater types: (from left to right) Semi-submersible, spar buoy, barge, tension-leg platform (TLP), [8]

On the rotor design, the particular conditions it experiences on the floater tend to question whether the classical three-blade horizontal-axis wind turbine (HAWT) is the most adapted. Particular interest has been shown in vertical-axis wind turbines (VAWT) due, notably, to their low centre of gravity. However, the three-blade HAWT is the most mature design, and the one that concentrates most of the current research.

In the later work, the focus will remain on the rotor and, in particular, on the classic three-blade HAWT design.

1.3. Objectives

The work conducted will try to answer the following main research question:

How do high-fidelity large-eddy simulations compare with experimental and low- to mid-fidelity models for the aerodynamic behaviour of a FOWT subjected to two degrees of freedom floating motions?

In order to do so, five sub-questions will be addressed:

- Is it feasible to model FOWTs subjected to coupled floating motions with large-eddy simulations using YALES2 in combination with an actuator line approach?

  If fixed-bottom wind turbines have already been simulated using YALES with actuator lines multiple times, such as in the work of Benard et al. [9], only one application on FOWTs has been published so far [10], without much detail on the model. Independently of the aerodynamic models, only a few studies focused on coupled floating motions have been performed.

- What are the discrepancies between large-eddy simulations and low- to mid-fidelity models for the behaviour of a FOWT subjected to coupled floating motions?

  Low- and mid-fidelity models such as BEM or FVW are extensively used and available within the well-known OpenFAST simulation tool. Therefore, it is interesting to compare and validate the results with such models, and in particular with the work of Ramponi [11] for coupled floating motions.

- How well are large-eddy simulation results comparable with experimental results for the unsteady behaviour of FOWTs?

  Experimental results are an essential source of validation, but only a few test campaigns for FOWT are available due to their complexity. However, an experiment was conducted at TU Delft, with the aim of providing results for both single and coupled floating motions on a scale model of the DTU 10MW turbine.

- Is it possible to obtain local and detailed insight into the airflow at blade level using actuator lines in combination with LES?

  Whether lower-fidelity models or an experimental approach are used, it is often challenging to obtain detailed results at the blade level, such as unsteady oscillations of the angle of attack. Yet, this is crucial information as it is one of the main parameters for control strategies and is associated with load constraints and unsteady responses.

- Can the near-wake behaviour and its main features be captured in response to the imposed motions?

  One great advantage of using CFD is the possibility of easily accessing the development of the wake and its characteristics downwind of the rotor. In particular, the near and mid-wake need to be properly resolved to compute accurate loads.

1.4. Report organisation

After a brief literature review on FOWT aerodynamics and the numerical model used in this study in chapter 2, the later model is described with the overall methodology in chapter 3. Then, the method is validated in chapter 4 before being applied to one degree of freedom motions, namely surge (chapter 5) and pitch (chapter 6). Finally, coupled pitch/surge motions are investigated in chapter 7. Conclusions of the study are drowned in chapter 8, as well as recommendations on possible works to be performed to continue the analysis.

2

Literature review

2.1. Rotor-induced motion

The key challenge for FOWT is to address the six additional degrees of freedom and their impact on the turbine's performance.

2.1.1. FOWT dynamics

The characterisation of the dynamics of an entire FOWT is a complex matter. First, the turbine is subjected to both external loads from its harsh environment (non-uniform and unsteady wind, waves and currents, etc.) and internal loads from its different components. Each of these components has its own behaviour, and they interact with each other in a coupled manner. The floater's motion induced by the waves can, for example, influence the rotor response, which will then alter the motion of the floater, etcetera. The characterisation of such a behaviour calls for partially or fully coupled approaches, which are generally based on low- to mid-fidelity models for cost issues. OpenFAST (formerly FAST) [12] acts as a reference for such models and is widely used to obtain the behaviour of FOWTs.

Such coupled models, as well as experimental results, permit the characterisation of the dynamic response of a FOWT to a certain loading and, in particular, the motion in the six additional degrees of freedom (DOF). The three translational (surge, sway, and heave) and three rotational (pitch, yaw, and roll) motions are indicated on the Figure 2.1. These DOF can greatly affect the rotor's performance as well as the stability provided by the platform and mooring system, therefore, it is crucial to know what the structure's response will be to the solicitations it might face during its lifespan.

The typical response of a FOWT is generally characterised by the amplitude and frequency of the typical motion in each of the six DOFs and is mainly dependent on the type of floater. In order to estimate these typical responses, several experimental campaigns and multiple numerical simulations have been performed. Imposing wave and wind conditions (generally perpendicular to the rotor), they study the resulting motion and offer orders of magnitude for the typical motion of a certain platform. Comparisons between the responses of the different types of floaters presented earlier can be retrieved in the work of Sebastian and Lackner [14], Goupee et al. [15] or Robertson et al. [16]. In brief, the surge and sway motions are the principal translational ones, with the barge and the semi-submersible experiencing such motions at particularly low frequencies. The TLP is very stiff to heave excitation, while the spar-buoy can experience larger motions. The TLP is also very stiff to rotational motions, with other types of platforms being particularly sensitive to pitch oscillations.

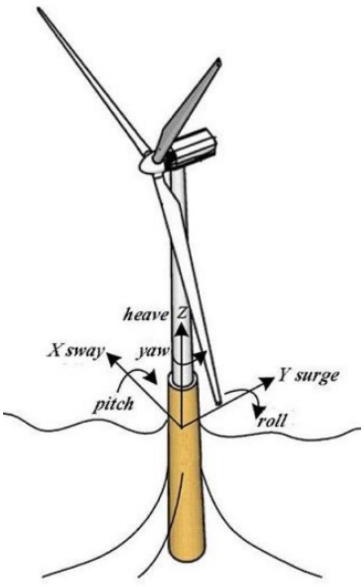

Figure 2.1: 6-DOF motions of a wind turbine floating foundation, [13]

2.1.2. Imposed motion

Ideally, fully coupled simulations should be run for FOWT, including hydrodynamics (platform, mooring lines), aerodynamics (rotor but also emerged structures), and elastic responses (tower, blades, etc.). Such simulations generally call for low- to mid-fidelity models to keep their costs reasonable. Thus, in order to study specific behaviours more precisely, uncoupled and partially-coupled simulations are also used. In order to study the aerodynamic behaviour of the rotor with high-fidelity tools, a few models including fluid-structure interaction (FSI) have been developed [17]–[19] enabling tip deflection, for instance. A LES formulation has also been used to replace the aerodynamic module in OpenFAST and benefit from both a coupled approach and high-fidelity CFD [20]–[23]. However, in rotor aerodynamics, the choice to impose a certain motion is generally preferred for the sake of simplicity.

Indeed, the coupled models are complex, and the use of high-fidelity models is limited by the computational power available. Thus, when the main subject of interest is the rotor aerodynamics for a FOWT, a motion is generally directly prescribed to the geometry. Those prescribed motion characteristics are mostly obtained from tests in wave tanks on scaled models and thorough numerical analysis, and mostly depend on the type of floater considered. Without the need for complete coupling, the difficulty is greatly reduced, and a great variety of aerodynamic models of different complexity and fidelity can be used. However, there is no real-time interaction between aerodynamic and hydrodynamic responses accounted for.

As will be discussed in the next section, surging and pitching are found to have the greatest impact on the rotor's aerodynamic behaviour. They both have been imposed and studied extensively in the literature in a single manner, with many different numerical methods.

If all six degrees of freedom are to be studied, Ribeiro et al. [24] claim that conclusions can be drawn by only studying surge, yaw, and sway motions. Indeed, they state that pitch is only a combination of these three DOFs and that rolling and heaving are similar to swaying from a rotor's point of view.

More rarely, combined motions are also imposed on wind turbines. That is the case of Ramponi [11] who studied pitch-surge, pitch-yaw, and surge-yaw motions using OpenFAST, and notably highlighted the little effect of yawing as well as the importance of the phase difference between surge and pitch motions. A combined surge-pitch motion was also imposed in the work of Lin et al. [25] who found greater power fluctuations for certain phase differences as well. In Chen et al. [26], such a combined motion was found to reduce the mean power generated. They also highlighted the fact that a combined motion induced complex responses that were different from a simple superposition of the responses obtained for the single cases.

2.2. Rotor behaviour

Compared to a fixed turbine, the platform motion will create highly unsteady conditions for the FOWT rotor. Hence, its performance and dynamics will be significantly altered. This section aims at discussing the main aerodynamic phenomena induced by the floater motion.

As mentioned earlier, the focus is on conventional three-bladed horizontal-axis wind turbines. Furthermore, the main interest is in isolated rotors and not wind farms.

2.2.1. Power production

The performance of a wind turbine rotor is generally described by the thrust and the power generated, or their associated non-dimensional coefficients. On a fixed rotor, they are usually considered to be steady (assuming steady wind conditions). However, FOWTs experience significant motions, and unsteadiness in the loads is therefore expected.

On the motions, there is a clear consensus in the literature on the fact that surging and pitching have the biggest impact on the rotor's performance. This is not surprising, as they are the only two motions in the same direction as the incoming wind, and as the different floaters all experience such motions. The works of Tran et al. [27], [28], for example, highlight how those motions greatly alter the loads and how they become unsteady. In comparison, they estimate that the unsteady thrust and power coefficients are 12 to 16 times more sensitive to pitching than yawing, for the same frequency and amplitude of motion.

Even if some studies suggest a decrease in the mean power for imposed surge and pitch motions (Chen et al. [26], even greater loss for coupled motions) or for fully coupled analysis [18], the consensus is rather on an increase in the mean power and a slight decrease in the mean thrust for the two motions.

Such observations can be found in Lienard et al. [29], Shen et al. [30], Amaral et al. [31], Fang et al. [32] and others. Lienard et al. [29] highlight that the majority of the power gain corresponds to the forward phase, for both motions, with a maximum when the rotor comes back to its initial position. Concerning the coupling of the motions (pitch-surge), Ramponi [11] shows that those power gains can possibly be zeroed depending on the phase difference between the two motions. Then, Amaral et al. [31] state that those power gains tend to increase with the amplitude and frequency of both motions. A similar statement can be found for pitching in Fang et al. [32].

Finally, the power oscillations also depend on whether the rotor is controlled or not. If it is, an increase in the power generated above the rated power will not be allowed, which can finally result in an overall power generation loss.

2.2.2. Wake

The wake refers to the region downwind of the rotor where the flow is altered compared to the free stream flow surrounding this region. As a consequence of the rotor extracting energy from the flow, a velocity deficit and increased turbulence intensity can be observed in this region. As it extends downwind, the velocity deficit tends to decrease while the wake cross-sectional area increases.

More precisely, the wake can be divided into two sub-regions: the *near-wake* and the *far-wake*. The former is located right downwind of the rotor and can extend to 2 or 4 times the rotor diameter, while the latter is its continuity further downwind. If the near-wake characteristics are mostly determined by the rotor geometry (blades, nacelle, hub, etc.) and thus are greatly complex, 3D, and heterogeneous, the far-wake in turn is less dependent on precise features [33]. Indeed, the former region can generally be well predicted using only the flow conditions and the general performance of the rotor (thrust and power). Important features in the wake are the tip and root vortices generated by the difference in pressure between the suction and pressure sides of each blade. They rotate with the wake as a consequence of the rotor motion and convey a significant part of the wake energy. Hub-vortices are also to be observed in the central region of the wake. Those vortices can be clearly observed in the near-wake but not really in the far-wake as they dissipate.

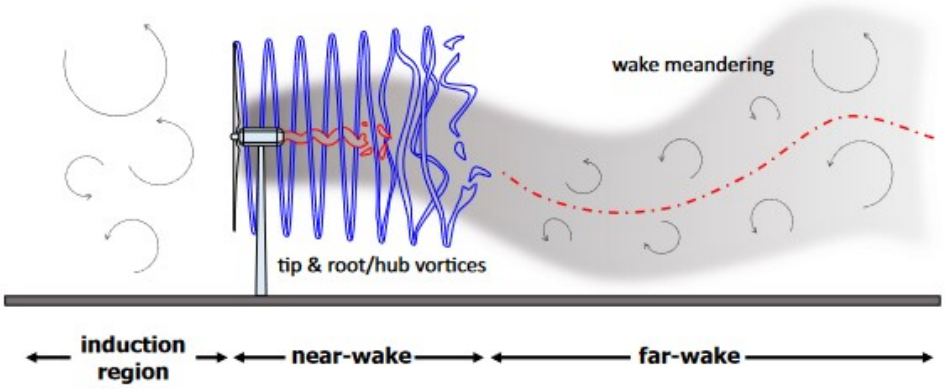

Figure 2.2: Schematic representation of the instantaneous flow field near a wind turbine rotor, [33]

For a FOWT, it is expected that the rotor motions will alter the wake characteristics compared to a fixed rotor. Similarly to rotor performances, there is a clear consensus that the wake strength is mostly affected by surging and pitching motions, compared to other motions such as yawing [27], [28]. Experimental results obtained for surge motion within the UNAFLOW project have shown that the tip vortices' travel speeds are altered by the surge motion, that the wake becomes asymmetric, but also that surging does not significantly impact the shape of the velocity deficit [34]. For pitch motion, other experimental results obtained by Rockel et al. [35] showed an upward shift of both the mean flow and its fluctuations.

When the FOWT moves backward due to pitch or surge solicitations, there is a risk that the rotor interacts with its own wake. Due to the higher level of turbulence in this region and the presence of tip and root vortices, this can generate significant fatigue loads, for instance. Evidence of such blades/wake interactions has been found by Tran et al. [28] for surging and by Matha et al. [36] for both pitch and surge motions.

As mentioned earlier, Fontanella et al. [34] have found, thanks to experiments, that the wake is asymmetric due to the motions. Similar results were found numerically by Ye et al. [37]. They also highlighted the impact of the tower wake on the asymmetry of the velocity deficit profiles. Indeed, the tower wake is conveyed upward by the rotational wake, then mixed with the rotor wake, thus breaking symmetry.

The centreline and contours of the wake are not necessarily steady, even for fixed-bottom wind turbines. When large turbulent eddies are present in the incoming flow, *wake meandering* can be observed [33]. It corresponds to the fluctuations of the whole wake around the time-averaged wake centreline. In the context of FOWT, the motions could also be sources of wake meandering. Indeed, roll motion was found to significantly trigger wake meandering, especially for low turbulence inflow [38]. Furthermore, vertical meandering was also observed due to pitching motion in Johlas et al. [21], [22]. On the other hand, the experimental results obtained by Garcia et al. [39], showed no significant impact of surging on wake meandering, although traces of the motion could be found in the far wake by means of a spectral analysis. There exist several methods in order to numerically track the wake centreline. Coudou et al. [40] investigated a few of them and tracked wake trajectories.

As wind turbines are generally placed in wind farms, wake recovery is a key parameter. Indeed, the faster the wake recovery, the closer the turbines can be placed, resulting in greater production in the same area. Some studies tend to show that, due to greater dissipation, FOWTs present faster wake recoveries. Indeed, such a statement was observed by Cheng et al. [18] for a fully-coupled simulation. Experimental results on a porous disc by Schliffke et al. [41] lead to the same conclusion for surging. Finally, Duan et al. [42] qualify the statement for surge motions, highlighting the impact of the surge period. Indeed, for short surge periods, the wake recovery is found to be slower, while for longer periods, the wake recovery is faster, and two FOWT can be placed closer together in a wind farm design. The amplitude of the surge motion, on the other hand, is not found to have a significant impact on wake recovery.

Some elements constituting the wake and discussed in this present section are illustrated on Figure 2.2.

2.2.3. Unsteady aerodynamics

When talking about unsteady aerodynamics, two different scales need to be distinguished:

- The dynamic inflow at the **rotor scale**, consequence of an unsteady inflow, an unsteady wake due to turbulence or rotor motion, for example.
- Unsteady airfoil aerodynamics at the **blade section scale**, induced by unsteady variations of the apparent angle of attack (AoA).

Those two scales are not necessarily coupled, one can be steady while the other is unsteady. In addition, the unsteadiness can be either periodic or aperiodic.

Airfoil scale

For the particular case of a periodic perturbation over an airfoil, the so-called *reduced frequency* k is defined as follows:

$$k = \frac{\omega c}{2V_\infty} \tag{2.1}$$

Wherein, ω is the perturbation frequency ($[rad/s]$), c the airfoil chord length, and V_∞ the reference wind speed. This dimensionless parameter is often used to categorise the degree of unsteadiness of a flow subject to a periodic disturbance, and the ranges are usually given as follows:

- $k = 0$, the flow is steady
- $0 < k \leq 0.05$, the flow is quasi-steady
- $0.05 < k \leq 0.2$, the flow is unsteady
- $k > 0.2$, the flow is highly unsteady

For a wind turbine, and by considering only in the reference velocity the free wind speed U_∞ and the rotor speed Ω as described in Sebastian and Lackner [14], the reduced frequency becomes:

$$k(r) = \frac{\omega c(r)}{2\sqrt{U_\infty^2 + (r\Omega)^2}} \tag{2.2}$$

Wherein r is the radial position along the span. Thus, a wind turbine blade whose chord length and reference wind speed vary along its span, will experience different levels of unsteadiness: the flow at the root could be unsteady while the one at the tip is steady, for example.

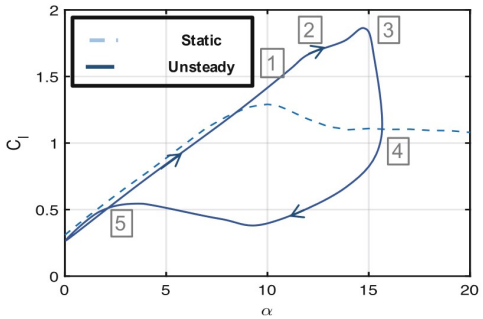

Figure 2.3: Example of lift polar when airfoil subjected to dynamic stall, [43]

It is common to find people referring to unsteadiness at the airfoil scale and to dynamic stall interchangeably. However, dynamic stall is not the only source of unsteadiness, as this level and a fully attached flow around an airfoil can totally generate unsteady behaviour [44]. Dynamic stall is a specific phenomenon, that occurs on lifting surfaces when subjected to pitching, plunging, or other motions during which the effective angle of attack exceeds the static stall angle. It is a consequence of the boundary layer development over the airfoil and the interaction with shed vortices, which creates a delay in separation, and results in a so-called *hysteresis effect*: the relation between the lift generated and the angle of attack is no longer unique for unsteady and quasi-steady solicitations (see example in Figure 2.3). Visbal and Garmann [45] offered a detailed description of the phenomenon over an airfoil by means of high fidelity numerical results. Examples of unsteady polars representing the hysteresis effect can be found in Bayati et al. [46] with the experimental results obtained within the framework of the UNAFLOW project. Furthermore, the strength of this effect (i.e. the difference in amplitude and the range of AoA concerned) is increased with increasing motion frequency [34]. For more details on dynamic stall in wind energy airfoils, one can refer to Santos Pereira [43].

Rotor scale

At rotor scale, Bayati et al. [47] introduced a similar indicator of unsteadiness, the wake reduced velocity:

$$V_W^* = \frac{U_\infty}{2fR} \tag{2.3}$$

Wherein f is the motion frequency and R the rotor radius. The higher the wake reduced velocity, the steadier the flow at the rotor, with a limit around $V_W^* = 5$ to delimit unsteady to quasi-steady flows.

For a FOWT, the sources of unsteadiness on both scales are numerous. Among these sources, figure the ones also present for fixed rotors: unsteady inflow due to wind turbulence, due to the presence of an upstream turbine and its wake, yawed conditions, or the so-called *tower shadow*. This latter phenomenon refers to the particular interaction between the tower and the rotor blades as they pass by the tower. The induced velocities of the tower wake in particular alter the circulation around the blade sections in this particular region, which is crossed once every rotation by each blade. Hu et al. [13] quantified the impact of this phenomenon for different rotor motions.

For floating wind turbines, the rotor will also experience motion, creating unsteady conditions. Again, the two motions with the greatest impact on unsteadiness are found to be surging and pitching [27], [30], [48]. The latter motion was found to particularly promote the occurrence of dynamic stall with significant variations of angle of attack when blade pitch is fixed [27], [49]. Fang et al. [32] also made such an observation and added that pitching motion can lead to stall flutter. This phenomenon being the oscillation in and out of dynamic stall which raises integrity issues due to the great fatigue loads associated with it. The rotor motion is not only directly responsible for unsteady inflow conditions but also for time-varying wake shapes that also favour unsteady behaviour. Shen et al. [30] stated that this unsteady wake shape, as well as shed vorticity (created by unsteady variations of circulation around the airfoil), are the two greatest sources of unsteadiness during surge motion.

During the experiments investigating the surge response and conducted as part of the UNAFLOW project, they avoided the airfoil's unsteady behaviour by staying distant from the static stall angle of attack [34]. However, time variations in thrust force were still observed in response to the surge motion, as discussed in the previous section. This response was found to be in accordance with the quasi-steady theory (QST), in which the loads and wake respond instantaneously to the platform motion [10]. Previous works have shown that, following the QST, a first order linearization of the thrust can work for a certain range of amplitudes and frequencies [34], [50]. The thrust force T becomes:

$$T \simeq T_0 + K_{VT}\Delta V \tag{2.4}$$

Wherein T_0 is the steady-state thrust force, ΔV the variation in rotor speed and K_{VT} the partial derivative of thrust with respect to rotor speed.

The thrust variation can be divided into an amplitude term and a phase term as follows:

$$\Delta T = |\Delta T| e^{j\phi} \tag{2.5}$$

Wherein, the amplitude in quasi-steady theory becomes:

$$|\Delta T| = 2\pi f A K_{VT} \tag{2.6}$$

A and f are the amplitude and frequency of the 1 DOF motion, respectively. In addition, the phase shift with one-dimensional harmonic motion is $\phi = \pm 90°$ depending on the direction the motion velocity is defined.

Therefore, the thrust variation remains the same for identical motion at reduced velocities defined as:

$$\Delta V^* = \frac{\Delta V}{V_\infty} = \frac{2\pi f A}{V_\infty} \tag{2.7}$$

Previous works, and the experimental results obtained in the context of OC6 and UNAFLOW in particular, tend to highlight a good agreement with QST at low reduced frequencies [10]. This quantity is defined as:

$$f_r = \frac{fD}{U_\infty} \tag{2.8}$$

2.2.4. Rotor flow states

This section aims at investigating the notion of rotor working states, but first, the concept of actuator disc needs to be introduced via the one-dimensional momentum theory.

1D Momentum theory

First, a streamtube including the rotor is defined, delimiting four sections: the inlet, the outlet, and the two sections upstream and downstream of the rotor (respectively sections 1, 4, 2, and 3 on Figure 2.4). Then, the equations of conservation are applied to a flow inside the streamtube that is considered to be steady, inviscid, incompressible, and with a constant internal energy. Finally, the problem is considered one-dimensional, meaning that the pressure and the velocity are constant in the radial and azimuthal directions.

From the simplified equations, the thrust and the power can be expressed only with the pressures and velocities at the inlet, outlet, and rotor discs. If the velocity is continuous at the rotor, the model has the particularity to introduce a pressure discontinuity at this section. The resulting particular section at the rotor is the so-called *actuator disc*.

Furthermore, the (axial) induction factor a is introduced, giving the relation between the free stream velocity and the velocity at the rotor, as follows:

$$U_R = (1 - a)U_\infty \tag{2.9}$$

In the model, the velocity passing through the rotor disc is also the mean between the air speeds far upstream and far downstream:

$$U_R = \frac{1}{2}\left(U_\infty + U_f\right) \tag{2.10}$$

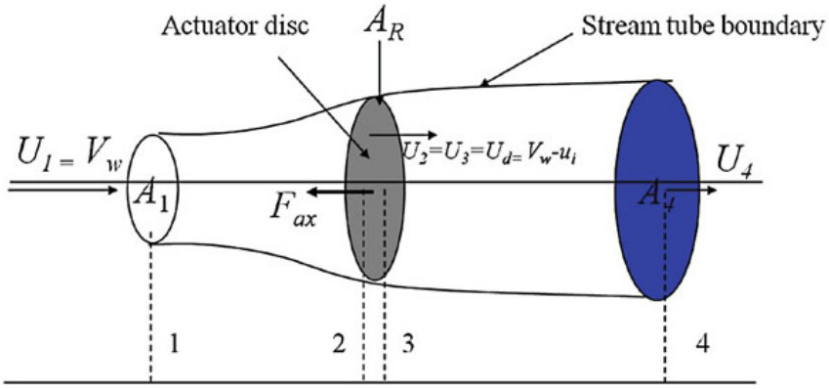

Figure 2.4: Streamtube with the axial velocities used in 1D momentum theory, [51]

Then, the non-dimensional thrust and power coefficients can be expressed w.r.t. a:

$$C_T = \frac{T}{\frac{1}{2}\rho A_R U_\infty^2} = 4a(1-a) \quad ; \quad C_P = \frac{P}{\frac{1}{2}\rho A_R U_\infty^3} = 4a(1-a)^2 \tag{2.11}$$

From Equation 2.10, it results that the velocity far downstream U_f is:

$$U_f = (1-2a)U_\infty \tag{2.12}$$

Thus, for $a > 0.5$, U_f becomes negative, corresponding to flow reversal, which is beyond the scope of the assumptions made, and the model does not stand anymore. To surpass this limit, the Glauert correction is generally used for highly loaded actuator discs, extending the relation for the thrust coefficient C_T for $0.5 \leq a \leq 1$.

Working states

Discussions on the different flow states experienced by the rotor first began with the observation of helicopters in descent that were having very unstable behaviours under certain conditions.

There are generally four different working states identified, namely the windmill state, the turbulent wake state, the vortex ring state, and the propeller state (see Figure 2.5). However, additional states are also frequently discussed, such as the propeller brake state.

Those different states can be briefly described as follows:

- *Windmill working state* (WWS): it is the normal mode of operation for a wind turbine in steady conditions, the rotor is extracting energy from the flow, and the stream-tube contracts upstream and expands downstream.
- *Propeller working state* (PWS): it is the normal mode of operation of an aircraft propeller in steady conditions. As opposed to windmill, it adds power to the flow, accelerating the flow and contracting the stream-tube downstream.
- *Turbulent wake state* (TWS): corresponding to highly loaded conditions, the flow starts to recirculate in the wake region, downstream of the actuator disc.
- *Vortex ring state* (VRS): vortex recirculation is observed at the tip, and the flow through the actuator disc is completely blocked.

Those working states are generally delimited w.r.t. the axial induction factor a such as presented in Figure 2.6 (from Sørensen et al. [52]). The propeller brake state is also represented, corresponding to conditions where power is added to the flow and a downwind thrust is created. Such a working state was never found to be relevant nor discussed for FOWT.

Even though the turbulent wake and vortex ring states are transient and unstable states [52], their possible occurrence is a major issue for wind turbines. First, the momentum balance equations used in the actuator disc model are broken down for those states. As most of the engineering models are

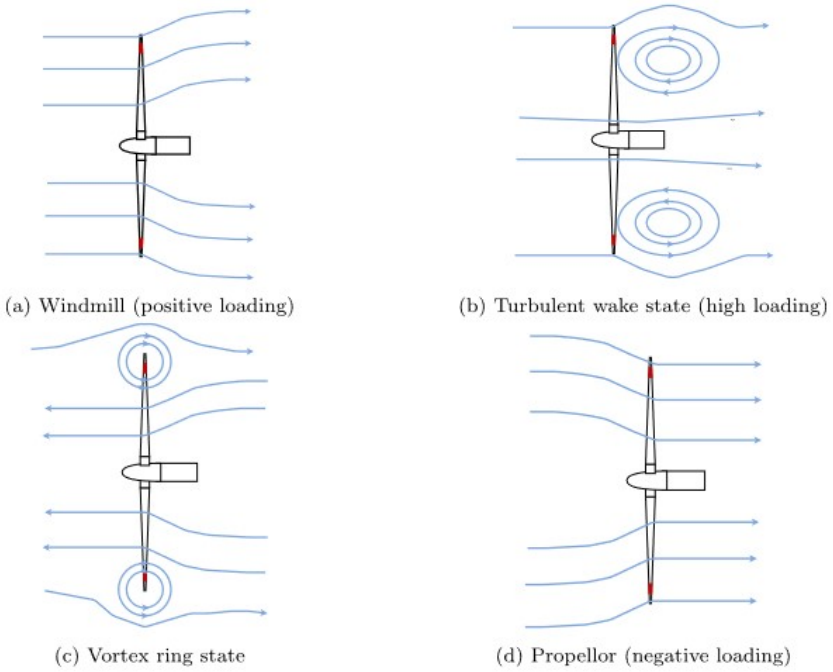

Figure 2.5: Modes of operation of an actuator at various loading conditions, [8]

based on these equations to evaluate the aerodynamic behaviour of wind turbine rotors, this could represent a challenging limitation for their use, calling for higher fidelity but also more expensive tools. Second, those two states are associated with higher fatigue loads, as a consequence of the increased turbulence level and the recirculating flows that induce vibrations and oscillations.

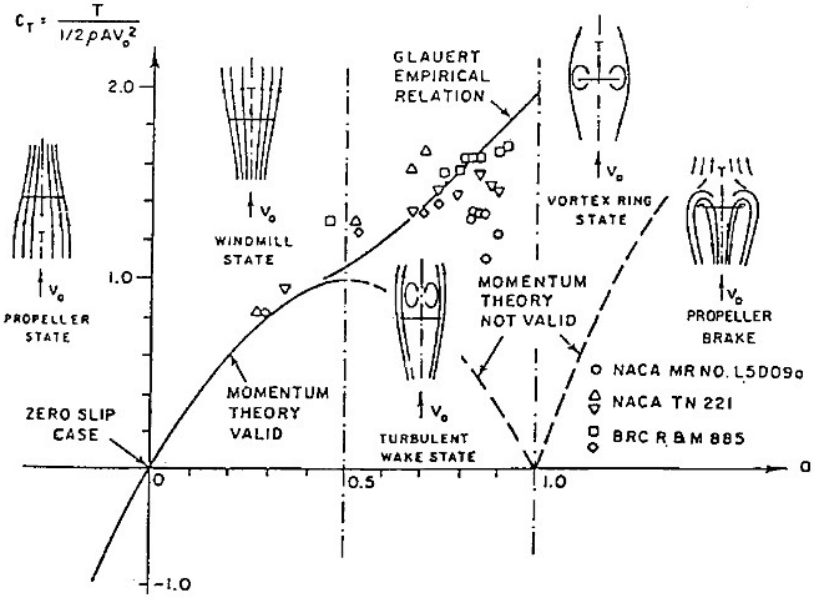

Figure 2.6: Thrust coefficient and rotor flow states w.r.t. the axial induction factor, [52]

In the context of FOWT, it is feared that the motions of the rotor can lead to a higher occurrence of these unstable states. In particular, when the turbine is moving downward due to pitching or surging, the rotor could interact with its own wake, leading to turbulent wakes or even vortex ring states for faster motions. If the rotor motion velocity were to surpass the wind speed, the rotor could enter the propeller working state.

Such a transition from WWS to PWS, through TWS and VRS was first imagined by Sebastian and Lackner [14], [49]. They detected the occurrence of the windmill and propeller working states for a combined surge-heave-pitch motion. To do so, they looked at the axial induction factor and associated a positive value with WWS, a negative one with PWS. They highlighted significant differences along the blades' span and noticed an increased PWS occurrence at outboard sections due to the pitching motion.

Leble and Barakos [48] studied the occurrence of TWS and VRS for a pitching rotor. They used an indicator commonly employed for helicopters in descending flights, which compares the so-called induced velocity at hover (a function of the thrust) with the normal velocity at the rotor plane. They detected the rotor to enter TWS and also VRS for large pitching amplitudes. The same conclusions based on the same indicator were made by Lienard et al. 2020 [29] for both surge and pitch motions. However, they were more cautious with the conclusion, calling for wake visualisation for confirmation and highlighting that the criterion uses the thrust coefficient, which is highly unsteady for FOWT (which is not the case for helicopters in quasi-steady descent as it was initially designed for). Such indicators based on the induced velocity at hover are multiples. Dong and Viré [53] compared two of them (Wolkovitch's and Peters' criteria) with the axial induction factor method to identify VRS occurrence. However, for the latter method, they used a modification proposed by Cruz and Atcheson [54] who introduced the platform motion velocity U_p in U_R formulation:

$$U_R = (1 - a)(U_\infty - U_p) \tag{2.13}$$

They observed significant differences between the three indicators. Later, they conducted a more detailed study for surge only, using the axial induction and the Wolkovitch criteria, and comparing with streamlines visualisation [55]. They were able to observe a cycle during the periodic surge motion as follows: windmill working state to vortex ring to propeller to vortex ring and windmill again (WWS -> VRS -> PWS -> VRS -> WWS). They stated that a turbulent wake state was not encountered during the cycle because, even if the flow was at times chaotic with recirculation in the wake, no increase in the thrust coefficient was observed. However, this could also be a limit of their potential, hence inviscid, method.

In addition, the flow visualisations highlighted that these changes in working states could be just local properties of the flow near the rotor and not global changes in the streamtube as encountered for helicopters. This is in line with the discussion made by Ferreira et al. [56] who claimed that no turbulent wake or vortex ring states occurred for FOWT. They stated that the working state changes, as originally defined, are not encountered in the context of FOWT but rather local changes are observed. For example, the rotor can appear to work in propeller mode while the streamtube as a whole is in its windmill state.

Therefore, debates on the definition and terminology of these states for FOWT applications are still ongoing. Yet, BEM methods, including dynamic models, are still found to provide accurate results [56] and the main discussion is rather on the amplitudes of load variations actually observed at the rotor. Indeed, whether it comes from high variations of angle of attack or blade/wake interactions, it is essential to know if negative values of thrust or power are achieved.

During surge motion, negative values of the thrust coefficient were observed by Kyle et al. [57]. In addition, differences along the blades' span were also observed. This was explained by looking more closely at the angle of attack which is directly related to the loads at the blade's level. When the rotor supposedly passes from WWS to PWS at a platform motion speed equal to the incoming wind velocity, the blade sections only experience the rotational velocity. Thus, at that precise moment, the AoA is equal to the collective pitch plus the twist angle, defining a limit to detecting this transition. Moreover, since the twist varies along the span, different conditions are observed, and the root region experiences propeller state as in Leble and Barakos [48]. Later, in the work of Kyle and Früh [58], they looked at the sign of both the thrust and power coefficients and proposed a quadrant visualisation. They also defined with this indicator two new states: a so-called *braking state* with power added to the flow and a torque applied against the rotation, which appears at the beginning of the windmill state, and a *quasi-windmill state* observed when leaving the propeller state and with similar characteristics to VRS in terms of power and thrust signs. During surge motion, they observed the following sequence: from windmill state ($T > 0$, $P > 0$) to braking state ($T > 0$, $P < 0$) to propeller state ($T < 0$, $P < 0$) to quasi-windmill ($T < 0$, $P > 0$) and back to propeller, braking, and windmill again. In addition, the visualisation of vortical structures in the flow showed interactions between the blades and the tip vortices during surging but

was not associated with VRS, which was believed not to be relevant for FOWT, even at the local level.

Similarly, Dong and Viré [55] also looked at variations of thrust coefficient and observed negative values of C_T as well. From their indicators, they associated those negative thrust values with VRS and PWS. In addition, the flow visualisations clearly showed local flow rehearsal at the rotor. They also looked at the radial distribution of the angle of attack through time, as in the work of Kyle et al. [57].

2.3. Key research projects

Some projects, by enabling the collaboration of several universities on the FOWT research, serve as references in the literature.

One of its main facilitators is the International Energy Agency (IEA). Through its wind tasks, and by regrouping and coordinating the main players in wind energy research (both academic and industrial), this organisation aims to support the deployment of wind energy. For floating applications, the Offshore Code Comparison Collaborative projects (OC3, OC4, OC5, and OC6) have played and still play a significant role in the critical evaluation of the current research. The OC5 project, for instance, has permitted the comparison of multiple numerical models with experimental results on the estimation of loads for a designed semi-submersible platform [16]. A similar comparison, but notably with a deeper focus on aerodynamic models, was performed within the latest one (OC6) [10], [59].

For the validation of their results in these campaigns, they extensively use the experimental results obtained within the UNAFLOW project [34], [46]. This experimental campaign has permitted to obtain the aerodynamic response of a scaled wind turbine subjected to single surge and pitch motions. Not only the loads were obtained during the motion, but also some wake information was obtained via hot-wire anemometry (HWA) and particle-image velocimetry (PIV) techniques.

2.4. Aerodynamic model

There exists a great variety of aerodynamic models used for FOWT, each of which has a different level of fidelity. Blade element momentum (BEM) based models are generally considered low-fidelity, potential approaches such as free vortex wake (FVW) mid-fidelity and computational fluid dynamics (CFD) simulations high-fidelity. Among the latest category, large-eddy simulations (LES) are particularly acute and adapted for the complex and unsteady flow around a FOWT. However, the complete resolution of the flow field calls for fine meshes around the blades and can lead to prohibitive computational costs. For that purpose, an actuator line method (ALM) in combination with LES is often preferred.

2.4.1. Actuator Line

In computational fluid dynamics, the domain is discretised and the Navier-Stokes (NS) equations are solved over the grid generated. However, in order to lower the computational cost of simulations, it can be chosen to model the impact of certain elements as the blades on the flow fields and not directly discretise the domain around them.

Formulation

The *actuator line model (ALM)* formulation was first introduced by Sørensen and Shen 2002 [60] and represents each blade by a discretised actuator line. At each blade section, the direction and velocity of the local incoming flow are evaluated according to blade element theory (see Figure 2.7). The effective inflow is affected by the freestream and rotational velocities, the axial and azimuthal induction factors, accounting for the non-uniform distribution of the loads over the actuator disc, and the potential rotor motion. The angle of attack α as seen by the airfoil is calculated from the effective velocity angle ϕ, the pitch and twist angles of the blade section ϵ. Finally, based on tabular airfoil data, lift and drag forces, as well as their projection (axial and inplane forces), are associated with each blade element via the corresponding angle of attack.

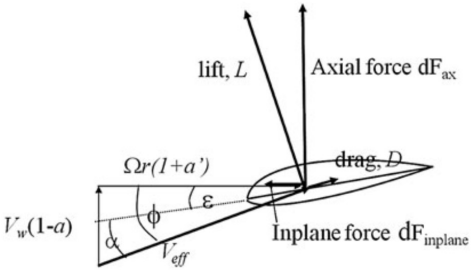

Figure 2.7: Blade element theory, [51]

Therefore, with projection, the force at each section is expressed as follows:

$$\vec{f_{AL}} = \frac{1}{2}\rho V_{eff}^2 c \left(C_l \vec{e_L} + C_d \vec{e_D}\right) \tag{2.14}$$

Wherein C_l and C_d are respectively the lift and drag coefficients, c the chord length, and V_{eff} is the local velocity in blade element theory (see Figure 2.7).

A drawback to this approach is the required accessibility of lookup tables for the blades considered. This method is also more complex and computationally demanding than other similar methods, such as the actuator disc one (ADM) but provides a more detailed representation of the loads (spanwise distribution and rotational effects). If complex phenomena such as the transition from laminar to turbulent or separation over the blades cannot be captured with ALM, root and tip vortices can, on the other hand, be generated.

The efficiency of ALM is no longer to be proved as it has already been used several times for FOWT applications [19]–[21] and multiple times on fixed wind turbines. In the context of FOWT, the unsteadiness of the inflow induced by the platform motion needs to be taken into account in the calculation of the blade loads. This is achieved by including the platform velocity within the blade element velocity triangle, such as proposed in the work of Cheng et al. [18].

Smearing

Once the loads are obtained at each segment along the actuator lines, they still need to be applied to the meshed domain. This important step is called the smearing of the forces. In order to maintain numerical stability, the body forces need to be distributed over several grid points and not only interpolated at the nearest grid point. This process is generally made by means of a convolution between the loads and a regularisation kernel η_ϵ:

$$f_\epsilon = f \circledast \eta_\epsilon \tag{2.15}$$

Wherein η_ϵ is generally taken in the form of a three-dimensional Gaussian function as follows:

$$\eta_\epsilon(d) = \frac{1}{\epsilon^3 \pi^{3/2}} \exp\left[-(d/\epsilon)^2\right] \tag{2.16}$$

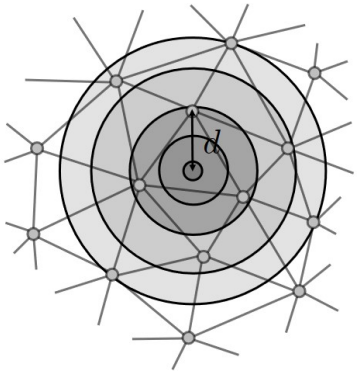

Figure 2.8: Interpolation of a point force on several grid points, [61]

Wherein d is the distance between the grid point and the location of the force on the actuator line, and ϵ the smearing (or regularisation) parameter.

The choice of ϵ is critical, as it needs to be large enough to guarantee stable computations while being small enough to provide accurate results. If a constant value is usually taken, the decreasing blade chord length at the tip can lead to an over-prediction of the loads in this region. Indeed, at the tip, the spreading radius results in being too large, inducing wider tip vortices and smaller associated induced velocities, resulting in a wrong estimation of the local angle of attack and an overestimation of the generated lift [62]. However, if a constant value is chosen for ϵ, tip loss correction models can be used to overcome this issue. Such a model was developed by Shen et al. [63] and is typically used. In addition, filtered ALM, as developed by Martinez-Tossas and Meneveau [64], and as used in combination with tip-correction in the work of Stanly et al. [62] can be preferred. This modified approach permits to avoid the over-prediction of lift when coarser grids and large smearing parameters are used.

More details on the mesh requirements associated with this process are given in the next section.

Other elements modelling

The discussion on ALM above was focused on the blade modelling, but a similar approach can be used to model the impact of other elements such as the tower or the nacelle.

Even if these elements are often omitted, they can play a key role and significantly influence the flow field surrounding the rotor. Benard et al. [9], for example, highlighted the impact of the nacelle and the tower, which are responsible for different flow phenomena such as initiating the breakdown of the tip vortices for the tower [62].

Therefore, actuator approaches can be chosen to model the impact of the nacelle and/or the mast. Li et al. [38], for instance, modelled the nacelle thanks to a simplified actuator surface approach, and

Gao et al. [65] with an actuator line and a modified Gaussian function for distribution. Concerning the tower, an actuator line is generally preferred, with the airfoil replaced by a simple cylinder and its corresponding lift and drag coefficients. Constant values can be used, but time-dependent descriptions can also be found in the form of:

$$C_d = A_1 \quad ; \quad C_l = A_2 \sin(2\pi f_t t) + A_3 \tag{2.17}$$

Wherein, the A_i are constants depending on the tower and on the flow (Reynolds number). The shedding frequency f_t is computed thanks to the Strouhal number $St = f_t D_t / U_\infty$ with D_t being the tower diameter and U_∞ the incoming wind speed. Such a method, accounting for the unsteadiness of the tower wake, is frequently used, as in the works of Sarlak et al. [66] or Stanly et al. [62].

2.4.2. Large-Eddy Simulation

This part aims at presenting more in detail the parameters and characteristics required for the simulation of a floating offshore wind turbine using large-eddy simulations with an actuator line approach.

Overview of existing literature

If a growing interest has been given to FOWT aerodynamics, there are still only a few simulations using LES with coupled or imposed floating motions. Therefore, a certain number of requirements for large-eddy simulations are directly taken from fixed-bottom turbine studies.

However, there are still several studies using LES to study the behaviour of FOWT. Indeed, a certain number of studies used the code SOWFA [67] with, for example, Wang et al. [20] who prescribed a pitching motion on four rotors in order to compare with experimental results. Later, the code SOWFA was coupled with OpenFAST in order to have realistic platform motions [21]–[23], [68]. In particular, two floaters were compared by Johlas et al. [22] and complex inflows were imposed by Xu et al. [23]. Using a different code than SOWFA, Xiao and Yang [69] also prescribed pitching motions, but on an array of nine FOWT. On the other hand, Li et al. [38] imposed a side-to-side motion, equivalent to sway motion and arguably close to roll motion as well. Finally, Yu et al. [19] developed a fully-coupled model using a LES approach for the aerodynamic loads.

LES formulation and SGS modelling

Direct numerical simulation (DNS) is the ideal high-fidelity CFD simulation in which all the scales are resolved. Unfortunately, its cost is prohibitive for wind turbine applications. Large-eddy simulation (LES) follows the same principle as DNS, but, in order to lower the computational cost, only the large scales of turbulence are resolved. However, the influence of the smallest scale as well as their interaction with the largest are important and cannot simply be neglected. Sub-grid scale (SGS) models are thus used to account for the impact of the smallest eddies. The difference between the largest and smallest eddies is made by means of a space-filtered function, and, for instance, the velocity u that would have been filtered is denoted as $\bar{u}$. LES remains very high-fidelity and computationally demanding, but, for a few years now, it has become more accessible. It is particularly adapted for 3D, unsteady, and complex flows such as a wind turbine wake [9].

Within the unresolved scales, a distinction needs to be made between sub-grid scales and sub-filter scales. The former, are not represented on the too coarse mesh, the latter are unresolved because they were removed or damped by the filter. In practice, a 3/2 rule is generally adopted so that the filter size $\overline{\Delta}$ is 1.5 larger than the grid size Δ_g [70].

With the filtering operation denoted by $\overline{\cdot}$, the NS equations become:

$$\frac{\partial \overline{u}}{\partial x_i} = 0 \tag{2.18a}$$

$$\frac{\partial \overline{u}_i}{\partial t} + \frac{\partial \left(\overline{u}_i \overline{u}_j\right)}{\partial x_j} = -\frac{\partial \left(\overline{p}/\rho\right)}{\partial x_i} + \frac{\partial \left(2\nu \overline{S}_{ij}\right)}{\partial x_j} - \frac{\partial \tau_{ij}}{\partial x_j} - \frac{f_i}{\rho} \tag{2.18b}$$

Wherein $\overline{S}_{ij} = \frac{1}{2}\left(\frac{\partial \overline{u}_i}{\partial x_j} + \frac{\partial \overline{u}_j}{\partial x_i}\right)$ is the shear tensor, ρ the density and ν the viscosity of the fluid. f_i is an additional body force term to account for the effect of the wind turbine on the flow when it is not directly modelled. It can be noted that the second left-hand term is the so-called convective term,

which is particularly difficult to numerically resolve. Finally, $\tau_{ij} = \overline{u_i u_j} - \overline{u}_i \overline{u}_j$ represents the impact of the smallest scales on the largest ones and requires a SGS model. The goal of such a model is to reproduce the energy cascade: the largest eddies carry most of the turbulent energy, transfer it to the smallest eddies, which ultimately dissipate it. For the SGS model, this means that it should not add, nor dissipate too much turbulent energy in the flow.

The first SGS model was introduced by Smagorinsky [71], it bears his name and uses the concept of eddy viscosity ν_{SGS} to give a relation for the τ_{ij} tensor:

$$\overline{\tau}_{ij} = \frac{1}{3}\delta_{ij}\overline{\tau}_{kk} - 2\nu_{SGS}\overline{S}_{ij} \tag{2.19}$$

Translating Prandtl's mixing length model (0-equation model), the ν_{SGS} parameter is related to the filter width $\overline{\Delta}$ and the strain-rate tensor $|\overline{S}| = \sqrt{2\overline{S}_{ij}\overline{S}_{ij}}$ via a constant C_S as follows:

$$\nu_{SGS} = \left(C_S\overline{\Delta}\right)|\overline{S}| \tag{2.20}$$

The standard Smagorinsky model is still widely used for its simplicity while guaranteeing viable results. However, the constant C_S needs to be calibrated depending on the type of flow studied, the Reynolds number, or the discretisation scheme. Furthermore, the model generally requires correction in boundary layers such as the van-Driest damping.

A dynamic procedure to compute the constant in Smagorinsky's model was first proposed by Germano et al. [72]. Later, Lilly [73] suggested a modification of the dynamic procedure. Those models are widely used and often preferred to the standard Smagorinsky because of the globally improved results, including at the near-wall, and the lack of need for tuning the constant. In simulations for FOWT, the former was notably used by Li et al. [38] while the latter was used by Xiao and Yang [69] and Johlas et al. [21].

Among the most used SGS closure models, the σ-model [74], the Wall-adapting local eddy-viscosity (WALE) [75] and the Vreman model [76] must also be cited.

If a comparison of SGS models for FOWT applications was not found, a few such studies exist for fixed-bottom turbines. In the work of Sarlak et al. [66], seven eddy-viscosity closure models were compared on two fixed turbines aligned in the direction of the incoming wind. These models are: no model ($\nu_{SGS} = 0$), standard Smagorinsky, mix-ω, mix-S and, for each, their dynamic version using the Germano identity. In the paper, the impact of blade resolution and the smearing parameter were also discussed and found to be of greater significance in the prediction of blade loads and power, compared to the different SGS models. Three well-known SGS models (Vreman, WALE, and σ-model) were also compared to the standard Smagorinsky for a single fixed HAWT in the work of Ciri et al. [77]. In terms of thrust and power generated, the results were found to be similar again. However, larger differences were noted in the wake, where the more dissipative models (WALE and σ) caused an earlier transition to turbulence and a shorter recirculation zone. The Vreman model also led to unstable situations due to its associated low dissipation but also due to the coarse mesh used. Finally, the standard Smagorinsky closure was also compared to the Germano dynamic procedure and a so-called Anisotropic Minimum Dissipation (AMD) model on VAWT by Abkar [78]. Again, little impact was noticed on the mean aerodynamic loads, while the structure of the wake was significantly affected. The standard Smagorinsky, which over-dissipates the energy of the smallest resolved scales, caused further transition to turbulence. The calibration of the constant was nonetheless found to be capable of improving the prediction of turbulent characteristics and of the wake.

Domain

The geometric domain surrounding the turbine's rotor, and eventually its other elements, which will later be discretised into a mesh, has to be chosen carefully. It needs to be large enough to be able to capture all the different behaviours in the flow to be observed. For a wind turbine, this is generally the wake development and expansion, the induction region, the diffusion of tip- and root-vortices, etc. On the other hand, if the domain is chosen too large, the computational cost can significantly increase without necessarily improving the results.

Gao et al. [65] observed that for fixed turbines, the domain around a rotor of diameter D is generally taken in the range $L_x \times L_y \times L_z = (2D - 5D) \times (2D - 5D) \times (7D - 15D)$ wherein L_x, L_y and L_z refer

respectively to the length in the transverse, vertical, and streamwise directions. However, these typical ranges can be slightly extended as Abkar [78] and Li et al. [38] used, respectively, domains of size $6D \times 6D \times 30D$ and $7D \times 7D \times 14D$. Furthermore, it was found that the rotor was generally placed between $3D$ and $5D$ after the inflow [38], [78], [79].

However, it can be frequent to find large eddy simulations with a geometric domain even larger when the atmospheric turbulence and its effect on the turbine are to be studied, such as in the study by Li and Yang [80].

Finally, it is also common to find domains whose dimensions and boundary conditions are chosen to mimic the environment encountered within a specific wind tunnel [9], [66], [70], [77]. This approach is used to compare the numerical results precisely with the experimental ones, and include the so-called blockage effect.

Grid

Once the geometric domain is defined, the grid, or mesh, needs to be generated. This process is of particular importance for CFD simulations, as the quality of the mesh is closely related to the quality of the results obtained.

Whether the grid is structured or unstructured, allowing for simpler generation around complex geometries [9], the two most important criteria are its density and its orthogonality.

Orthogonality refers to the angle between the borders of a cell and the local incoming and leaving flow. Denoted by a number between 0 and 1 (where 1 corresponds to a flow totally orthogonal to the cell), it should be kept as high as possible in order to avoid numerical diffusion. As an order of magnitude, Sheidani et al. [81] used a mesh with an average orthogonal quality of 0.9 and a minimum of 0.3 which is considered a good quality for large-eddy simulations.

Concerning the mesh density, it corresponds to the requirement that the cells should be small enough in order to capture the flow effects, even at the smallest scales. For blade-resolved, or other wall-bounded flows, this calls for highly refined regions near the wall to capture the boundary layer development [82]. For large-eddy simulations in general, the grid needs to be fine enough to resolve a sufficient amount of turbulent scales. As mentioned in Sheidani et al. [81], it is generally agreed that at least 80% of the turbulent kinetic energy should be resolved. For the flow surrounding a wind turbine, this generally requires grid refinement near the rotor and in the wake. Within the wake, it can even be chosen to refine more locally where the tip and root vortices are expected.

If the rotor is not fully resolved but modelled by means of actuator lines, for instance, the required size of the smallest cells is not dictated by the wall unit but rather by the number of cells along the actuator lines. Here, a distinction needs to be made between the number and size of the actuator line segments (N_{AL}, Δ_{AL}), and the number and size of the mesh cells nearby the actuator lines (N_{grid}, Δ_g). A ratio of $\Delta_{AL}/\Delta_g \geq 1.5$ is generally advised [79].

Concerning N_{AL}, the number of elements the actuator lines are discretised by, it needs to be large enough to smoothly and accurately capture the load distribution along the span. Jha et al. [79] suggested a minimum of $\Delta_{AL}/R \leq 1/20$ to correctly compute the thrust and power generated. On the other hand, Benard et al. [9] followed a guideline suggesting $\Delta_{AL}/R \leq 0.03$ which resulted in the use of $N_{AL} = 32$. Sarlak et al. [66] compared five grids, corresponding to different rotor resolutions (from $N_{AL} = 13$ to 52) and found the results to converge after $N_{AL} = 35$. The convergence was reached with 50 points per line in Stanly et al. [62]. In general, a value between $N_{AL} = 30$ and 60 is chosen to provide accurate results [79].

Discretisation

In order to numerically resolve the NS equations written above, they need to be discretised both in time and in space. This calls for specific spatial and temporal schemes. For the sake of brevity, these methods will not be discussed in detail, but the most common ones are cited, and a few remarks on their orders (related to the numerical errors) are made.

Concerning spatial discretisation, once the domain is discretised into elements or cells, the first step is to choose the systematic approach, whether a finite difference (FD), a finite volume (FV) or a finite element (FE) method will be implemented. Then, a discretisation scheme of a certain order needs to be chosen as a trade-off between accuracy, stability, and computational cost.

In Benard et al. [9], three different discretisation schemes of respectively 1st, 2nd, and 4th orders were compared to simulate the flow around a fixed wind turbine, and the authors highlighted the interest

of high order methods. Indeed, the 1st order scheme resulted in very poor results, and significant differences were also observed between the other two, as more numerical diffusion was observed with the 2nd order scheme. Moreover, when an actuator line method is used, Jha et al. [79] observed oscillations in velocity and pressure with a 2nd-order linear scheme and highlighted the interest of hybrid linear/upwind methods in order to solve these oscillations.

In practice, the well-known 2nd order central differencing scheme is widely used [20], [38], [77] and its 4th order derivative is used more rarely [66]. In the latter article, the authors also chose to solve the convective term with a lower order scheme (3rd), resulting in a hybrid global method. Hybrid methods are also occasionally used in order to differentiate the directions, generally using a different scheme in the vertical direction [70], [78].

On temporal discretisation, no similar comparison was found as for spatial solving. However, a few methods regularly come back, among which figure the Runge-Kutta family and the widely used RK4 (4th order) [9], [62]. The second-order backward Euler scheme is also regularly used [20], [66] as are the schemes of the Adams–Bashforth family [70], [78].

If the spatial steps are given by the grid and its elements' sizes, a time step needs to be carefully chosen for temporal discretisation.

Usually in CFD, the well-known Courant–Friedrichs–Lewy (CFL) condition is used in order to guarantee convergence of the numerical computations. If an explicit scheme is used, the Courant number is typically kept under unity, while it can reach higher values for implicit schemes. However, for wind turbines, when the blades are resolved or represented by means of actuator lines, a smaller time step is generally required. Indeed, in order to well capture the tip vortices, it is generally advised that the blade tip should not cross more than one grid cell per time step [79]. As these regions near the rotor are generally refined and the grid cells small, this results in the use of a time step corresponding to a CFL number well below unity [70], [81].

3

Methodology

This chapter describes the methodology employed during the work. The aerodynamic tool YALES2 as well as the experimental campaign used as a source of validation are described.

3.1. TU Delft experimental campaign

An experimental campaign was conducted in April 2023 within a wind tunnel at Delft University of Technology by Federico Taruffi and Felipe Miranda Novais on a scaled-down floating offshore wind turbine. The experiment permitted the measurement of the temporal variations of loads (using a 6-DOF balance) during a wide range of motions. One- and two-degree-of freedom motions, as well as more complex motions, were investigated. As the experiment was realised relatively shortly before these words were written, no publication is yet available, except for a draft paper the authors submitted [83]. It presents the experimental setup and discusses the first results.

A picture of the experimental setup is given in Figure 3.1 where one can see the turbine mounted on the hexapod in front of the wind tunnel nozzle.

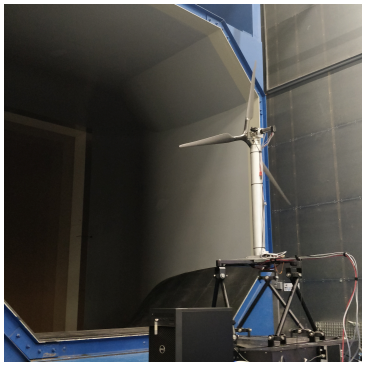

Figure 3.1: View of the experimental setup, courtesy of Federico Taruffi and Felipe Miranda Novais

3.1.1. Wind tunnel

The experimental campaign was conducted within the Open Jet Facility (OJF) at TU Delft. It is a closed-loop open-jet wind tunnel, as illustrated Figure 3.2. The wind flow can reach wind speeds up to $35\ m/s$ and is achieved by a large fan that is driven by a 500 kW rated electric engine.

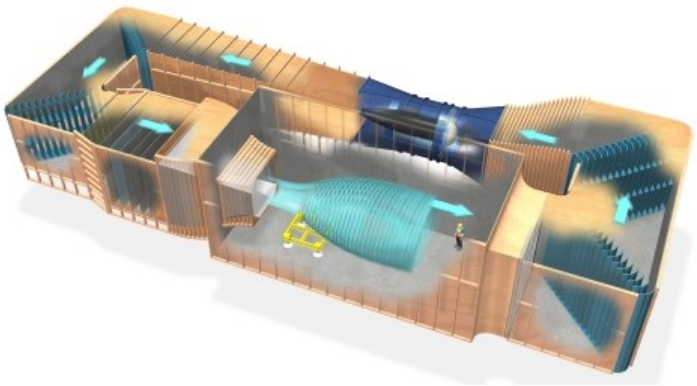

Figure 3.2: Schematic representation of the Open Jet Facility (OJF)

The nozzle has an octagonal shape with a $3\ m$ equivalent diameter and a contraction ratio of 3:1. It is followed by a large room of $13\ m$ width and $8\ m$ height.

The work conducted by Lignarolo et al. [84] has permitted them to evaluate the quality of the flow at the nozzle exit and in the test area. It was notably found that, at one metre downwind of the nozzle, the free-stream flow has a turbulence intensity of 0.5%.

3.1.2. Turbine model

The details about the scaled model and how the scaling was performed can be found in the work of Fontanella et al. [85]. In brief, it is a $1.2\ m$ scaled rotor of the DTU 10MW (corresponding to a 1:148 geometric scale) with a fixed blade pitch. The scaling was performed with the aim of replicating the blade normal-to-plane distribution of loads at the design tip-speed ratio (TSR) and with a 1:3 velocity scale factor.

The main characteristics of the scaled model are indicated Table 3.1 in comparison with the full-scale DTU 10MW.

Parameter	DTU 10 MW	Scale Model
Cut-in wind speed (m/s)	4	1.33
Rated wind speed (m/s)	11.4	3.8
Cut-out wind speed (m/s)	25	8.33
Rotor diameter (m)	178.4	1.2
Hub height (m)	118.0	0.79
Design TSR (-)	7.5	7.5
Design blade pitch (°)	0	0
Minimum rotor speed (rpm)	6	296
Maximum rotor speed (rpm)	9.6	473.6
Rotor tilt (°)	5	0

Table 3.1: Properties of the DTU 10 MW rotor and scaled values for the wind turbine model, adapted from [85] and [83]

The principal challenge for the authors was to deal with the low Reynolds number encountered at the blades of the scaled model (lower than 100k). This was dealt with by using the airfoil SD7032, whose polars were obtained via experimental results performed at DTU as part of the LIFES50+ project. They were later extended to $\pm 180°$. The geometry of the blades is represented Figure 3.3.

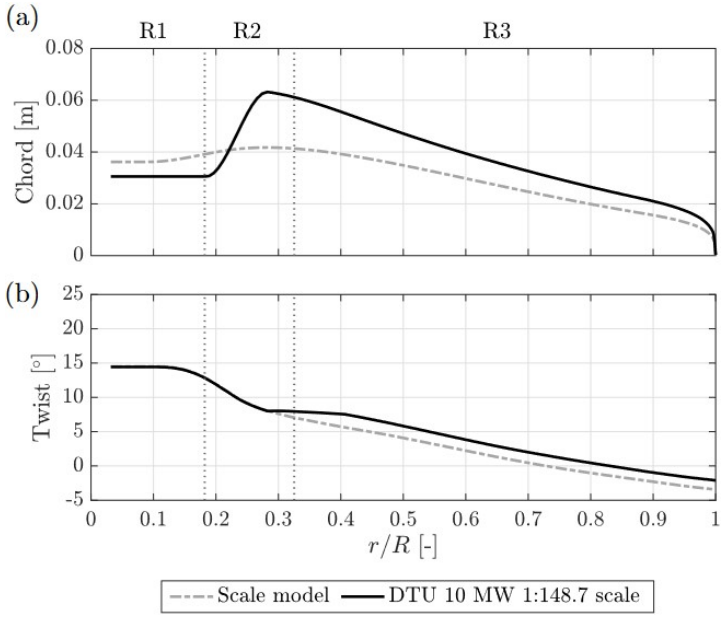

Figure 3.3: Chord and twist of the scale model blade in comparison with the DTU 10 MW at 1:148.7 scale, [85]

For the use of the code, the complete polars of the blades were provided for nine different Reynolds

numbers between 30k and 250k.

3.1.3. Test matrix

In the first part, sinusoidal motions of one degree of freedom were imposed in the surge, pitch, and yaw directions.

For the surge case, for example, the motion is given by:

$$z(t) = A_S \sin(2\pi f_S t) \tag{3.1}$$

Wherein A_S and f_S are, respectively, the surge amplitude and frequency.

The test matrix was generated in a similar way as in the UNAFLOW project [34]. Motion frequencies between $0.5\ Hz$ and $5\ Hz$ were chosen, corresponding to reduced frequencies from 0.15 to 1.5 (see Equation 2.8).

Similarly, the amplitude is not directly set but obtained by choosing a range of surge velocity ΔV. The following range was chosen:

$$\Delta V^* = \frac{\Delta V}{U_\infty} = (0.0125, 0.025, 0.0375, 0.05, 0.075, 0.1, 0.125)$$

In comparison, values only up to 0.05 were obtained during the UNAFLOW test campaign [34]. In addition, a review of most previous experimental and numerical cases investigated is presented in the work of Ferreira et al. [56] (caution, the reduced frequency is defined differently). One of the objectives of this test campaign was to extend a bit this range, and investigate higher reduced velocities.

As a result of this increase in the rotor's velocity and the motion frequency, the amplitude of motion can be computed:

$$A = \frac{\Delta V}{2\pi f} \tag{3.2}$$

The different cases were tested for two different freestream velocities: $U_\infty = 2.5\ m/s$ and $U_\infty = 4.0\ m/s$. For the latter case, the rotational velocity was set to 480 RPM, corresponding to the design tip-speed ratio $\lambda = 7.5$.

Later, two degrees of freedom were also imposed, including pitch/surge motions. Here, the cases were chosen to vary the amplitude and the frequency in the same set of ranges as before. A phase difference between the two motions ($0°$,$90°$,$180°$ and $270°$) was also introduced. Finally, a set of realistic motion sequences obtained via OpenFAST were also imposed.

3.1.4. Limitations of the experiment

Except for the usual limitations of experimental simulations (scaling parameters, etc.), it is worth mentioning some limitations that were encountered during the experiment.

First, the freestream velocity within the wind tunnel was found to be difficult to set precisely. Thus, variations around the desired freestream velocity were experienced. As a consequence, variations in the loads measured are also expected, without the possibility to precisely correct them as no measurement of the velocity was performed.

Then, the loads measured by the balance do not directly give the torque or the thrust. Inertial forces are also measured and need to be subtracted. However, when the motion is small, so are the load variations, and this process becomes more tricky and can introduce some errors. On this note, results obtained for $U_\infty = 4\ m/s$ were found to be of much higher quality than those obtained for $U_\infty = 2.5\ m/s$.

Finally, some cases with high frequency and large amplitude could not be reached because of the limits of the hexapod.

3.2. Numerical simulations

This part aims at presenting the code used for the numerical simulations as well as its main parameters used in all cases.

3.2.1. The code: YALES 2

YALES 2 is a Navier-Stokes solver created within the CORIA laboratory in Rouen, France. Its main characteristics can be retrieved from the paper by Moureau et al. [86].

The solver has been developed in order to be able to support grids with a very large number of elements (several billions). In particular, it allows for mesh refinement (as illustrated Figure 3.4) while several meshing software programmes struggle with very small elements and cannot sufficiently resolve certain flows. This refinement technique does not alter the orthogonality of the flow but keeps the same coarse representation of curved boundaries and should, therefore, be used with parsimony.

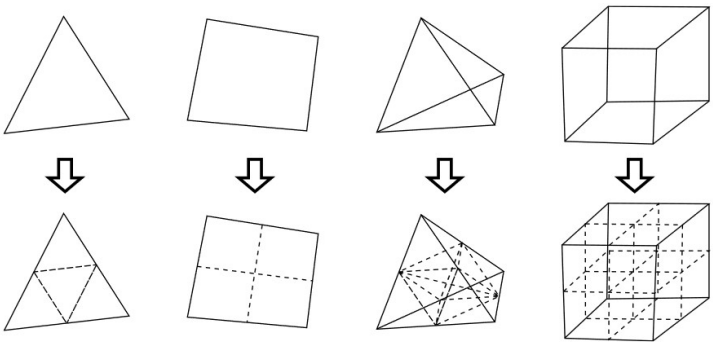

Figure 3.4: Examples of refinement of elements, [86]

Its capacity to deal with very small cells and large grids allows the use of DNS on certain flows, even if its main usage remains large-eddy simulations. YALES2 is principally used for incompressible and low Mach number flows and can deal with both structured and unstructured grids.

Concerning the discretisation techniques, a finite volume approach is implemented with different schemes available, including a central 4th-order scheme for spatial discretisation and a 4th-order 2-step Runge-Kutta scheme for temporal discretisation. The spatial numerical errors are thus 4th-order on Cartesian grids. However, a comparison between structured and unstructured grids in Benard et al. [9] has shown a similar order of errors on the unstructured grid.

Aside from Benard et al. [9], the code has been used several times to compute wind turbine flows. An adaptive mesh refinement method was notably implemented in the work of Zeoli et al. [87], presenting the interest of such a method in order to obtain similar results with a lower number of cells (thus lower computational cost). The development of the streamtube in yawed conditions was also investigated by Houtin-Mongrolle et al. [88]. As a last example, YALES2 was coupled with an aero-servo-elastic solver in the work of Gremmo et al. [89] to account for the elastic behaviour of the blades, but also of the tower and nacelle.

Finally, the implementation of the actuator line method in the code was modified by Ricardo Amaral in order to enable the motion of the wind turbine. The code can deal with all sorts of motions (not only sinusoidal) in the six degrees of freedom and was notably validated on the UNAFLOW's scale wind turbine in the context of the OC6 Phase III project [10].

3.2.2. Main simulation parameters

First, many solvers are available within YALES 2, but the incompressible one (ICS) was used here. It solves the Navier-Stokes equations in the form:

$$\frac{\partial u}{\partial t} + \nabla.(uu) = -\frac{1}{\rho}\nabla P + \frac{1}{\rho}\nabla.\tau \tag{3.3}$$

$$\nabla.u = 0 \tag{3.4}$$

A time step corresponding to a Courant number $CFL = 0.9$ is generally advised with this solver. However, as mentioned earlier, the requirement of having the blade tip not pass through more than one cell per time step can result in lower Courant numbers. This is particularly true for reduced-scale experiments in which the rotational speed is much higher. Therefore, lower CFL numbers will also be used and their influence investigated.

Many simulation parameters need to be determined as a trade-off between the accuracy of the results wanted and the computational resources required. Therefore, the objective of the simulation

and the desired outputs need to be clearly defined. This is particularly true for the mesh resolution, the domain size, and the corresponding simulation duration. Indeed, if the focus is to be put on the loads only and their variations in time, there is no need to solve the far wake precisely and capture its detailed development. Thus, it can be decided to neglect this part, only affecting the loads slightly, to reduce the computational cost. On the other hand, if precise insights into the flow and the wake are to be obtained, the domain and the simulation duration will need to be long enough, combined with a sufficient resolution of the wake in all the regions desired.

On the turbulence model, the dynamic Smagorinsky procedure as described by Germano et al. [72] and Lilly [73] was generally preferred. In any case, the literature review did not highlight significant differences between the most commonly used turbulence models, especially concerning loads.

The main input for the AL method is the blade polar. As mentioned earlier, they are dependent on the Reynolds number. However, the code is not capable of dealing with multiple Reynolds-dependent polars. Therefore, the interpolation was made before the simulation, with the Reynolds radial distribution calculated as follows:

$$Re(r) = \frac{\rho V_{eff}(r) c(r)}{\mu} \quad ; \quad V_{eff}(r) = \sqrt{U_\infty + (\Omega r)^2} \tag{3.5}$$

Wherein ρ is the air density, μ the dynamic viscosity, and $c(r)$ the chord length at radial position r. This formulation does not account for any impact of the loading or the rotor motion on the effective velocity as seen by the blade sections, which vary through time and are not necessarily available before the simulation. As a consequence, an error is introduced here. However, this error is believed to be small enough as the dominant term in the calculation of V_{eff} is the rotational velocity, which is particularly large in the cases considered. This assumption and its impact on the quality of the results will later be checked thoroughly.

Two parameters that have one of the greatest impact on the quality of the results are the mesh resolution and the time step used. Their influence will be investigated in detail in the following sections.

Finally, one last important feature of the numerical model when doing CFD is the boundary conditions of the domain. Here, they need to be chosen carefully in combination with the domain geometry if the experimental campaign is to be mimicked. Indeed, in the experiment, the influence of the wind tunnel and its walls altered the flow around the rotor. The blockage effect, for example, refers to the fact that the airflow is not totally free to expand around the rotor and can significantly alter the loads. Ideally, the wind tunnel could be represented in the domain, and the flow could be notably resolved at its walls. However, this would significantly increase the cost of the simulations. Instead, it is chosen to avoid any interference effects in the simulation and account for the ones occurring in the wind tunnel by modifying the freestream velocity at the inlet.

First, in order to avoid any blockage effect in the simulation, the cross section of the domain should be chosen to have a blockage ratio at least inferior to 5% [90], [91]. The blockage ratio is equal to the ratio of the area of interest (here the rotor area) over the cross section of the domain. For example, for a square cross section of $4D \times 4D$, the blockage ratio is equal to 4.9%. Therefore, these dimensions should be used as a limit for the minimum cross-section area to have a negligible blockage effect. This will also be checked in the next chapter.

Finally, concerning the inlet, the freestream velocity magnitude is not the only parameter to be considered. Indeed, it can be chosen to have a non-uniform velocity distribution if the turbine is to be in the atmospheric boundary layer, for instance. Here, the flow measurements in the wind tunnel performed by Lignarolo et al. [84] have shown that the flow is uniform at the test section. The flow also has a turbulence intensity of about 0.5% that could be taken into account to increase the fidelity of the results, even if it remains a small value.

3.2.3. Mesh generation

As mentioned previously, YALES2 offers the possibility to deal with unstructured meshes and refine them to achieve small element sizes. In order to generate the meshes, the open-source 3D finite element mesh generator Gmsh was used [92]. This software provides a fast and user-friendly way the generation of meshes of different complexities. In the case of this study, it permitted to generate relatively simple unstructured meshes with refined zones for the rotor or the wake, for example. A

particularly interesting feature is the possibility of generating the mesh via a simple script. Therefore, some parameters, such as the size of the refinement areas or the cell width, can be easily changed from one mesh to another.

For the cases presented in the next sections, it was generally chosen to generate a relatively coarse mesh with Gmsh and use twice the refinement method implemented in YALES2.

3.2.4. HPC12

The simulation of wind turbine flows in LES calls for the use of large meshes, with millions of cells, which requires significant computational resources. Therefore, YALES2 was installed on the supercomputer HPC12. It is a cluster of nodes administered by the ICT department ay TU Delft and used by the ASM (Aerospace Structures and Materials) and FPT (Flow Physics and Technology) departments.

4

Validation

The aim of this chapter is to validate the numerical model and its main parameters that will be used to simulate the behaviour of the scaled FOWT.

4.1. Convergence of simulation parameters

The recommendations for the main parameters (time step, domain, mesh, and discretisation) found in the literature have been described in the previous sections. Yet, it remains to be checked whether those guidelines are suitable for the problem studied here, and if they can be simplified to save computational time.

For this purpose, a simulation was run with a set of parameters following the main guidelines. Then, various simulations in which only one parameter was changed were run and compared.

4.1.1. Original simulation

This part describes the numerical setup of the simulation used as a reference for the convergence analysis.

First, concerning the time step, it is generally advised to use a Courant number $CFL = 0.9$ for the incompressible solver in YALES2. However, for wind turbine applications, it was found in the literature that the tips should not travel more than one cell during one time step, in order to compute accurately the important tip vortices. Therefore, based on the local cell size, the CFL number was lowered to 0.65 to meet this criterion.

On the domain, it was chosen to be large ($6D \times 6D \times 15D$) in order to minimise any blockage effect (blockage ratio of about 2.2%) and to capture a sufficiently long part of the wake development.

The domain was then discretised into a grid. A coarse mesh with four refinement regions has been created on Gmsh, and all the cells were subdivided twice using the method implemented in YALES2. The mesh, in the plane perpendicular to the rotor ($x = 0$), and after refinement, is represented Figure 4.1. The mesh is identical in the $y = 0$ plane, and the rotor is centred at $(0, 0, 0)$. Four regions were refined (in descending order of cell size): the far-wake, the mid-wake, the near-wake, and the region near the rotor. The cell size within the most refined area, near the rotor, was determined in order to achieve a sufficient number of actuator points: $N_{AL} = 40 \in [30; 60]$. Then, a small cell size was kept in the near-wake; as the loads highly depend on the behaviour of the wake in this region. The quality of the mesh is reduced in the downwind regions as the focus of this study is rather on the loads and the near/mid-wake behaviour than on the far-wake development. The annotations in Figure 4.1 stand for the original coarse mesh from Gmsh, before refinement. As $lc = 0.4\ m$ is the cell width in the outer region, the average cell width in each region can be computed by dividing by 64 (two consecutive subdivisions into eight elements for each cell). They are summarised in Table 4.1.

Then, as advised in the work of Benard et al. [9], 4th-order discretisation schemes were used for both spatial and temporal discretisation.

As a reminder, the boundary conditions are slip walls everywhere except for the inlet, at which a uniform freestream velocity is prescribed, and at the outlet. On the last one, YALES2 tries to set a flat velocity profile to avoid backflow issues.

Refined region	Coarse Gmsh mesh	Final mesh
Outer-region	400	6.25
Far-wake	200	3.13
Mid-wake	80	1.25
Near-wake	57	0.89
Rotor	33	0.52

Table 4.1: Average cells' width within each sub-regions (in mm)

Finally, the tests were conducted for a 1-DOF harmonic surge motion with $f = 2\ Hz$ and $\Delta V^* = 0.05$.

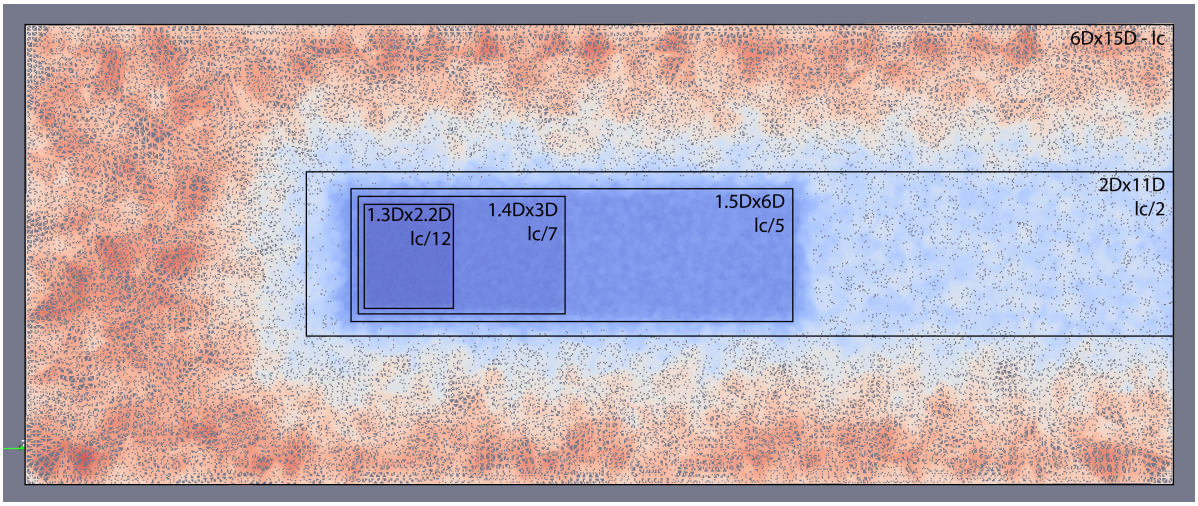

Figure 4.1: Mid plane ($x = 0$) slice of the original mesh, coloured by cells volumes, $lc = 0.4\ m$

4.1.2. Time step

As described above, the CFL number was lowered to $CFL = 0.65$ in comparison with the advised $CFL = 0.9$ for the solver. As a consequence, the total computational time for the simulation is increased. Therefore, it can be interesting to estimate to what extent the accuracy of the simulation is increased, and see whether it is worth it in terms of computational time or not. For this purpose, the exact same simulation was run with $CFL = 0.9$.

As a consequence, the average time step was increased from $0.43\ ms$ to $0.60\ ms$.

First, no particular difference could be observed in the development of the tip vortices between the two simulations. As illustrated in Figure 4.2, differences in the wake only start to appear at the end of the near wake (around $z = 3D$). However, differences in the loads were still found. Indeed, the thrust and the power generated by the turbine are plotted Figure 4.3a and Figure 4.3b. If the amplitude and phase of the two signals are identical, the lowest CFL number shifts the loads upward. The relative difference between the two average values is equal to 0.9 % for the thrust, and 2.7 % for the power. In addition, the power spectral density of the thrust for the two simulations is plotted Figure 4.3c. Again, the differences between the two simulations remain small, and the higher time steps permit the same peaks to be captured. The most significant peak appears at $f = 2\ Hz$, the surge motion frequency. It can be noted that, in the absence of tower or structural effects, there is no particular peak at 1P ($50.3\ Hz$), 2P, 3P or etc.

In conclusion, the lower Courant number does not provide crucial additional data but leads to a slight shift of the loads towards higher values. The two simulations were not performed on the exact same nodes on the cluster; therefore, the comparison between the total computational time cannot be directly done (the total time was actually lower for the higher CFL number, but the nodes are believed to be less efficient). For the following work, it was chosen to keep a CFL number corresponding to the tip speed criterion as it slightly improved the results without having too much of an impact on computational time.

Lastly, it should be mentioned that such a temporal discretisation is more than enough to capture the floating motion. The highest motion frequency investigated is $f = 5\ Hz$ and needs to be compared

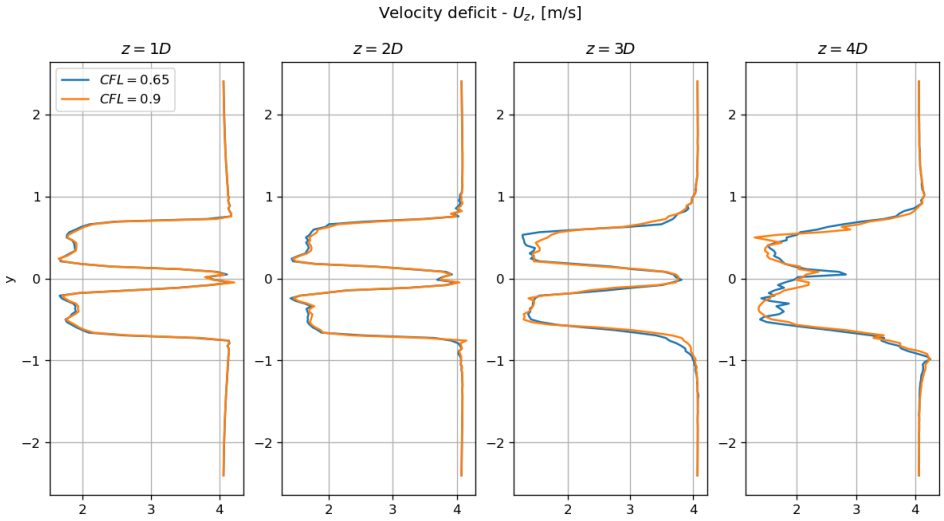

Figure 4.2: Impact of the Courant number on the instantaneous velocity deficit at four different locations and $t = 6.0\ s$

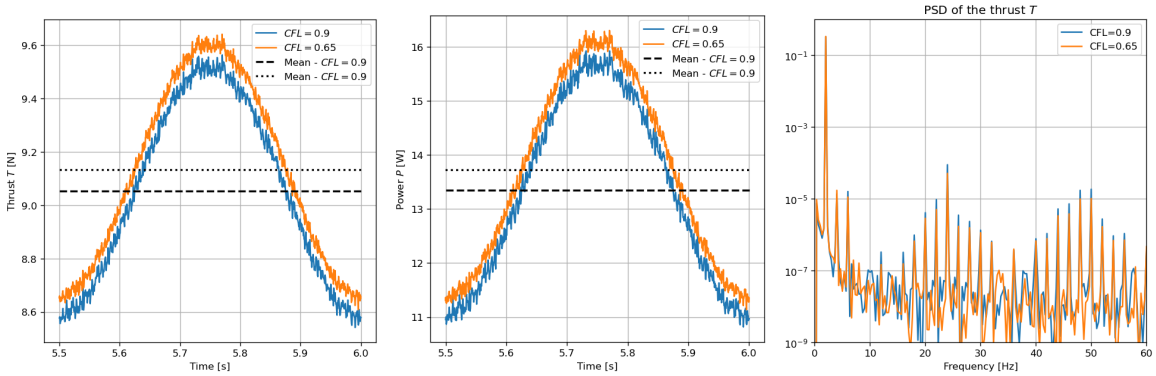

(a) Thrust (b) Power (c) PSD thrust

Figure 4.3: Impact of the Courant Number on the loads

with the much higher rotational speed of $\Omega = 480\ RPM = 50\ rad/s$.

4.1.3. Domain

The two main criteria for the domain here are to avoid any blockage effect and to capture a sufficient part of the wake development, in order to estimate the loads accurately and observe the behaviour of the near wake. Those criteria call for a sufficiently large domain in both the rotor plane direction and the streamwise direction. However, for the same cell width, the larger the domain, the more cells there are, and the more computationally demanding the simulation. Yet, this is not always significant if only the regions where the cells are the biggest are enlarged. Finally, the simulation needs some time for the wake to develop from the rotor and converge. The longer the region downwind of the rotor, the longer the simulation.

In order to obtain the optimal domain size, three configurations in addition to the original simulations were investigated. There are summarised below ($L_x \times L_y \times L_z$, for respectively transverse, vertical, and streamwise directions):

- $4D \times 4D \times 7D$ (rotor at $2D$ after inlet)
- $6D \times 6D \times 10D$ (rotor at $3D$ after inlet)
- $6D \times 6D \times 15D$ (rotor at $5D$ after inlet) - original simulation
- $8D \times 8D \times 20D$ (rotor at $7D$ after inlet)

For each domain, the mesh was generated the same way with the same refinement regions, except for the largest domain, in which the mid-wake and far-wake regions were slightly extended.

First, the loads are plotted for one surge period in Figure 4.4.

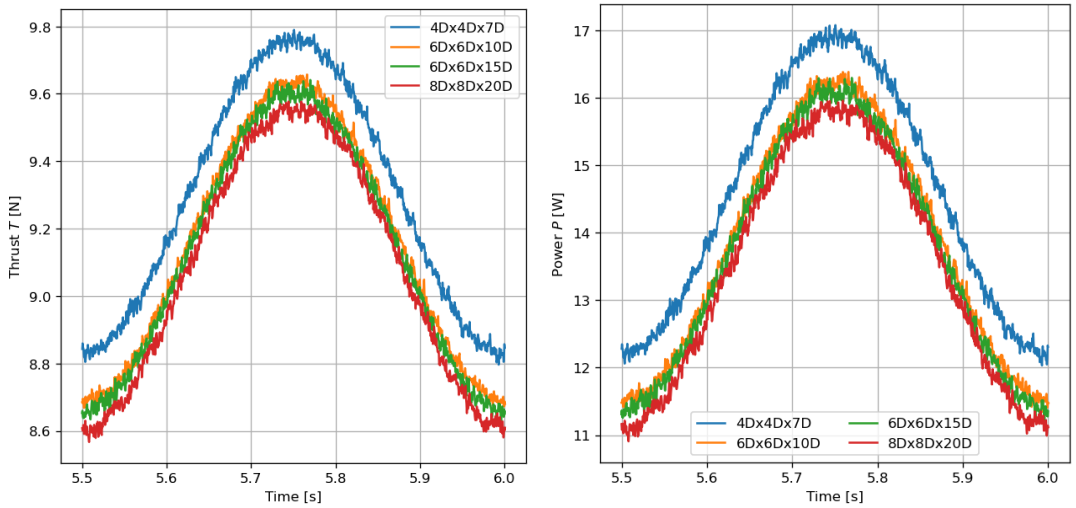

(a) Thrust (b) Power

Figure 4.4: Impact of the domain size on the loads

It appears that there is barely any difference between the two simulations with the same rotor plane dimensions. The loads for these two simulations are also fairly close to those of the largest domain. In contrast, the differences with the smallest domain results are significant. Therefore, the dimensions in the wind direction did not significantly affect the results, but the ones in the rotor plane direction did. This is attributed to the blockage effect. In order to visualise that, the velocity deficit is plotted at one near-wake location ($z = 2D$) in Figure 4.5.

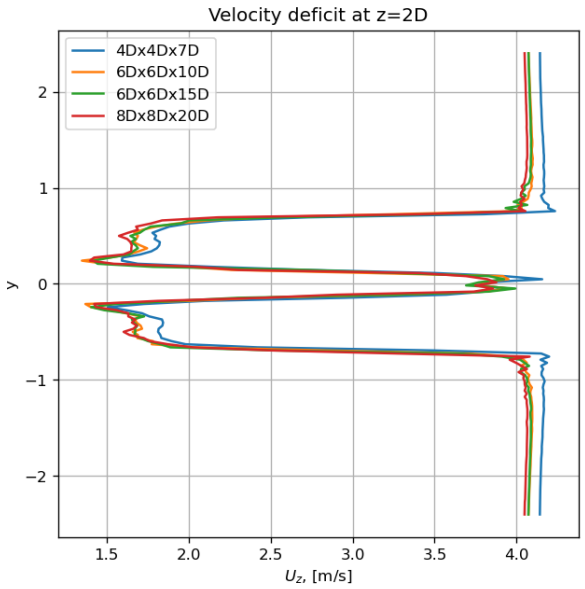

Figure 4.5: Impact of the domain size on the instantaneous velocity deficit at $z = 2D$ and $t = 6.0\ s$

The blockage effect can be clearly observed in the outer part of the wake, where the wind speed is constant. Indeed, due to the presence of the walls, the flow is accelerated in the inner and outer parts of the wake when the domain is too small. It is generally advised to use a blockage ratio at least inferior to 5% [90], [91]. The blockage ratio is defined as the ratio between the rotor area and the domain in-plane

area for wind turbine applications. For the configurations $4D \times 4D$, $6D \times 6D$ and $8D \times 8D$, the blockage ratio is respectively equal to 4.9%, 2.2% and 1.2%. Therefore, even if the 5% limit is generally advised, it is found here that a lower value should be preferred if possible.

In conclusion, the second configuration with the domain equal to $6D \times 6D \times 10D$ was chosen for most of the following simulations.

4.1.4. Actuator line discretisation

The number of points at which the actuator lines are discretised is a key parameter. As discussed previously, it is generally advised to use values between 30 and 60, but this can differ from one problem to another and from one blade geometry to another. Indeed, wind turbine blades can roughly be divided into three parts: the root, the tip, and the part in between where most of the loads are concentrated. The flow at the extreme parts, on the other hand, is highly three-dimensional. All those three parts need to be sufficiently discretised in order to accurately estimate the loads and capture the flow behaviour.

Configuration	N_{AL}	Δ_{AL} $[mm]$	CFL	$\overline{dt}$ $[ms]$	N_{elem} $[\times 10^6]$
1 (original)	40	14.6	0.65	0.43	56
2 (lower resolution)	31	18.8	0.509	0.49	29
3 (higher resolution)	46	12.7	0.745	0.46	71

Table 4.2: For each configuration, number N_{AL} and width Δ_{AL} of blade elements, Courant number CFL, average time step $\bar{dt}$ and total number of mesh elements N_{elem}

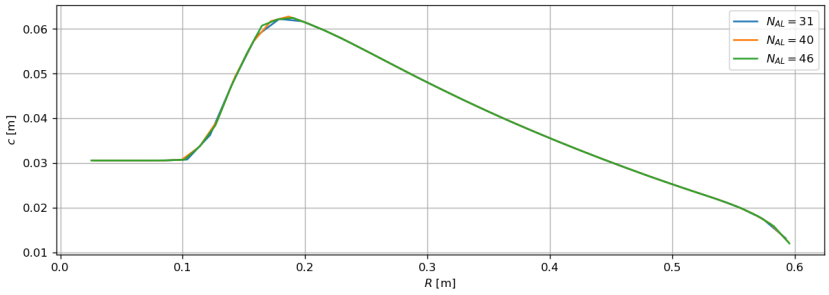

Figure 4.6: Discretisation of the blades geometry for 3 different resolutions

In YALES2, the actuator lines are discretised uniformly, with the elements' width Δ_{AL} being automatically computed to match the width of the largest cells near the rotor. Therefore, by increasing the mesh resolution in the rotor's refinement region, one increases the number of blade elements N_{AL}.

Configuration	$\bar{T}$ $[N]$	ΔT $[N]$	ϕ_T [°]	$\bar{P}$ $[W]$	ΔP $[W]$	ϕ_P [°]
1 (original)	9.13	0.47	-90.6	13.73	2.37	-90.7
2 (lower resolution)	9.25	0.48	-91.1	14.06	2.39	-90.9
3 (higher resolution)	9.01	0.46	-90.0	13.27	2.33	-90.0

Table 4.3: Amplitude of variation, mean value and phase difference with the surge motion of the thrust and power

In addition to the original simulation, two more configurations have been investigated. The mesh resolution was varied in order to obtain different blade discretisation. In order to make the simulations more comparable, the CFL number was also varied so that the time steps remained of the same order of magnitude (it is computed with the velocity, the Courant number, and the size of the smallest cells, which differs here from one simulation to another). The main characteristics of each simulation are gathered in Table 4.2.

The different actuator line discretisations were obtained by modifying the mesh resolution near the rotor. On the one hand, the lower resolution was obtained by using the exact same mesh as the original simulation, but the parameter lc increased from 0.4 to 0.5. On the other hand, the higher resolution was obtained by only refining the rotor refinement region, passing from $lc/12$ to $lc/14$. Therefore, it should be noted that not only the blade discretisation changed but also the mesh resolution.

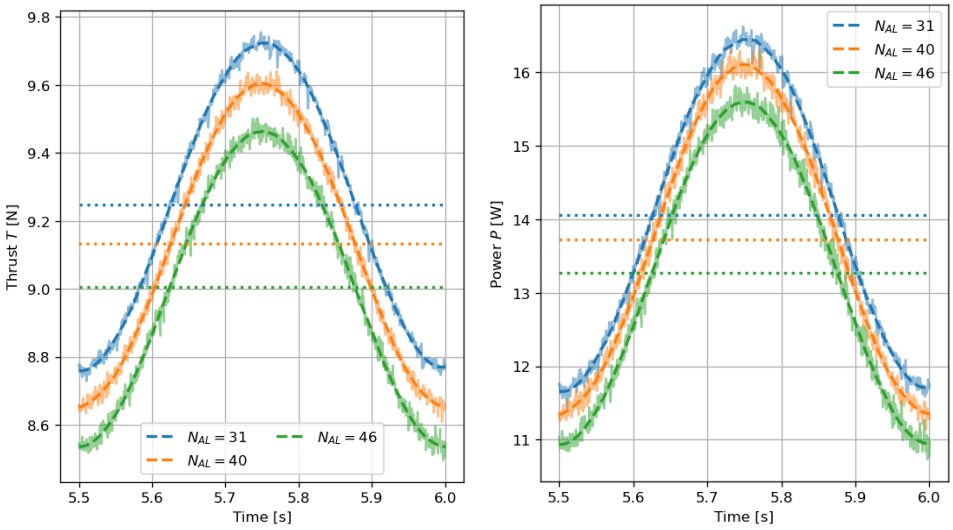

(a) Thrust (b) Power

Figure 4.7: Impact of the mesh resolution in the rotor region on the loads, including the filtered (dashed lines) and averaged (dotted lines) solutions over one motion period

First of all, one can check that, in each simulation, the blades are sufficiently discretised to accurately model their geometry. The radial distribution of the chord is plotted Figure 4.6. There are very few differences, and even the lowest resolution gives a good geometry.

Then, moving on to the results of the simulations, the thrust and power have been plotted for one surge period in Figure 4.7. The detailed results have been summarised in Table 4.3. Therefore, if there are some differences between the three configurations, they remain relatively small (less than 3% relative difference between the lowest and highest resolution on the mean loads). The trend is that, using a lower resolution tends to overestimate the loads. This can be verified at the blade level in Figure 4.8 where the radial distribution of the mean angle of attack and the mean aerodynamic coefficients have been plotted. As there were no significant differences at the root region, and for clarity, only the central part and the tips have been represented. Again, differences are noticeable but remain small. On the phase difference, the finer the rotor resolution, the more it converges to the theoretical quasi-static value of $-90.0°$.

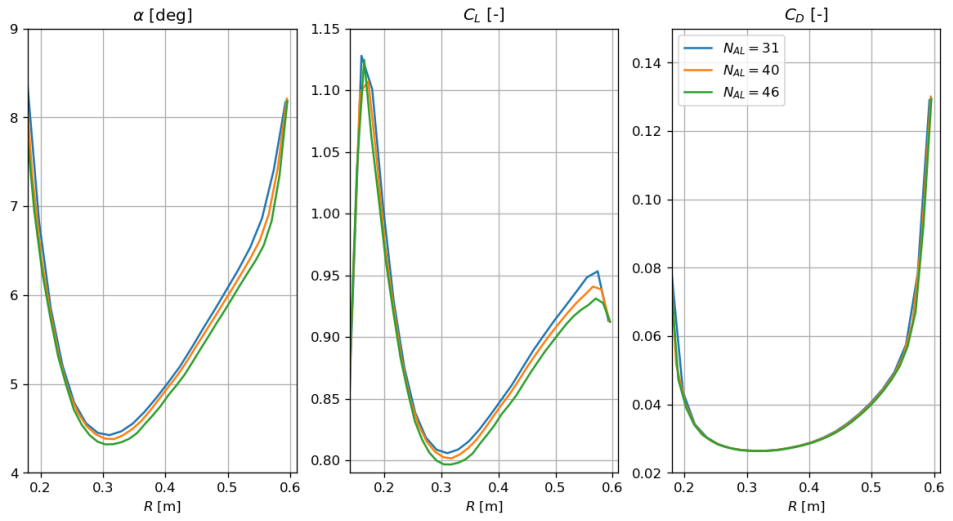

Figure 4.8: Impact of the mesh resolution in the rotor region on the mean radial loads

Furthermore, one can compare the development of the wake downwind of the rotor. The wake

deficit is plotted at four locations Figure 4.9. In the near-wake, the three configurations show very similar trends, as significant differences start to appear at $z = 3D$. Then, the configuration with the lowest resolution tends to overestimate the velocity deficit in most regions except at the centre, where it is underestimated.

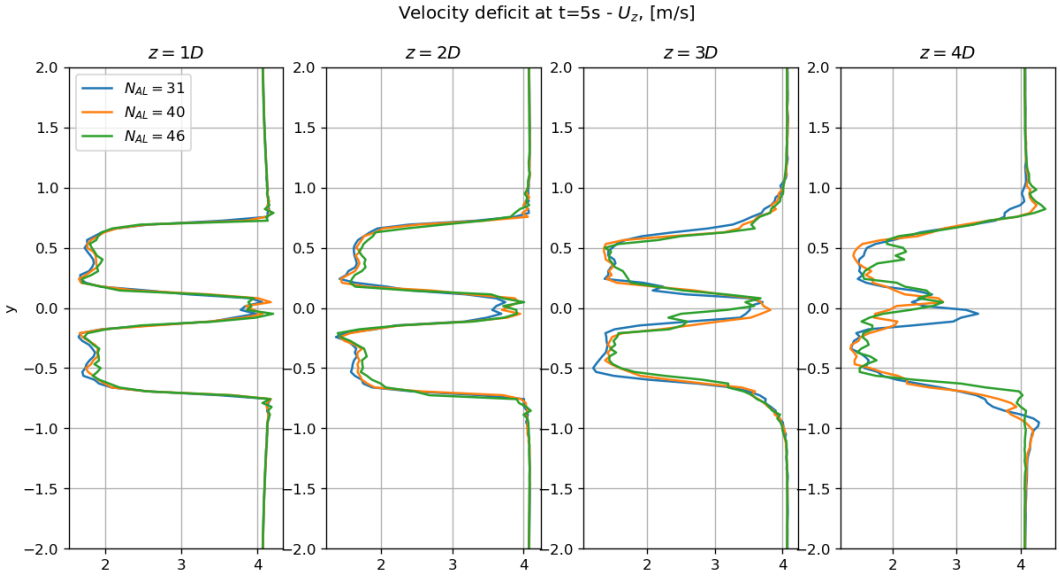

Figure 4.9: Impact of the mesh resolution in the rotor region on the instantaneous velocity deficit at four locations and $t = 6.0\ s$

In brief, the impact of blade discretisation has been investigated and quantified. It was found that, even the lowest resolution (still satisfying the recommended $N_{AL} \geq 30$) showed great results, and differences with the highest resolution remained small. On the other hand, the difference in number of mesh elements and, thus, in computational cost is much more significant. Therefore, it was chosen to keep a resolution of the order of $N_{AL} = 31$.

Finally, it is essential to precise that the mesh resolution is not only important for the actuator lines discretisation, but it should also be checked that a sufficient part of the flow is solved. This will be discussed later in subsection 4.1.6.

4.1.5. Discretisation scheme

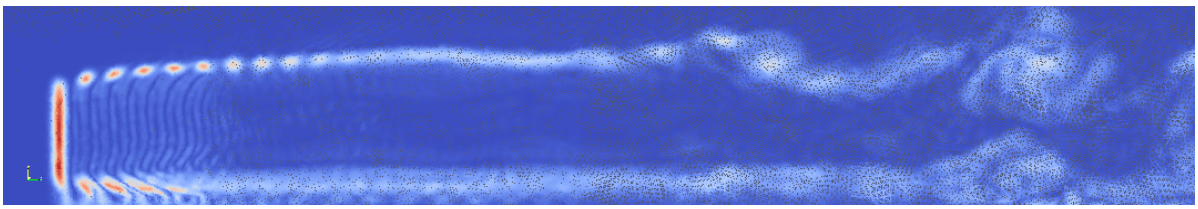

(a) 4th order

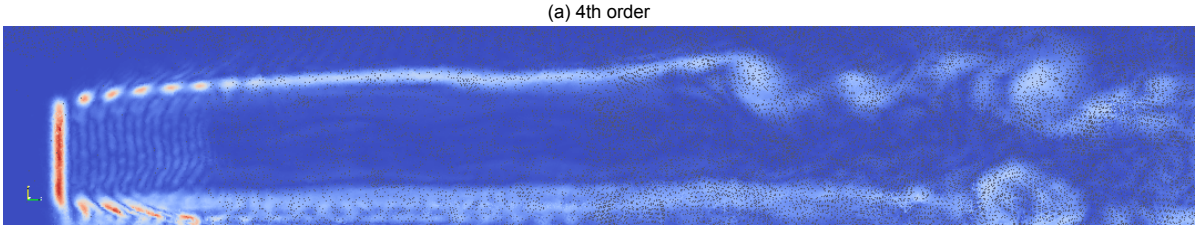

(b) 2nd order

Figure 4.10: Impact of the spatial discretisation on the wake development, plane $x = 0$ and $t = 6\ s$

The YALES2 implementation allows the user to choose between a central 4th-order scheme and a central 2nd-order scheme for the approximation of the fluxes for spatial integration. A similar simulation

to the original one with a 2nd-order scheme was run in order to estimate the impact of such a choice.

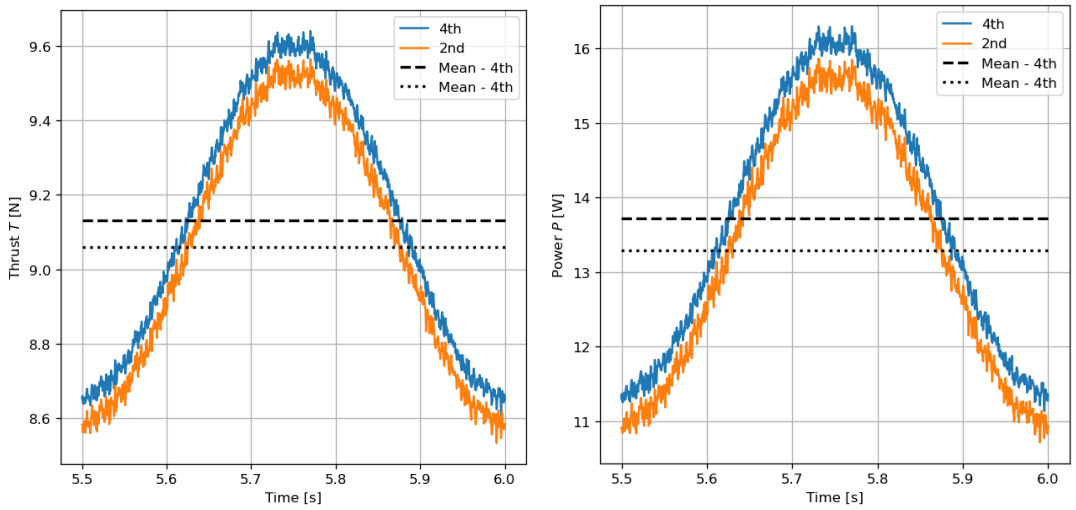

(a) Thrust (b) Power

Figure 4.11: Impact of the spatial discretisation on the loads, including the averaged solutions over one motion period

The thrust and power for the two configurations and during one surge motion period are plotted Figure 4.11. The loads are slightly shifted downward with the lower-order scheme. The relative differences are only about 0.8% for the thrust and 3.2% for the power.

Then, one can look at the development of the wake and, in particular, the root and tip vortices. For this purpose, the vorticity fields in the plane perpendicular to the rotor ($x = 0$) are given Figure 4.10. If the disparities between the two fields are not obvious, they still exist. In the near wake, more diffusion can be observed for the 2nd-order scheme, especially near the tip vortices and in the region between the root and tip vortices. In addition, the progress of the tip vortices is slower for the 2nd-order scheme as the space in between every tip vortex is smaller. Larger differences in the wake appear later in the wake. This can be confirmed by looking at the velocity deficit plotted Figure 4.12. Yet, the main vortical structures are conserved in the two simulations.

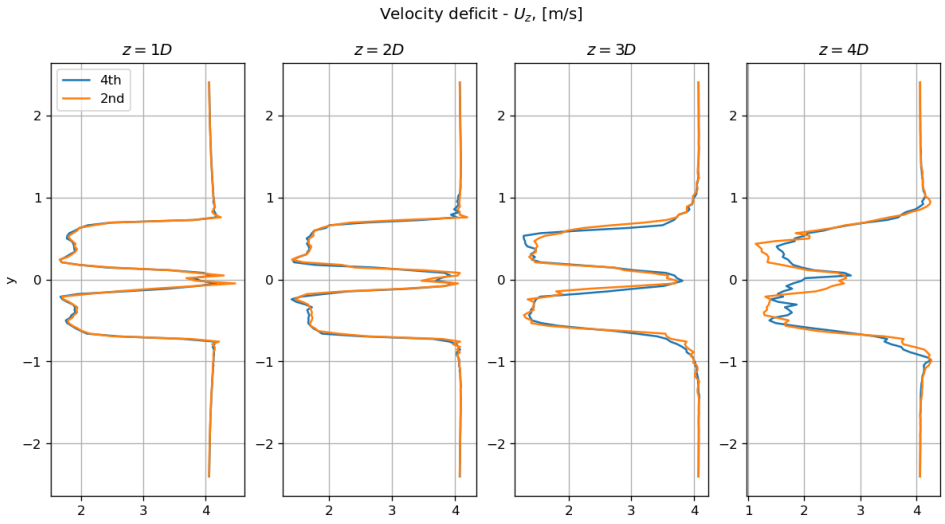

Figure 4.12: Impact of the spatial discretisation on the instantaneous velocity deficit at four locations and $t = 6.0\ s$

In conclusion, the use of a reduced order scheme has been shown to slightly underestimate the loads and affect the development of the tip vortices, which notably create larger differences in the mid-wake. In addition, no particular saving on computational time was made. Therefore, it is chosen to

continue with the central 4th-order scheme.

4.1.6. Final choice simulation parameters

The conclusions of the previous tests, motivated by a compromise between accuracy and computational cost, are summarised below:

- Time step: $CFL = 0.65$, to ensure the tip cross only 1 cell per time step
- Domain: $6D \times 6D \times 10D$ ($3D$ after inlet) to avoid the blockage effect and capture a sufficient part of the wake flow
- Actuator line resolution: $N_{AL} = 32$, to compute the loads accurately while keeping a reasonable number of cells
- Spatial discretisation: 4th-order central scheme to better capture the tip vortices and better estimate the loads

A new mesh was created by slightly modifying the previous one. Except for the domain size and the blade resolution discussed above, the refinement regions were also slightly extended in the $x-$ and $y-$ direction to ensure the tip vortices and the borders of the wake remain in the regions of thinner mesh resolution. A cross-section view of the mesh is represented Figure 4.13.

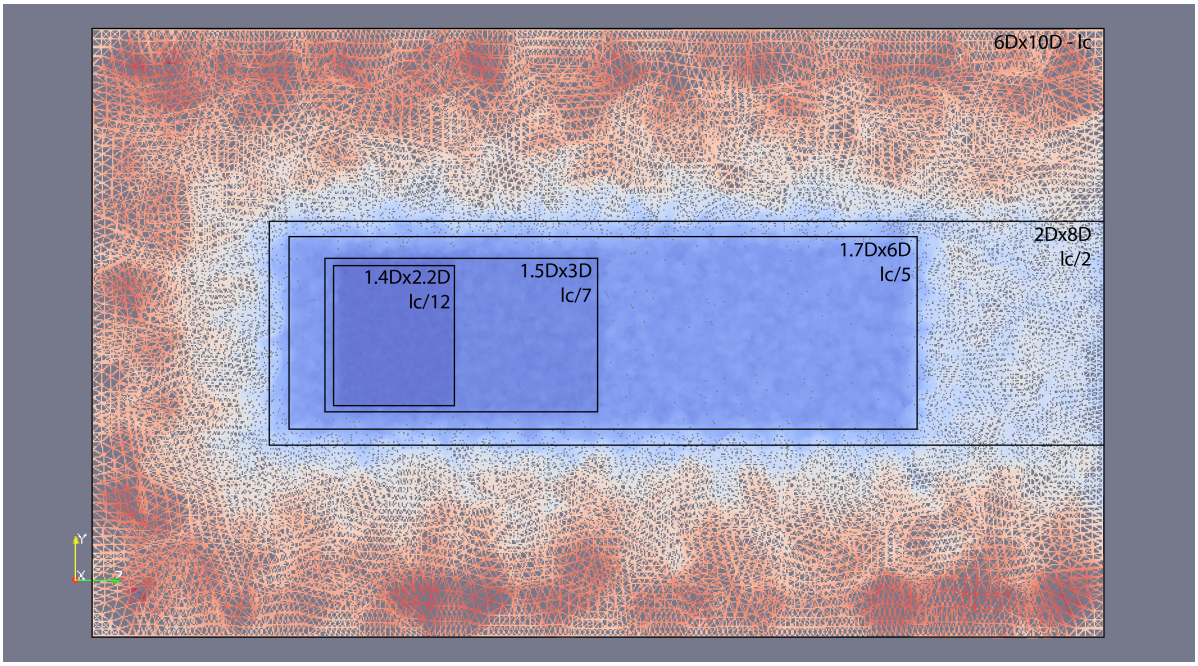

Figure 4.13: Mid plane ($x = 0$) slice of the final mesh, coloured by cells volumes, $lc = 0.5\ m$

Lastly, the mesh resolution required for the simulations is not only dictated by the actuator lines discretisation. As mentioned earlier, in LES, the mesh needs to be fine enough so that a sufficient amount of the turbulence scale is resolved. It is generally advised that at least 80% of the turbulent kinetic energy should be resolved [81]. In order to verify if a sufficient part of the turbulence within the flow is resolved, one can use the criterion proposed by Pope [93]. He suggested that as a measure of turbulence resolution, to look at the fraction of the turbulent kinetic energy in the resolved motions $M(x,t)$. Here, the turbulent kinetic energy actually resolved is compared with the turbulent kinetic energy modelled by the SGS model:

$$M(x,t) = \frac{k_{SGS}}{k_{SGS} + k_{res}} \tag{4.1}$$

Therefore, the value of M is between 0 and 1. If $M = 0$, all the turbulent scales are resolved, which corresponds to DNS. If $M = 1$, all the turbulence is modelled and not resolved, similarly to RANS.

Considering the 80% threshold for sufficient LES, this requires obtaining $M \leq 0.2$ at any time and everywhere in the flow.

The Pope's criterion has been evaluated, as an example, on a surge case defined by $\Delta V_S^* = 0.1$ and $f_s = 5\ Hz$. The cross-section view in the $x = 0$ plane is given in Figure 4.14. Since the problem is axis-symmetric, only the cross-section view is given. In addition, it is shown only at $t = 6\ s$ as no significant dependence on time for the criterion was found.

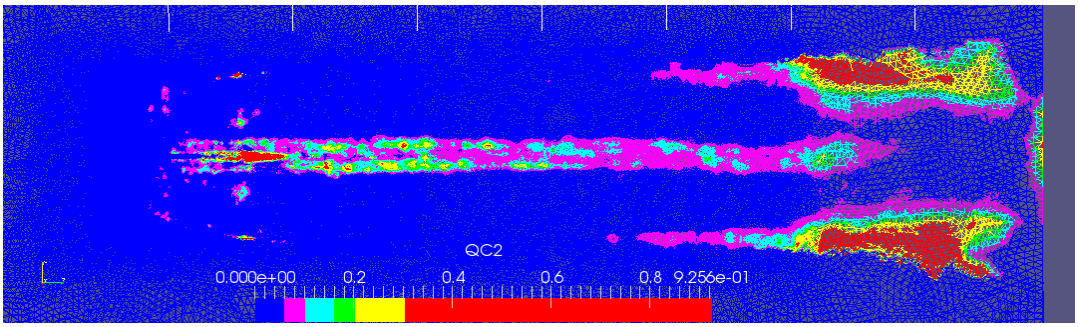

Figure 4.14: Cross-sectional view of Pope's criterion for a surge case, $\Delta V_S^* = 0.1$ $f_s = 5\ Hz$, white lines every $z = 1D$

In most of the field, the flow is very well resolved with $M \leq 0.05$ (blue regions in Figure 4.14). The quality of the mesh decreases in the central region, where the root vortices bring a large amount of turbulence. The quality of the mesh also decreases in the far-wake where the mesh is relatively coarse. The yellow ($0.2 \leq M \leq 0.3$) and red ($M \geq 0.3$) regions correspond to the locations where less than 80% of the turbulence scale is resolved. In the near and mid wake, these regions remain small. Regions of poor resolution appear around $z = 0.55D$ at the tip and particularly at the root vortices. This location corresponds to the end of the rotor's refinement region. On the other hand, at the far wake, larger regions of low resolution appear after the end of the wake's refinement region. This is a direct consequence of the choice to disregard this region, as it barely impacts the rotor loads. Globally, the mesh resolution is sufficient for the objectives of the simulations, even though an improvement could be made at the tip and root vortices in the near wake.

In the rest of this report, and if not precised otherwise, the numerical configuration described in this part was used to obtain the results presented.

4.2. Impact of some parameters

In addition to the convergence study performed for the main parameters of the simulation, this section tries to estimate the impact of some other choices made or imposed.

4.2.1. Reynolds number influence

As mentioned earlier, an error was introduced by generating the polars for a certain Reynolds number radial distribution calculated before the simulation. Even though it was justified by the dominant term being the rotational velocity in the calculation of the Reynolds number, the impact of this assumption needed to be checked. This is particularly critical as the differences in lift and especially in drag coefficients are significant between the case $Re = 30k$ and the others, as shown Figure 4.15.

Verification on surge imposed motion

First, the Reynolds number distribution calculated to generate the polar was compared with the mean distribution actually encountered by the blades. This was evaluated for a surge-imposed motion with the following characteristics: $U_\infty = 4.0\ m/s$, $\Omega = 480\ RPM$, $\Delta V_S^* = 0.05$ and $f_S = 2\ Hz$. The comparison is plotted Figure 4.16.

From the Figure 4.16, it appears that the Reynolds number distributions are very similar. Furthermore, the largest differences are encountered at the root region, which is not the most crucial for load estimation. This tends to confirm the assumption that the loads do not significantly alter the calculation of the Reynolds number, as the rotational speed is the dominant term. However, the comparison is made with only the average in time, and the unsteadiness introduced by the motion in particular could introduce errors not seen here. Therefore, a second verification was performed.

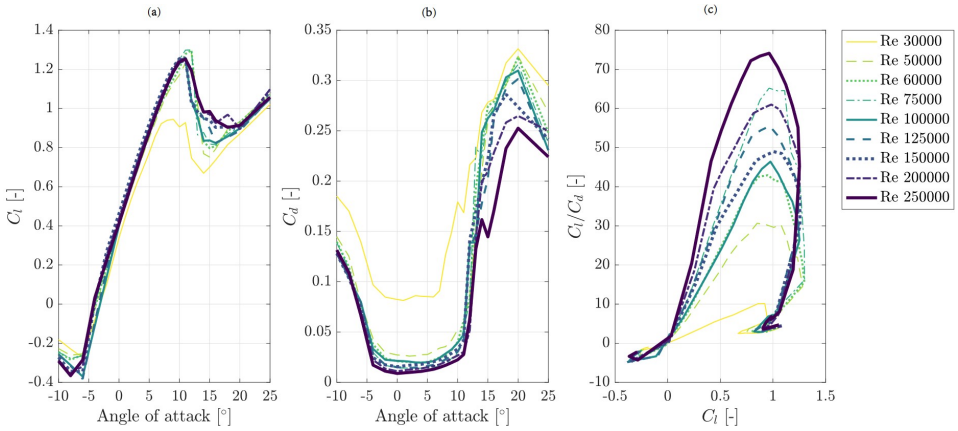

Figure 4.15: Aerodynamic coefficients of the SD7032 airfoil for several Reynolds numbers. (a) Lift coefficient. (b) Drag coefficient. (c) Lift-to-drag ratio, [85]

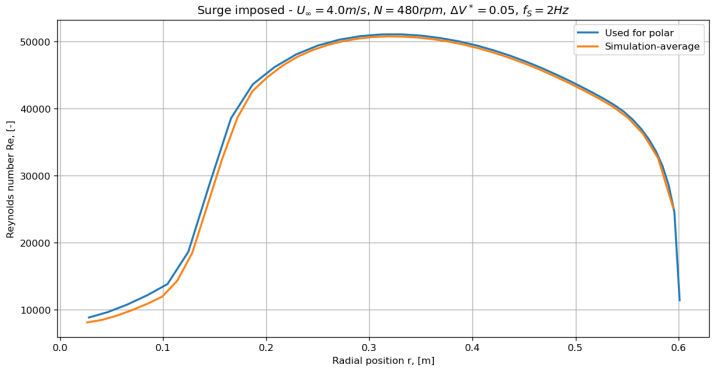

Figure 4.16: Reynolds number radial distributions, calculated beforehand (blue) and averaged over the simulation (orange)

Verification on static cases

If the loading has been shown to have little effect on the average Reynolds distribution, the question of whether the motion generates significant variations in lift and drag coefficients still needs to be addressed. The biggest difference would appear when the rotor is coming back to its initial position and the velocity is at its extremes ($U_r = U_\infty \pm \Delta V$). In order to clear this issue, two static simulations were performed and compared. In the first one, the freestream velocity was set to $U_\infty = 4.2\ m/s$ corresponding to $4.0 + \Delta V$ for $\Delta V^* = 0.05$ and all the parameters were set as usual in order to get accurate results. The second simulation is exactly the same except for the polars used as inputs. For this one, the polars were generated for $U_\infty = 4.0\ m/s$ even though it is not the right freestream velocity, in order to mimic what occurs during the motion when the velocity as seen by the rotor is at its maximum. The loads (thrust and power in particular) were obtained and plotted Figure 4.17.

From the Figure 4.17 it appears that the loads are very similar. Indeed, the error on the averaged values is lower than 0.1% on the thrust and lower than 0.48% on the power, which is largely negligible. It should be noted that the slight decrease in loads that can be observed on the plots is only due to the wake that is not fully developed at $t = 1.4\ s$, but they converge to their final values around $t = 1.8\ s$.

In brief, this means that, even when the motion velocity is at its maximum, the impossibility of using Reynolds-dependent polars does not introduce any significant error, and the loads are still computed accurately, at least for this reduced velocity.

4.2.2. Tower and nacelle

The presence of other elements surrounding the rotor, including the tower and the nacelle, can greatly affect, not only the wake behaviour, but also the loads. Their aerodynamic interactions can be complex and can be estimated by modelling them the same way the rotor is, using actuator lines. However, the accuracy of such a method to model the tower and the nacelle is not as clear as for the rotor, and

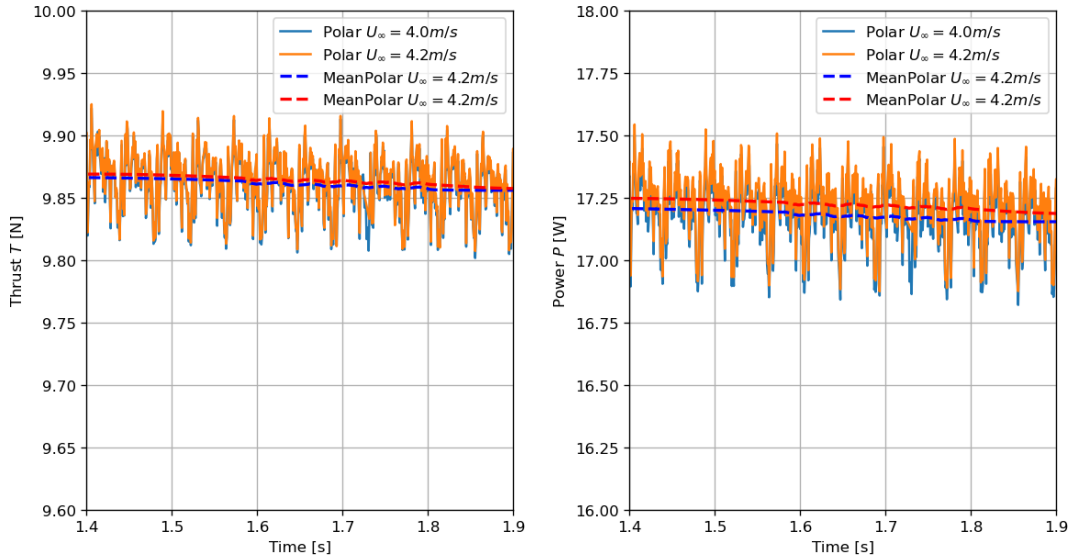

(a) Thrust (b) Power

Figure 4.17: Loads for the static case $U_\infty = 4.2\ m/s$, $N = 480\ RPM$, polars generated for $U_\infty = 4.0\ m/s$ and $U_\infty = 4.2\ m/s$, including the filtered solutions (dashed lines)

is rarely investigated in the literature. This technique is possible to use in YALES2, but no published article using it was found. Therefore, one should be cautious with its use.

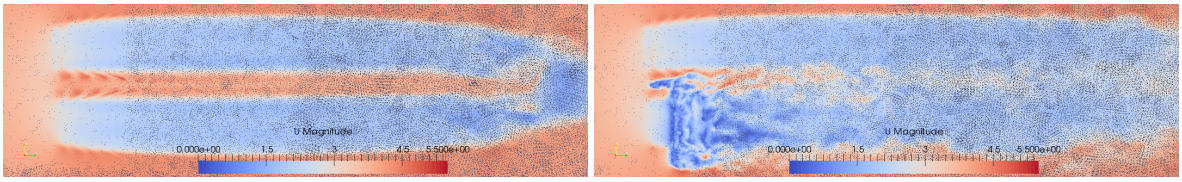

(a) (b)

Figure 4.18: Impact of the tower and nacelle on velocity field, plane $x = 0$

Yet, two simulations, with and without the tower and nacelle, were performed in order to estimate their influence on the rotor's performance and the wake's behaviour. The case in consideration is a static one, with $U_\infty = 4.0\ m/s$ and $\Omega = 480\ RPM$. The simulations were run on a smaller domain ($4D \times 4D$ in the rotor's plane) and with linear interpolation for the polars. Therefore, the absolute values are not directly comparable with the results presented in the next section, the focus here is on the differences between the two configurations.

In the experiment, the geometries of the tower and the nacelle are not scaled down from the full-scale turbine but are mainly driven by experimental constraints. It was chosen to mimic the experiment.

The tower is a cylinder and was modelled with an actuator line of length $L_T = 81\ cm$ and a chord equal to its diameter $D_T = 7\ cm$. The aerodynamic coefficients are fixed and equal to $C_{L,T} = 0$ and $C_{D,T} = 0.6$.

The nacelle, on the other hand, is a cuboid. Its length is $L_N = 24\ cm$ and its width $c_N = 5\ cm$. This gives an equivalent diameter of $D_{e,N} = 5.4\ cm$. The aerodynamic coefficients are fixed and equal to $C_{L,N} = 0$ and $C_{D,N} = 1.2$.

First, the impact of the nacelle, and the tower in particular, can be clearly observed by looking at the velocity deficit field given in Figure 4.18. The velocity in the wake drops near the nacelle and in the region downwind of the tower. This breaks the symmetry present in the case without these elements.

Then, the tower and the nacelle also impact the loads on the rotor. The thrust and power are plotted Figure 4.19. Two remarks can be made, applying to both the power and the thrust. First, the mean values are shifted downward when the tower and nacelle are included. With these additional elements, the thrust decreases from $T = 9.4\ N$ to $T = 9.3\ N$ (about 1% relative difference), and the power

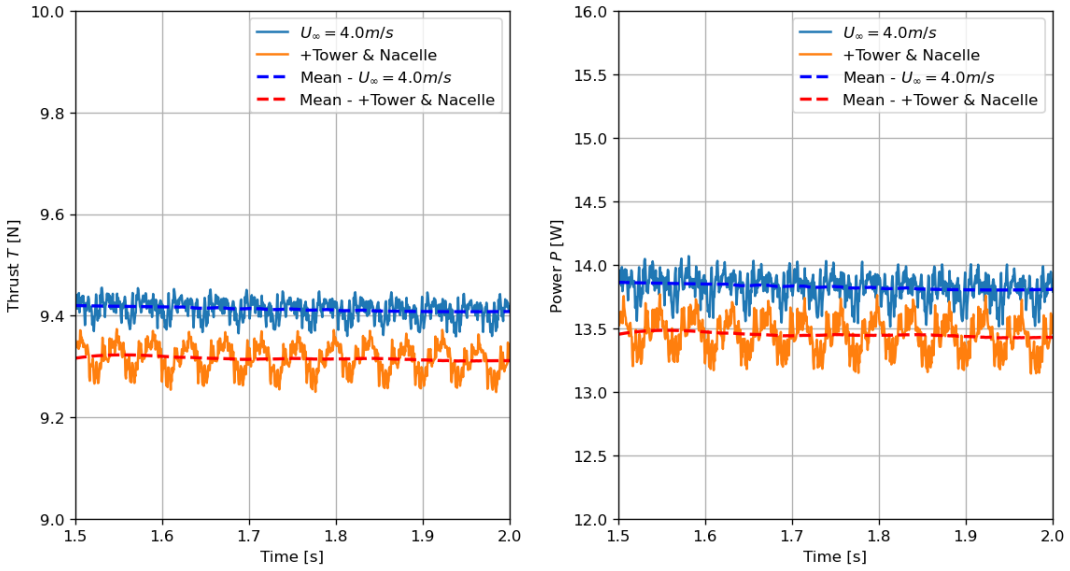

(a) Thrust (b) Power

Figure 4.19: Impact of the tower and nacelle on the loads, including the filtered solutions (dashed lines)

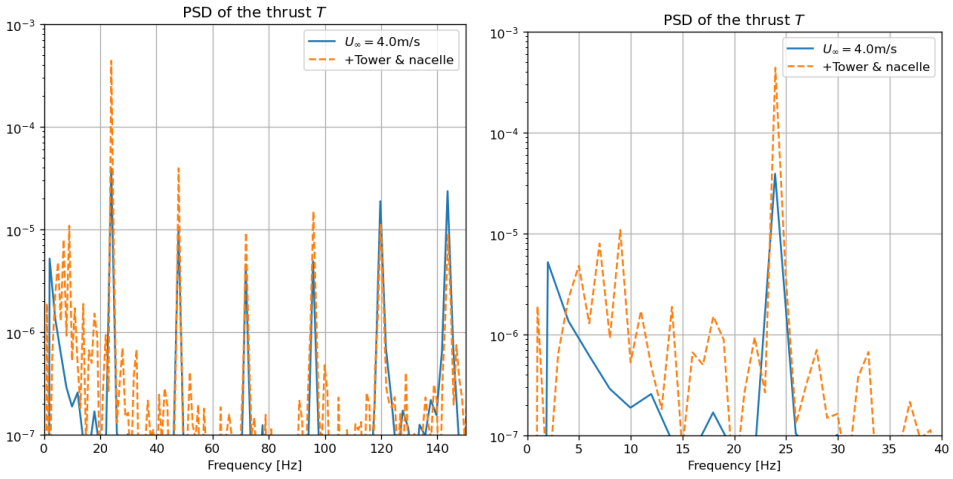

(a) (b)

Figure 4.20: Impact of the tower and nacelle on the power spectral density of the thrust, b) is zoomed on low frequencies

decreases from $T = 13.8\ N$ to $T = 13.4\ N$ (about 3% relative difference). Therefore, the difference in the mean loads remains relatively small. Second, larger periodic variations appear when the tower and the nacelle are added. This can be of significant importance when looking at fatigue loads, for instance. In order to look more precisely at those periodic variations, the power spectral densities of the thrust for the two simulations are plotted Figure 4.20.

Both spectral signals are dominated by the peak around $f = 24\ Hz$ and its harmonics. Their amplitude is slightly different, with the peaks being higher with the nacelle and the tower for the first harmonics and the trend inverting after. The first peak at 24 Hz corresponds to the low frequency variations that are easily noticeable on the loads Figure 4.19 and its amplitude is more significant with the additional elements taken into account. Other differences between the two signals exist in the low frequencies. If the peaks are not identified precisely, it is interesting to note that the frequency associated with the shedding vortices downwind of the tower is in this range. Indeed, in the book of Katopodes [94], it can be found that there is a relation between the Reynolds and Strouhal numbers for flows around a cylinder. For a diameter-based Reynolds number of about $Re = 19000$, the Strouhal number is around $St = 0.2$. This gives a frequency of the shedding vortices of about $11\ Hz$.

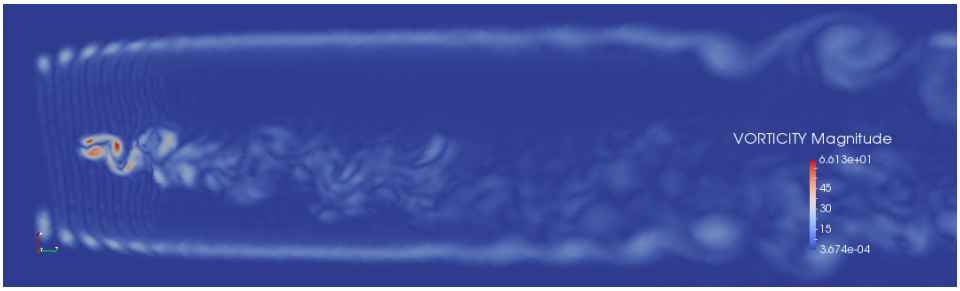

Figure 4.21: Vorticity field in plane $y = -0.3\ m$

Those shedding vortices can clearly be seen in Figure 4.21 where the vorticity field in the plane $y = -0.3\ m$ is given. One can see the tip vortices forming from the blades and, in the middle, the shedding vortices evolving from the tower. It can be noted that these vortices, as they diffuse, are deflected because of the rotation of the tip vortices.

To conclude, an actuator line approach was used to model the impact of the tower and the nacelle. It was found that their impact on the loads remained relatively small, decreasing slightly the mean loads but increasing a bit the variations. On the other hand, the impact on the near wake is significant as vorticity is added near the nacelle and behind the tower, where the wind velocity drops.

4.2.3. Wind tunnel effect-corrections

In the experimental setup, the $1.2\ m$ rotor is placed at the exit of the $3m$ equivalent diameter nozzle. The blockage effect and the other interference effects, such as jet expansion, are taken into account by modifying the inlet velocity according to the method described by Mercker and Wiedemann [95]. In their work, they proposed correction factors to account for interference effects that are occurring within open jet wind tunnels. The corrected wind speed becomes:

$$U_{cor} = \frac{U_\infty}{1 + \sum \epsilon_i} \tag{4.2}$$

Wherein ϵ_i are the different correction factors. Three interference effects are taken into account: the one corresponding to the jet expansion, the collector blockage, and the nozzle blockage (the dominant one in this setup).

In the experiment, for a freestream velocity of $U_\infty = 4\ m/s$, the corrected velocity becomes $U_{cor} = 4.063\ m/s$. This represents only a 1.6% relative difference in the freestream velocity.

A simulation was run in order to estimate the impact of such a correction. The surge case considered is the same as the original simulation presented earlier. However, the simulations were run on a smaller domain and with a linear interpolation for the polars. Therefore, the values might differ slightly, but the main focus here is the difference between the simulations with and without the corrected velocity.

The thrust and the power generated by the rotor are plotted for one surge period in Figure 4.22. There is not any significant difference between the two simulations in terms of phase shift or amplitude of variations. However, as expected, the loads are higher with the corrected increased velocity. Yet the relative difference between the mean values remains moderate: 1.6% for the thrust and 5.4% for the power.

One can also look at the velocity deficit in the near wake. It is plotted in Figure 4.23 along a line in the $y-$ direction for $x = 0$ and $z = 2D$. The velocity deficit shows a very similar shape. It is only shifted due to the slight increase in the freestream velocity.

To conclude, the wind tunnel effects occurring in the experimental setup were accounted for by correcting the freestream velocity. The loads are slightly increased, but the same patterns are found in the near wake. Since the wind tunnel has a large open section, its influence on the flow remains modest.

4.3. Static cases - Comparison with AeroDyn results

Finally, and before moving on to the 1-DOF and 2-DOFs motions, the results are compared with BEM results on static cases. Indeed, multiple static computations were performed by Felipe and Federico be-

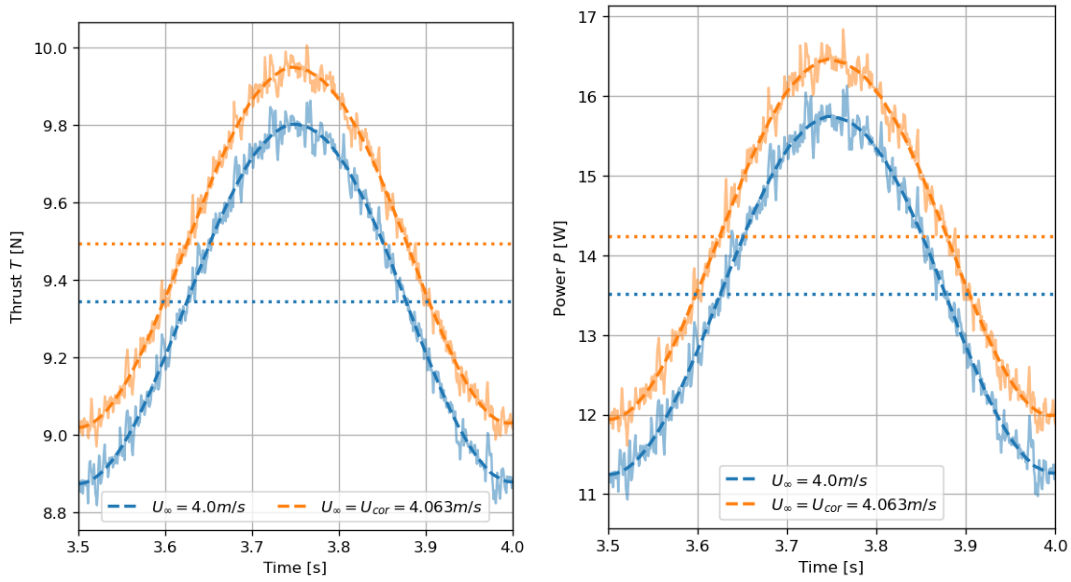

(a) Thrust (b) Power

Figure 4.22: Impact of the blockage effect on the loads, including the filtered (dashed lines) and averaged (dotted lines) solutions over one motion period

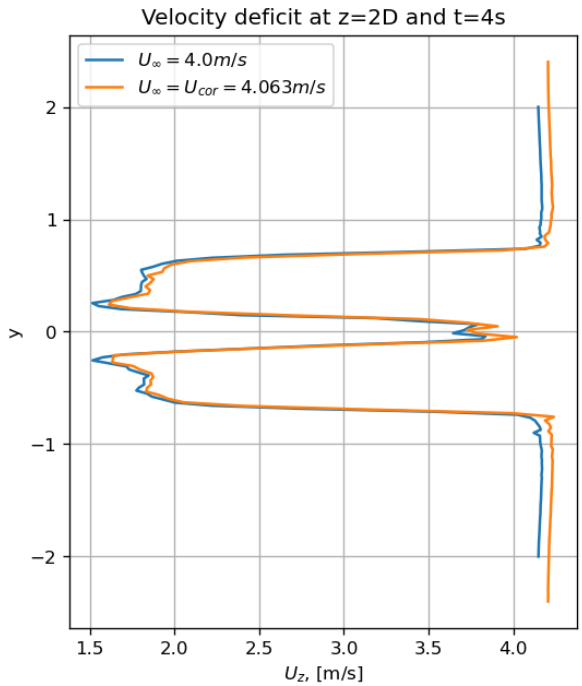

Figure 4.23: Impact of the blockage effect on the instantaneous velocity deficit at $z = 2D$ and $t = 4.0\ s$

fore the experimental campaign. They used FAST with the aerodynamic module AeroDyn14 (expected lower fidelity). They kindly provided their results for three cases with varying freestream velocities: $U_\infty = 3.8\ m/s$, $U_\infty = 4.0\ m/s$ and $U_\infty = 4.2\ m/s$. The rotational velocity is constant and equal to $\Omega = 480\ RPM$.

The results from FAST, in terms of mean thrust and mean power, are summarised and compared with YALES2's results in the Table 4.4. Two remarks can be made about these results. First, if the mean thrust forces obtained are very similar for the two methods, significant differences appear for the power. In addition, this relative difference in power increases as the freestream decreases.

	FAST - AeroDyn		YALES 2		Relative Difference, [%]	
Freestream velocity	T [N]	P [W]	T [N]	P [W]	T [N]	P [W]
$U_\infty = 3.8\ m/s$	8.59	9.25	8.75	11.56	1.87	24.97
$U_\infty = 4.0\ m/s$	9.17	12.24	9.26	14.12	0.98	15.36
$U_\infty = 4.2\ m/s$	9.74	15.25	9.76	16.7	0.18	9.48

Table 4.4: Comparison of AeroDyn results with YALES 2 on three static cases

Those static results can also be compared with the experimental ones. During the experimental campaign, and before every motion case, the static thrust was measured for both design freestream velocities $U_\infty = 2.5\ m/s$ and $U_\infty = 4.0\ m/s$. The results, provided by the experimentalists Federico Taruffi and Felipe Miranda Novais are plotted Figure 4.24. Great variations were found in the static thrust. For the cases with $U_\infty = 4.0\ m/s$, the thrust is $T_{exp} = 9.56 \pm 0.41\ N$. Therefore, the static thrust obtained with YALES 2 is in the acceptable range, especially considering the slight increase induced by the blockage effect within the wind tunnel.

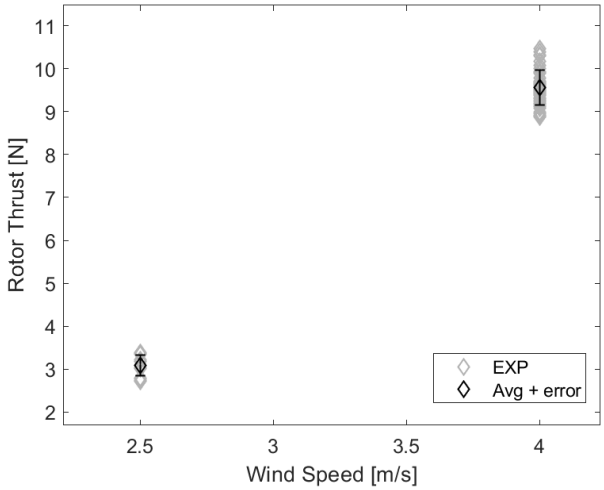

Figure 4.24: Experimental thrust measurements in static conditions, courtesy of Federico and Felipe

In order to obtain more insight on the discrepancies between YALES2 and AeroDyn results, one can look more precisely at the radial distribution of the loads along the blades. The angle of attack α as well as the lift and drag coefficients, C_L and C_D, are plotted Figure 4.25 for the three wind speed velocities investigated before. For a clearer comparison, the distribution of the relative difference between the two simulations is also plotted.

Therefore, one can note that the differences are significant. Again, they globally increase with the decreasing freestream velocity. If the differences are low at the root, they start to increase as the chord increases. A peak is observed on both the angle of attack and lift coefficient around $R = 0.18\ m$, where the blade chord is the largest. As the chord decreases almost linearly (see Figure 4.6), the differences in angle of attack and lift coefficient follow a similar trend. The discrepancies then increase near the tip. The fact that the differences in lift coefficient and angle of attack show a similar trend is simply explained by the fact that they have an almost linear relation in this range of angles of attack ($[0°; 10°]$). On the other hand, the differences in drag coefficient show a different trend and more significant values. The main differences are located at the outboard part of the blade (around $R = 0.5\ m$) and right at the tip. The tip region is a complex region where the flow is highly three-dimensional. For both BEM and lifting line approaches, the loads in this region highly depend on the use, or lack thereof, of a tip correction method. However, because the chord is very small in this region, only a minor part of the total loads is carried in this region. On the other hand, the peaks in relative difference in C_D around $R = 0.2\ m$ and $R = 0.5\ m$, can explain larger discrepancies in the torque and power, which are mainly drag-dependent (in opposition to the thrust, which is driven by the lift). This is particularly true for the smallest freestream velocity, $U_\infty = 3.8\ m/s$.

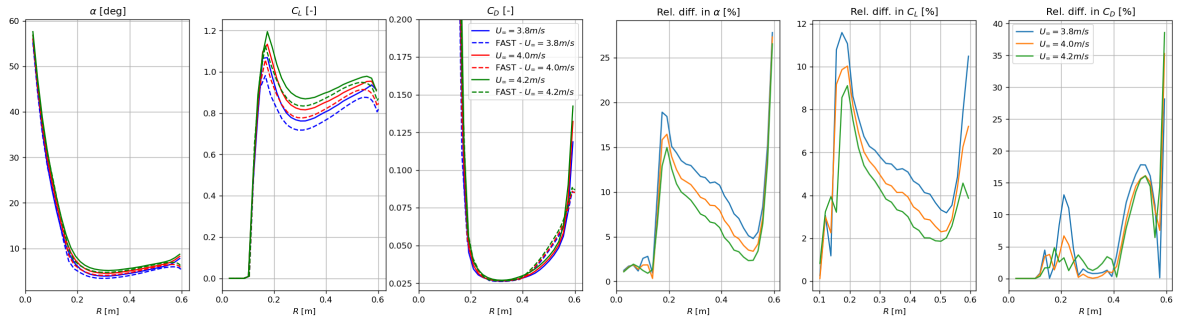

(a) (b)

Figure 4.25: Radial distribution of α, C_L and C_D with the relative difference between YALES2 and AerodDyn results

This ends this chapter on the validation of the numerical setup, whose main characteristics were described in subsection 4.1.6. It should be mentioned that another turbulence model frequently used for wind turbine applications was tried: the σ-model [74]. However, as previously observed in the literature, no significant difference could be noticed on the wake or on the loads, and the dynamic Smagorinsky was kept.

Using this numerical setup, surge and pitch motions can now be imposed.

5

1 DOF - Surge imposed motion

This chapter presents the results obtained for one-degree-of-freedom harmonic motions in the surge direction. The temporal evolution of the loads, both at rotor and blade levels, but also the behaviour of the near and mid-wake, are looked at.

5.1. Cases description

As described previously, a vast range of harmonic surge motions have been investigated during the experimental campaign, they will not all be simulated. First, and because the experimental results obtained for $U_\infty = 2.5\ m/s$ were of poorer quality, only simulations at $U_\infty = 4.0\ m/s$ were run. Then, two reduced velocities were chosen in order to study the impact of this parameter: $\Delta V^* = 0.05$ and $\Delta V^* = 0.1$. They were chosen among the largest reduced velocities in order to avoid a too small motion amplitude and have significant load variations to measure. For harmonic motions, the other parameter is the frequency. Again, multiple frequencies were considered at each reduced velocity in order to quantify its impact. Finally, four 'extreme' cases with high reduced velocities were simulated, but there are no experimental results for those configurations. The objective behind those cases will later be explained in section 5.5.

The surge velocity is prescribed as follows:

$$V_{p,s} = A_s\,(2\pi f_s)\cos\,(2\pi f_s t) = \Delta V_s^* U_\infty \cos\,(2\pi f_s t) \tag{5.1}$$

The surge cases considered are summarised in the Table 5.1. The amplitude of the motion, computed from the reduced velocity, and the frequency are also given.

Case	ΔV_s^* [-]	f_s [Hz]	A_s [cm]
S005f1	0.05	1	3.18
S005f2	0.05	2	1.59
S005f5	0.05	5	0.64
S01f05	0.1	0.5	12.73
S01f1	0.1	1	6.37
S01f2	0.1	2	3.18
S01f5	0.1	5	1.27
S075f15	0.75	1.5	31.83
S075f5	0.75	5	9.55
S1f2	1.0	2	31.83
S1f5	1.0	5	12.73

Table 5.1: Reduced velocity and frequency of the harmonic surge motion cases investigated

5.2. Rotor loads - Thrust and Power

In order to evaluate the performance of the turbine during motion, it is looked at the thrust and the power generated by the turbine (mean value and variations). The power is directly linked to the torque as the rotational velocity of the turbine is kept constant.

5.2.1. First reduced velocity - $\Delta V^* = 0.05$

FAST simulations, using the AeroDyn module, were only ran for the static cases. Therefore, a comparison with this low-fidelity model is not possible for the surge cases and the other motion cases. However, for this particular reduced velocity, one can use the static results in addition to the quasi-steady theory. Indeed, this $\Delta V^* = 0.05$ corresponds to a maximum and minimum velocity, as seen by the rotor, of $U_\infty = 4.2\ m/s$ and $U_\infty = 3.8\ m/s$. Therefore, according to the quasi-steady theory, thrust and power should oscillate between the two extreme static values. For example, AeroDyn's results suggest that the thrust in quasi-steady conditions should oscillate between 9.74 N and 8.59 N (ie $\Delta T = 0.57\ N$) around a mean value of 9.17 N (see Table 4.4).

Similarly, it is pertinent to compare the results obtained for these surge motions with the static simulations obtained with YALES2. The rotor loads are plotted Figure 5.1.

In addition, the detailed results for each case are summarised in the Table 5.2. FAST results are also reminded. Furthermore, the experimental results are also given for the corresponding cases. In the experimental results, the amplitude of variations and the phase difference is missing for the high-frequency case. This is because the power output was highly unsteady, with very large variations (above 16 W on average). From one period to another, the amplitude of power oscillations would significantly vary.

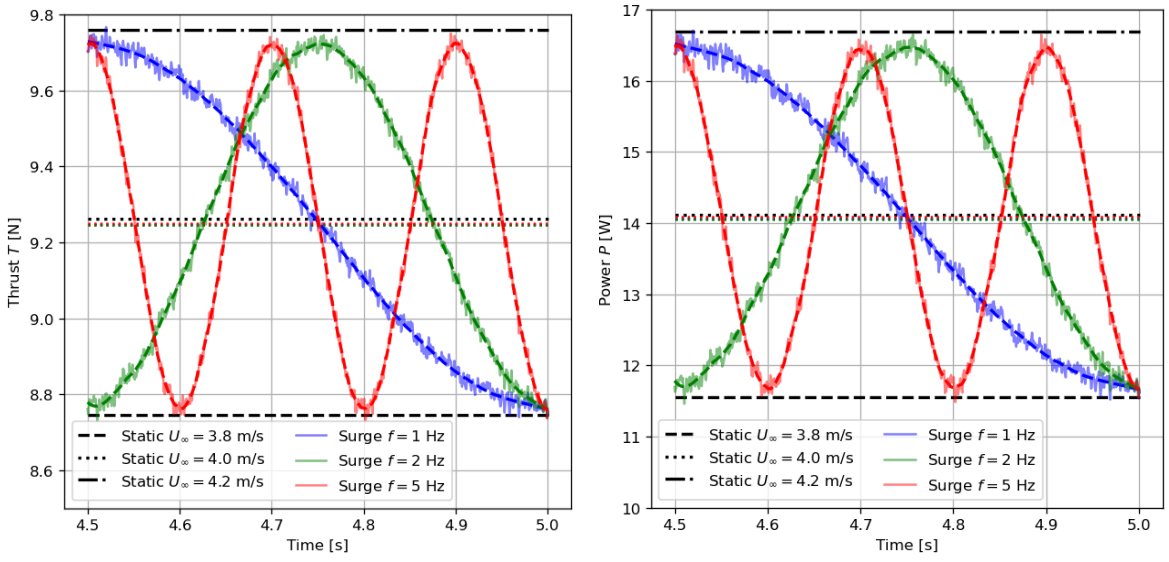

(a) Thrust

(b) Power

Figure 5.1: Thrust and power for surge motions with $\Delta V^* = 0.05$, including the filtered (coloured '–'), the averaged solutions over one motion period (coloured '..') and the static results (black lines)

From the graph and the detailed results, it appears that all the simulations run with YALES2 agree with the quasi-steady theory. Indeed, the amplitude of variations for thrust and power are similar for all frequencies. More importantly, they are very close to the amplitude expected from the static simulations performed with YALES2, even though a slight decrease is observed. In addition, the phase difference is very close to the theoretical value of $\phi = -90.0°$, especially for the low frequencies.

In comparison, the amplitude of thrust and power oscillations were expected to be larger from AeroDyn's results. This is explained by the observation made previously that the differences in static loads between the simulations and AeroDyn's results were found to increase with decreasing freestream velocity (see section 4.3).

A similar comment can be made for the comparison with experimental results, where larger os-

Source	Frequency [Hz]	$\overline{T}$ [N]	ΔT [N]	ϕ_T [deg]	$\overline{P}$ [W]	ΔP [W]	ϕ_P [deg]
Static FAST + QST	$\forall f$	9.17	0.57	-90	12.24	3.00	-90
Static YALES2 + QST	$\forall f$	9.26	0.50	-90	14.12	2.57	-90
YALES2	$f = 1$ Hz	9.24	0.48	-91.5	14.04	2.4	-91.4
	$f = 2$ Hz	9.25	0.48	-91.2	14.06	2.38	-91.2
	$f = 5$ Hz	9.25	0.48	-92.5	14.07	2.4	-92.4
Exp.	$f = 1$ Hz	9.43	0.57	-89.1	10.83	2.65	-91.7
	$f = 2$ Hz	9.39	0.59	-89.9	10.87	2.83	-94.0
	$f = 5$ Hz	9.36	1.37	-91.6	10.3	/	/

Table 5.2: Comparison of rotor loads for surge motion with $\Delta V^* = 0.05$

cillations were experienced for both the thrust and the power. On the mean values, the latter is underestimated in the simulations, and the former is significantly overestimated. On the phase shift, no significant difference can be observed when this output is measurable. An important outcome of the experimental results is that they found the low-frequency cases to respect the quasi-steady theory. On the other hand, for high frequencies such as $f = 5\ Hz$, the variations in thrust significantly increase, and all the more so for the power. This breakdown of quasi-steady theory for high frequencies is not observed in the numerical simulations and constitutes a substantial difference with the experimental results.

This important difference can be explained for various reasons.

First, it is worth mentioning that the freestream velocity in the simulations is not corrected for the wind tunnel effects. However, as investigated in subsection 4.2.3, the corrected freestream velocity only affects slightly the mean loads and not the amplitudes of variations. Therefore, it is very unlikely it would allow the breakdown of QST in the high-frequency case. On the other hand, one can note that this would, for all frequencies, decrease the difference in mean thrust and increase the difference in mean power.

Then, another limitation in the numerical simulations is the absence of change in the polars used. As discussed earlier, YALES2 cannot use Reynolds-dependent polars, but only one polar based on the estimated Reynolds radial distribution is generated before the simulation starts. If the impact of this assumption was not found to be significant, it is possible that it becomes relevant for high-frequencies changes.

Then, the main problem is believed to come from the mesh resolution around the rotor. The grid used probably does not permit sufficient capture of the motion of the rotor, whose amplitude is very small, and introduces unsteady effects. Indeed, for $\Delta V^* = 0.05$ and $f = 5\ Hz$, the amplitude of motion is $A = 0.64\ cm$. In comparison, this corresponds to about 1/100th of the rotor radius. Discretising the blade into 60 elements is considered a very fine resolution and generally represents a considerable computational cost. If the conservative guideline $\Delta_{AL} = 1.5\Delta_g$ [79] is used (in YALES2, there is $\Delta_{AL} \sim \Delta_g$), this configuration corresponds to mesh elements of the size about 1/100th of the rotor radius. Therefore, in this case, and for a conservative and very expensive mesh configuration, the amplitude is of the same order of magnitude as the size of the mesh elements near the rotor. This means that, during the motion, the blade elements only move within approximately three cells. In the configuration used here, with a lower resolution, the situation is even worse. Indeed, the mesh elements around the actuator lines have a size between 0.95 cm and 1.8 cm. This corresponds to a ratio between the motion amplitude and the mesh size of 0.7 and 0.4. In both cases, it is believed that such a low ratio (≤ 1) cannot capture unsteady effects. Therefore, it seems complicated to use actuator line LES for simulating cases with such low amplitudes of motion.

Complementary information on this high frequency/low amplitude case is discussed in subsection 5.2.4. In addition, the 'extreme' cases, whose results are discussed in section 5.5, are simulated in order to assess whether unsteady effects can be observed with a larger amplitude.

On the average loads, it was generally found in the literature that a surge motion increases the mean power and slightly decreases the thrust generated (in the absence of any control strategy). Here, both the mean thrust and mean power are found to decrease compared to the static values, especially at low frequencies. However, the differences are very small, and no significant conclusion can be drawn here.

5.2.2. Second reduced velocity - $\Delta V^* = 0.1$

Now, the reduced velocity is increased to $\Delta V^* = 0.1$, resulting in variations of $\pm 0.4\ m/s$ in the freestream velocity as perceived by the rotor.

Here, no FAST results are available to directly compare with the outputs of the simulations. In addition, there are no detailed results from the experimental campaign for these configurations. However, a similar trend than for the previous reduced velocity was found: the results are in accordance with the quasi-steady theory for the lowest frequencies and break down for high frequencies, in which ΔT significantly increases.

The time evolution of the thrust and the power are plotted Figure 5.2 and detailed in Table 5.3.

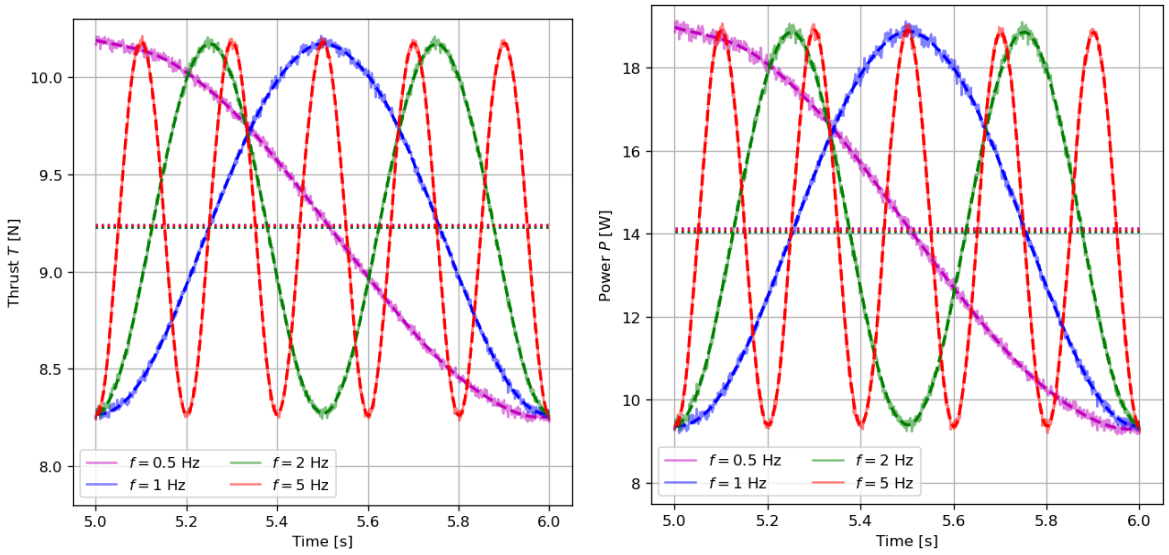

(a) Thrust (b) Power

Figure 5.2: Thrust and power for surge motions with $\Delta V^* = 0.1$, including the filtered ('–') and the averaged solutions over one motion period ('..')

Source	Frequency [Hz]	$\overline{T}$ [N]	ΔT [N]	ϕ_T [deg]	$\overline{P}$ [W]	ΔP [W]	ϕ_P [deg]
YALES2	$f = 0.5$ Hz	9.23	0.97	-91.9	14.05	4.82	-91.3
	$f = 1$ Hz	9.23	0.96	-92.1	14.05	4.79	-91.2
	$f = 2$ Hz	9.23	0.95	-91.5	14.06	4.73	-91.5
	$f = 5$ Hz	9.24	0.96	-92.6	14.09	4.76	-92.6

Table 5.3: Comparison of rotor loads for surge motion with $\Delta V^* = 0.1$

Regarding the results, similar comments can be made as for the previous reduced velocity. Indeed, one can observe a slight decrease in the mean thrust and mean power with the motion. The higher the frequency, the less important this decrease becomes, even though the differences are small. Then, for all frequencies, the amplitude of oscillations is almost the same. In addition, the phase shift for both power and thrust is very close to the theoretical value of $-90.0°$. Therefore, the four simulations with different frequencies all remain within the scope of the quasi-steady theory. Again, this differs at high frequency from the experimental results, and the same reasons can be advanced, even if the motion amplitude is slightly larger here.

In their work, Chen et al. [26] identified that the average power generation increased during the surge motion as the frequency or amplitude increased, but the average thrust remained constant. Here, a slight decrease is found in both the power and the thrust, without any significant impact from the reduced velocity.

5.2.3. Comparison with UNAFLOW project

It is also interesting to see how the numerical results compare with those of other experimental campaigns. In particular, the UNAFLOW project provided measurements of thrust variations and phase shift for a wide range of surge motions [34]. The experimental campaign used a similar approach to the one performed in Delft in April 2023 [83], and a slightly bigger rotor was used to scale down the same DTU 10MW. They notably measure the loads, for rated conditions ($\lambda = 7.5$), at two freestream velocities: $U_\infty = 2.5\ m/s$ ('RATED1') and $U_\infty = 4.0\ m/s$ ('RATED2').

In their work, they use the adimensionalised reduced frequency f_r defined in Equation 2.8. In addition, they define the unsteady thrust force coefficient as:

$$C_{\Delta T} = \frac{\Delta T}{\frac{1}{2}\rho\pi R^2 U_\infty^2} \tag{5.2}$$

They plotted this coefficient, divided by $A_r = A/D$ the reduced surge amplitude, with respect to the reduced frequency. They also plotted the phase shift obtained against the same reduced frequency for all the cases they investigated. Their results were retrieved and plotted with the numerical results presented above in Figure 5.3. Their QST prediction, obtained from the turbine operating conditions and its steady-state thrust coefficient characteristic, is also plotted (dashed line). The UNAFLOW campaign was also done on a scale model of the DTU 10MW, but with a larger rotor. Yet, the scaling was performed to mimic the thrust behaviour as well. Therefore, the adimensionalised quantities related to thrust are comparable.

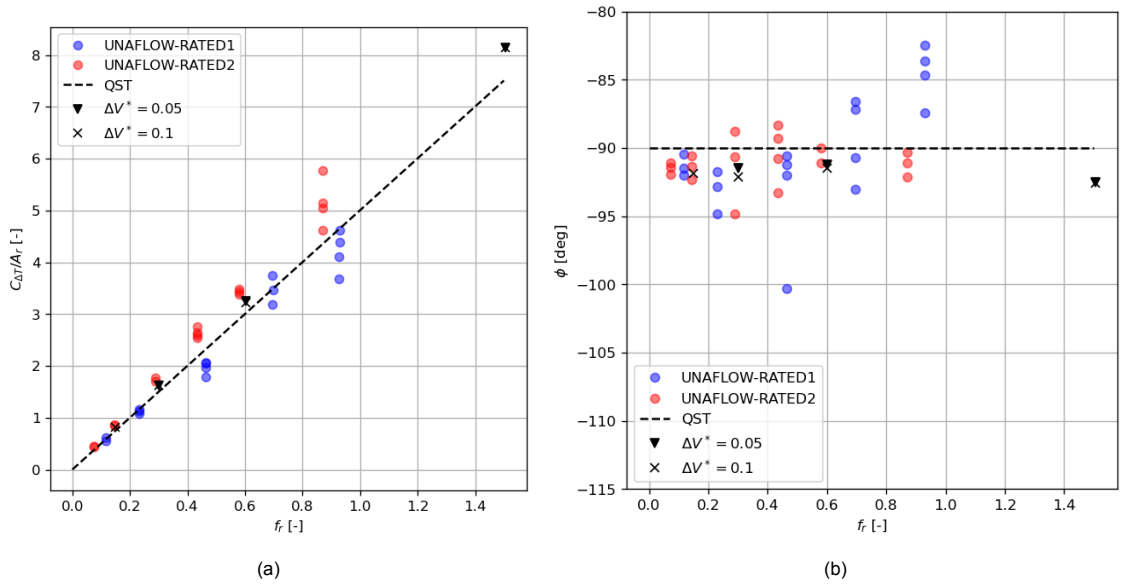

Figure 5.3: Unsteady thrust coefficient (a) and phase shift with surge motion (b) against reduced frequency, adapted from the work of Fontanella et al. [34] and extended with numerical results

Therefore, for the reduced frequency range investigated within the UNAFLOW project, the numerical results obtained compare well with their experimental ones. This holds for both the unsteady thrust coefficient and the phase shift. In addition, the results obtained for a higher reduced frequency continue to follow the same trend, in accordance with the quasi-steady theory. However, these points correspond to the ones where the QST was experienced to break down in Delft's experimental campaign [83].

5.2.4. High reduced frequency

As stated previously, breakdown of QST was experienced during the experimental campaign for high reduced frequencies (about $f_r \geq 1.2$, [83]). This was not observed in the numerical simulations. Two main limits of the numerical setup have been advanced to justify such a difference, among which figures the low mesh resolution compared to the amplitude of motion. Two new configurations on the case $\Delta V^* = 0.1$ and $f = 5\ Hz$ have been simulated in order to see if unsteady effects could be captured for this high reduced frequency case ($f_r = 1.5$).

Local Refinement

First, in order to obtain a bigger ratio of the amplitude of motion over the cell size near the rotor, the mesh was refined locally around the rotor.

Indeed, two refinement regions were added to the mesh used in the previous simulations. The first region is a cylinder of radius $1.4R$ and $40\ cm$ height centred around the initial rotor position, in which the cells have a width of about $lc/20$ before YALES2 refinement (as a reminder, the cells' width in the rotor refinement area is $lc/12$). Then, the mesh is refined again in a second cylinder, whose radius is $1.2R$, height is $20\ cm$, and cells' width is $lc/30$. Therefore, the size of the cells in the small region near the rotor is now divided by about 2.5. An illustration of the mesh is shown Figure 5.4.

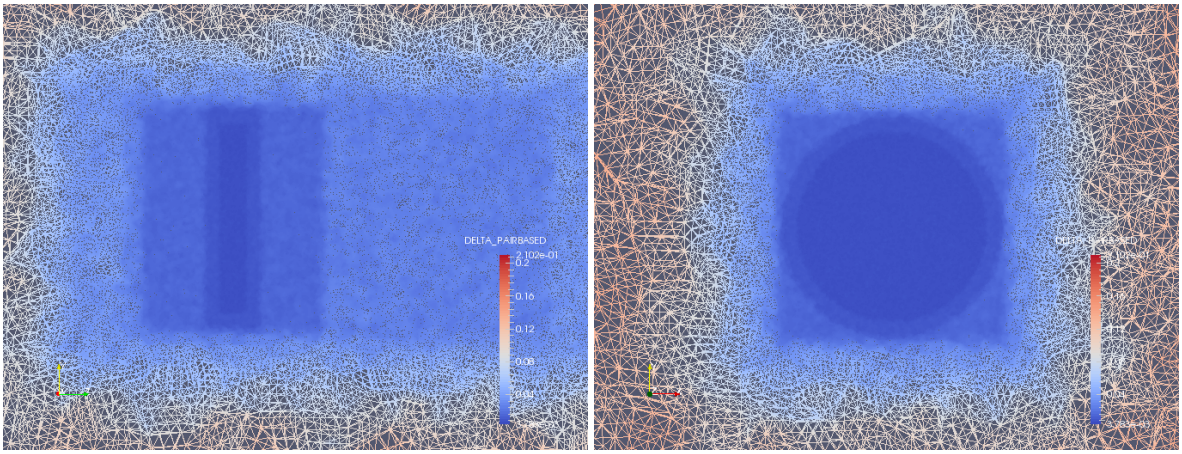

(a) $x = 0$ (b) $z = 0$

Figure 5.4: Mesh visualisation in two planes near the rotor, coloured by cells size.

In addition, one can get a better grasp of the improved resolution near the rotor by looking at the mean velocity source field. This is illustrated Figure 5.5. One can clearly see that, on the original mesh, the actuator force is only interpolated on a few elements along the $z-$axis, i.e. the direction of the surge motion. On the other hand, with the local refinement, the loads are interpolated, on average, on a much larger number of elements during the motion.

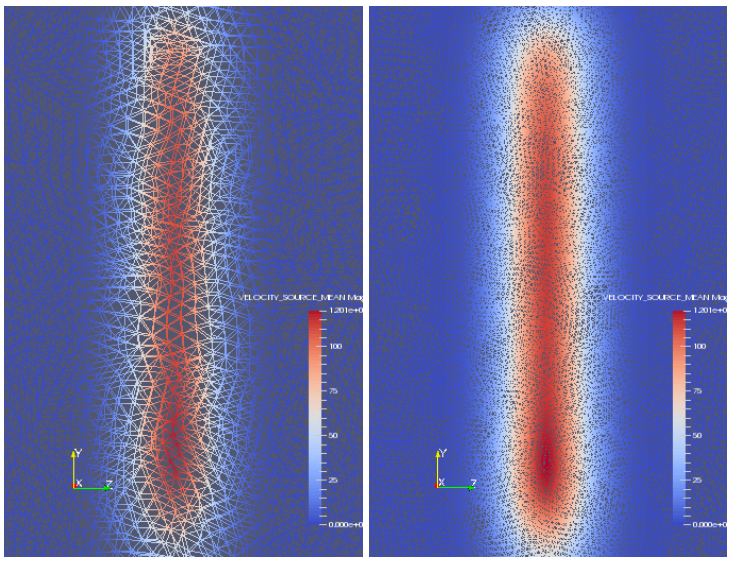

(a) (b)

Figure 5.5: Comparison of the mean velocity source on the original mesh (a) and with the local refinement (b), $\Delta V^* = 0.1$ and $f = 5\ Hz$

The details about the loads obtained with this new mesh are given in Table 5.4. Previous results

obtained for this motion case are also recalled.

Local refinement?	$\overline{T}$ [N]	ΔT [N]	ϕ_T [deg]	$\overline{P}$ [W]	ΔP [W]	ϕ_P [deg]	$\overline{dt}$ [ms]
No	9.24	0.96	-92.6	14.09	4.76	-92.6	0.59
Yes	9.34	0.97	-91.7	14.6	4.84	-91.5	0.24

Table 5.4: Impact of the local refinement on the power and thrust, $\Delta V^* = 0.1$ and $f = 5\ Hz$

Therefore, one can observe an increase in the mean loads, and a slight increase in the amplitude of oscillations. However, this cannot necessarily be attributed to the increased local resolution. Indeed, the CFL number was not changed between the two simulations, and the smaller mesh size led to smaller time steps. Indeed, the average time step dropped from 0.59 ms to 0.24 ms. The study on the impact of the CFL number performed in subsection 4.1.2 suggests that this difference in the mean loads is rather due to the smaller time step than the local refinement per se. Anyway, the load variations observed are still far from the values obtained experimentally, and the quasi-steady theory still holds. Therefore, this local refinement did not permit the capture of any unsteady effect. In addition, it should be noted that, even if the mesh was refined very locally, the total number of elements grew from about 32 million to 60 million, significantly increasing the computational cost.

High resolution

This surge case was also used to investigate the impact of using a globally more refined mesh. It was not only done to see if unsteady effects could be captured but also to use this simulation as a source of comparison with the one performed on the usual mesh as defined in subsection 4.1.6.

Therefore, the simulation parameters were all kept identical except for the domain and its discretisation. Yet, the same baseline was kept with still $lc = 0.5\ m$ and the YALES2 refinement performed twice. First, the domain length was extended to $z = 10D$ downwind of the rotor. Then, the cell width was lowered in the rotor's refinement region, passing from $lc/12$ to $lc/20$ and resulting in $N_{AL} = 53$. Then the near and far wake refinement regions were extended and slightly refined. The evaluation of the mesh resolution with Pope's criterion in subsection 4.1.6 also highlighted issues in the mesh near the tip and root vortices. Therefore, refinement regions were added in the shape of a long box for the root region and of a hollow cylinder for the tip areas. Similarly to the wake, these regions are cut between the near wake (up to $z = 3D$) and the far one (up to $z = 10D$) with a lower resolution. A cross-sectional view of the mesh is given in Figure 5.6 in which these new refinement regions can be observed. It should be noted that the total number of elements increased from about 32 million to more than 139 million, leading to a substantial rise in computational time.

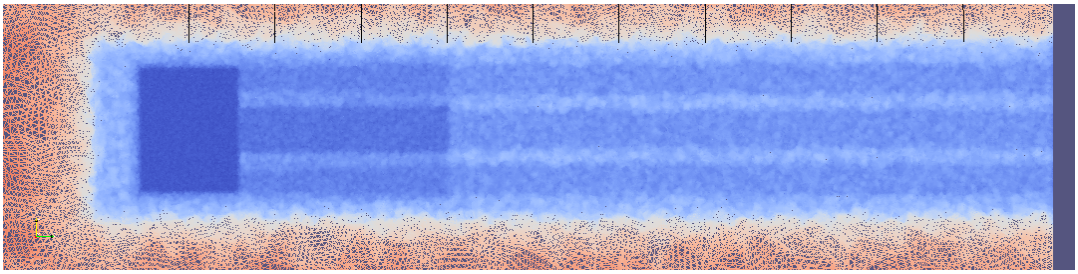

Figure 5.6: Cross section ($x = 0$) view of the refined mesh, coloured by cells size, black line every $z = 1D$

In order to compare and quantify the resolution of this refined mesh, the Pope's criterion was once again used and plotted in the $x = 0$ plane in Figure 5.7. Therefore, more than 90% of the turbulence scale is solved almost everywhere in the field (blue and magenta regions). Only two small regions still show insufficient resolution ($M \geq 0.2$): the tip and particularly the root vortices when leaving the rotor's refinement area. Therefore, the added refinement zones in these regions did not permit to completely solve this issue, and they should be even more refined. Yet, these regions remain very small, and the flow is globally well resolved, even in the far wake.

The rotor loads obtained with this high-resolution mesh are given in the Table 5.5 in comparison with the ones obtained for this surge case on the regular mesh.

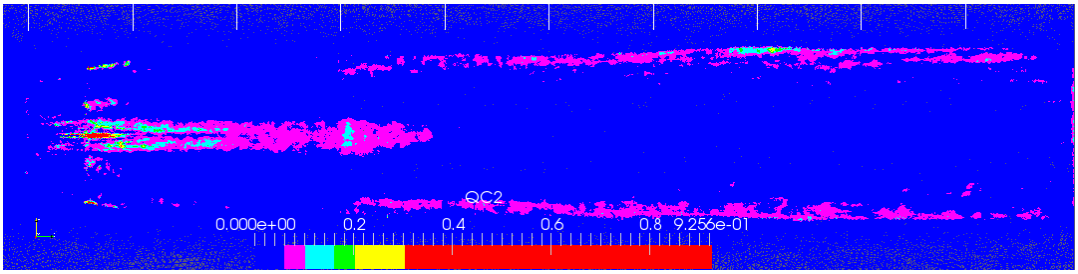

Figure 5.7: Cross section ($x = 0$) view of Pope's criterion with refined mesh for the surge case $\Delta V^* = 0.1$ and $f = 5\ Hz$, white line every $z = 1D$

Mesh	$\overline{T}$ [N]	ΔT [N]	ϕ_T [deg]	$\overline{P}$ [W]	ΔP [W]	ϕ_P [deg]
Usual	9.24	0.96	-92.6	14.09	4.76	-92.6
HR	9.01	0.93	-92.3	13.54	4.70	-91.9

Table 5.5: Power and thrust with the high resolution (HR) mesh in comparison with the usual one, $\Delta V^* = 0.1$ and $f = 5\ Hz$

If there is barely any difference in the phase shift, larger discrepancies appear in the mean loads. Indeed, the mean loads are overestimated on the regular mesh. On the refined one, the amplitude of oscillations is also slightly smaller, but this should be associated with the decrease in mean loads as the ratio between the two remains similar. Anyway, those differences remain minor in comparison with the experimental results. The results are still in accordance with the quasi-steady theory, and no significant unsteady effect has been captured.

In brief, the changes in the mesh did not permit the capture of unsteady effects as experienced experimentally for this high reduced frequency case. Another limitation of the numerical setup, which has not been cited so far, and that could explain such discrepancies with the experimental results, is the absence of flexibility. Indeed, in the simulations, the blades are considered to be rigid, and the motion to be ideally transmitted between the hexapod and the rotor. However, in the experiment, the blades were not perfectly rigid but had a certain flexibility. The same applies to the tower, which is not perfectly stiff and, therefore, does not transmit the motion perfectly to the rotor as imposed by the hexapod. This can become particularly crucial at high frequencies. To the author's knowledge, no estimation of the impact of the tower and blades flexibility in the experiment has been performed.

In order to further investigate the possibility of capturing unsteady effects with the numerical setup, two extreme cases are considered and discussed in section 5.5.

5.3. Local loads

So far, only the loads at the rotor's level have been looked at. However, thanks to the actuator line implementation, one can easily access the loads at blade level as well. In particular, the motions introduce periodic variations of loads that can be critical to determine, for fatigue issues or control strategies.

In order to look at the time evolution of loads at blade level, four positions along the blades are considered. They are represented on the blade's geometry in Figure 5.8.

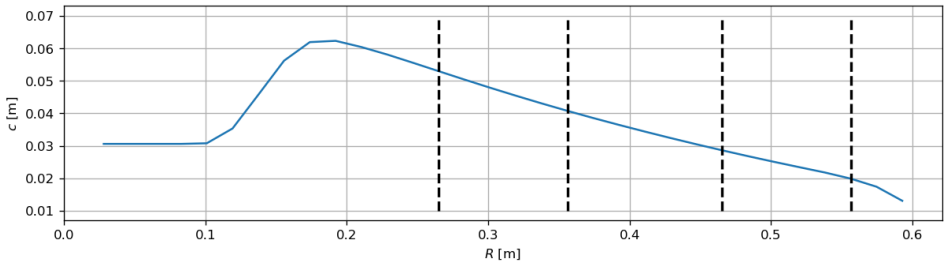

Figure 5.8: Location of the four probes along the blades

At each radial position considered, one can plot the time evolution of the angle of attack and the lift and drag coefficients. Three cases are given in Figure 5.9, Figure 5.10 and Figure 5.11. The first two correspond to the same reduced velocity $\Delta V^* = 0.05$ and the frequency is varied from one low-frequency case ($f = 1\ Hz$) to a high-frequency one ($f = 5\ Hz$). The last one is at the same low frequency ($f = 1\ Hz$) but with a higher reduced velocity $\Delta V^* = 0.1$.

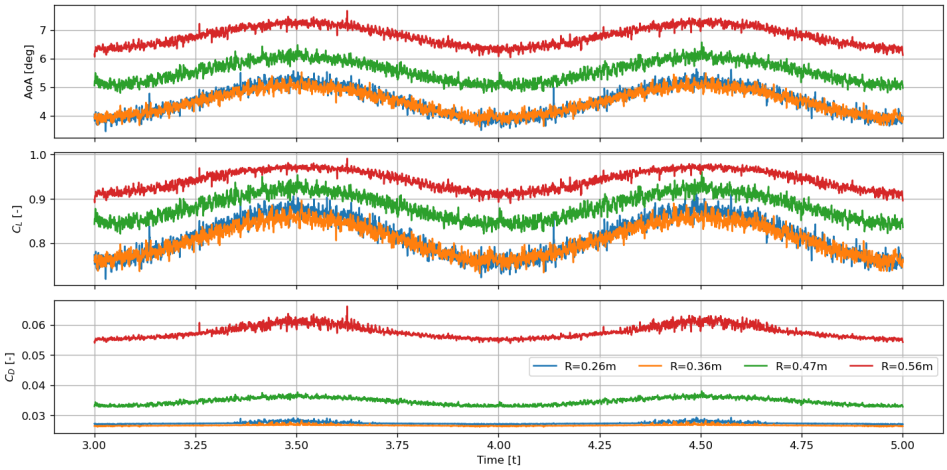

Figure 5.9: Time evolution of the local loads at four radial positions, $\Delta V^* = 0.05$, $f = 1\ Hz$

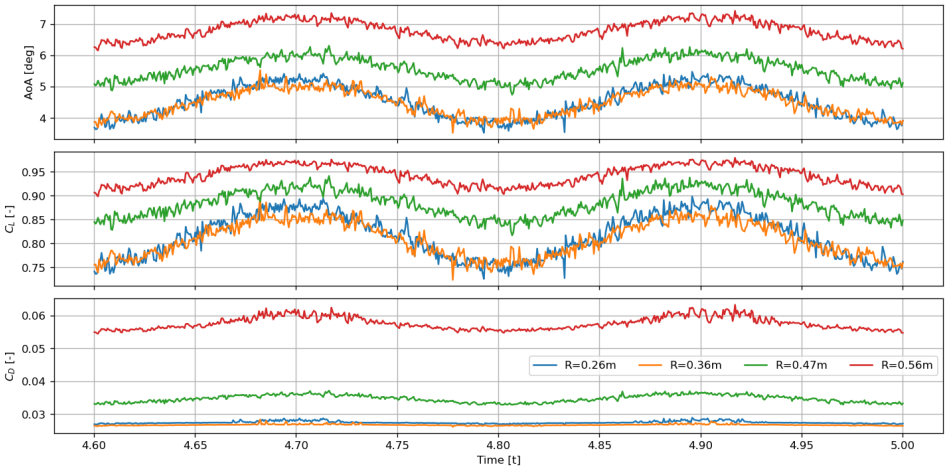

Figure 5.10: Time evolution of the local loads at four radial positions, $\Delta V^* = 0.05$, $f = 5\ Hz$

The reduced velocity and frequency of motion do not have such a significant impact on the local loads, and various comments can be made that apply to all cases.

First, looking at the variations in angles of attack, one observes that, at each radial position, a similar trend is observed, with only an offset, principally attributed to the twist angle. The amplitude of variations is only slightly bigger at inboard parts.

It is also interesting to note that the angle of attack, in these cases, remains outside of static stall regions. In addition, the angle of attack remains in regions where the relation with the lift and drag coefficients is almost linear. Therefore, the coefficients show similar sinusoidal time evolution.

Yet, one can notice a significant difference between the behaviour of the lift and drag loads. If the oscillations are stronger at inboard regions and weaker at outboard regions for C_L, the opposite applies for C_D. Since the lift and the drag are loads in orthogonal directions, this can be important for fatigue loads and structural integrity. Larger amplitudes of variations are experienced in the wind direction at inboard parts, and in the rotor plane at outboard parts. This should be taken with caution because the blades are twisted, but the twist difference between the sections considered is low (see Figure 3.3) and because they are not pitched.

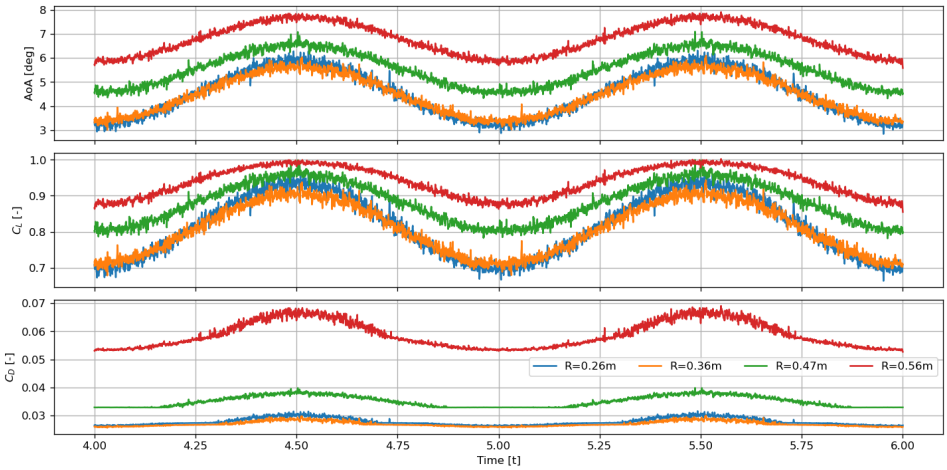

Figure 5.11: Time evolution of the local loads at four radial positions, $\Delta V^* = 0.1$, $f = 1\ Hz$

On the impact of reduced velocity, no big difference can be observed between Figure 5.9 and Figure 5.11. As the reduced velocity increases, so do the amplitudes of the loads oscillations. The differences in amplitude between the outboard and inboard parts also become more important.

Finally, by comparing Figure 5.9 and Figure 5.10, one can estimate the impact of frequency on radial loads. There is barely any difference. This is in accordance with the previous results and the fact that the loads follow the quasi-steady theory. Loads, both at the rotor's and blade's level, are only impacted by the reduced velocity and not the frequency of motion.

Those results can be compared with the work of Chen et al. [26] who also investigated harmonic surge motion. On the rotor loads, they observed similar thrust and power sinusoidal variations. However, when the amplitude of motion was increased, the sinusoidal output was modified, with the upper limit being increased and the lower one decreased. They also plotted the loads at the blade's level (but using a different projection). For surge motion, they obtained a sinusoidal temporal distribution as well.

5.4. Wake behaviour

As mentioned in the literature review, the floating motion will also alter the way the wake behaves. This section aims at looking at the impact of surge on the near and mid wake.

5.4.1. Particular case - $\Delta V^* = 0.05$, $f = 2\ Hz$

First, only one motion case is considered: $\Delta V^* = 0.05$, $f = 2\ Hz$. Because the inflow is uniform and because there is no tower or other source of asymmetry, the wake is mostly axially symmetric. Therefore, looking at the flow in the $x = 0$ plane is sufficient to get most information.

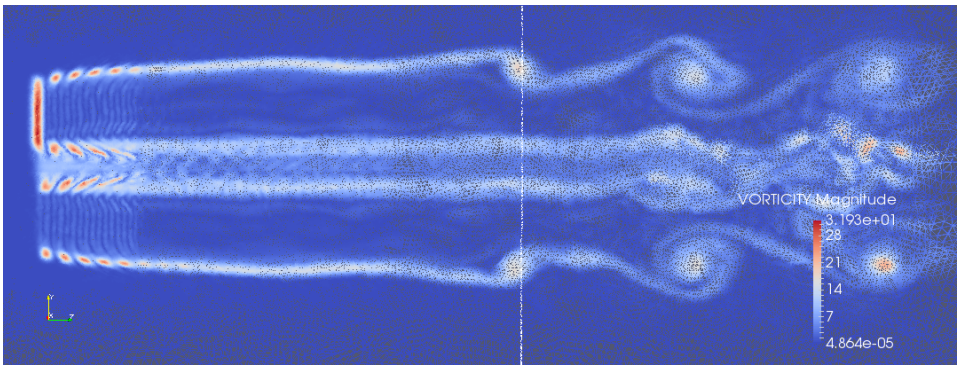

Figure 5.12: Vorticity field in the plane $x = 0$ at $t = 5.0\ s$, motion case $\Delta V^* = 0.05$, $f = 2\ Hz$

The vorticity field in this plane is illustrated Figure 5.12. In the near wake, one can clearly observe

the tip and root vortices, represented by circular areas of high vorticity and shedding from the blades' extremities. As they collapse downwind, regions of high vorticity remain. What differs from static cases wakes is the appearance of vortices later in the wake. Visualising the vorticity field, it seems that these vortices are forming at the surge motion frequency. However, this needs to be checked more thoroughly.

In order to do so, one can use the probe lines, placed at regular intervals in the wake in the plane $x = 0$ at which the velocity is accessible in time. In particular, it is interesting to look at U_y, as the vortices in this plane will create oscillations in the direction of this vertical component of the velocity. Its time evolution is plotted in Figure 5.13a at wake location $z = 3D$ and at the height $y = 0.68\ m$, corresponding to the height of the high vorticity region at this location. Thus, one can clearly observe periodic oscillations with positive and negative values of the same order of magnitude. By using the power spectral density of this signal, plotted Figure 5.13b, one recognise the peak at surge motion frequency $f_s = 2\ Hz$ and its harmonics. Therefore, vortices are shedding in the wake at surge frequency. More details on this phenomenon will be given in subsection 5.4.2.

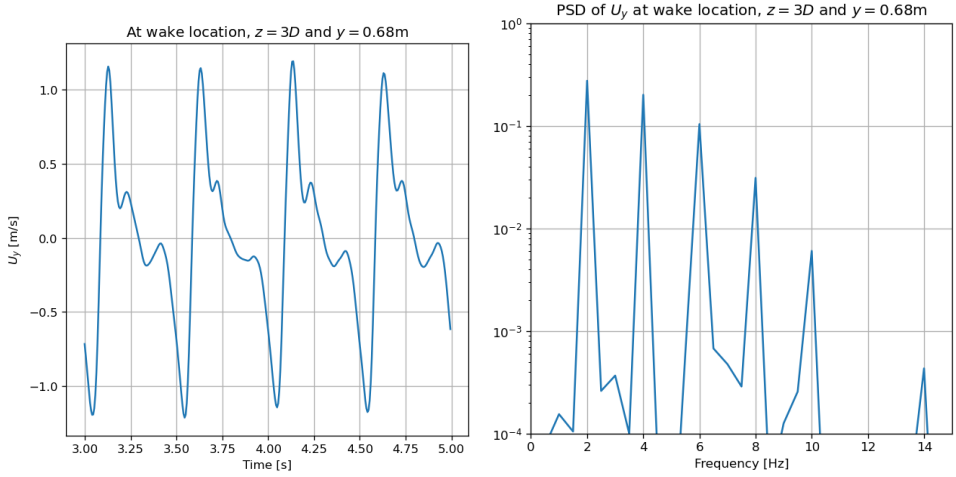

(a) (b)

Figure 5.13: Time evolution of the vertical component of the velocity at the position $(0, 0.68, 3D)$ and its power spectral density, motion case $\Delta V^* = 0.05$, $f = 2\ Hz$

Another important quantity in the wake is the so-called velocity deficit. One can access this information by looking at the distribution of the $z-$component (streamwise) of the velocity along the different probe lines, placed downwind of the rotor. This quantity is plotted Figure 5.14 at four different moments. At all these moments, the rotor is at the same initial position, but, for $t = 5.0$ and $t = 4.5$ the rotor comes from upwind, while it comes from downwind for $t = 4.25$ and $t = 4.75$. Therefore, it can be observed that each duo of the same motion configuration, presents very similar velocity deficits, even at the farthest location downwind of the rotor. The surge motion leaves a clear signature in the wake, even at relatively distant locations. This echos the work of Schliffke [96], who experimentally used a porous disc and made a similar observation for surge motion, when the amplitude or frequency were sufficiently large. If the flow is not solved sufficiently far downwind of the rotor in order to properly comment on the wake recovery, one can still note that the motion alters this process. Indeed, when comparing the different time steps in the latest graph at $z = 6D$, one sees that the velocity deficit is less important when the rotor is coming from its downwind position. Therefore, oscillations in the wind behind the rotor are expected even at far-wake, at least for this motion case.

Finally, one could also look at the wake centre. The method investigated in the work of Coudou et al. [40] is implemented in YALES2 and was used here, based on the velocity deficit. However, the centre was found to barely move during surge motion, and this was true for all motion cases. This can be explained as the surge motion is in the same direction as the freestream velocity and the wake. This is in accordance with the work of Garcia et al. [39], who also find traces of surge motion in the wake by means of a spectral analysis even though the motion would not trigger wake meandering.

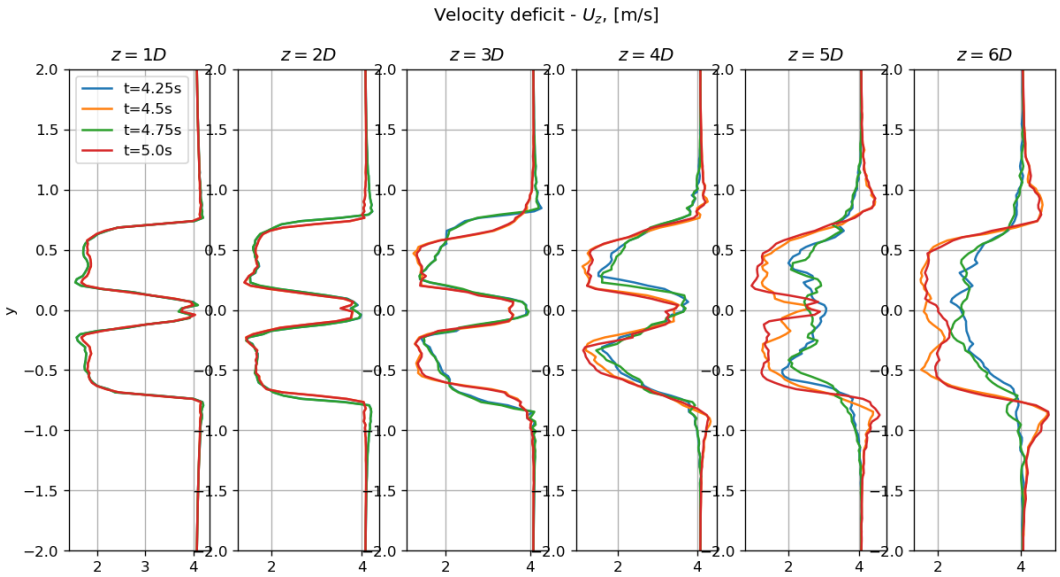

Figure 5.14: Distribution of the instantaneous U_z along probe lines placed at six locations and at four different moment, motion case $\Delta V^* = 0.05$, $f = 2\ Hz$

5.4.2. Vortex rings

In the previous case, particular vortices were formed at surge motion frequencies. This section aims to delve deeper into this phenomenon.

In particular, one can compare the different surge cases with different reduced velocities and frequencies.

The vorticity fields are given in Figure 5.15. For each case, the time step to be plotted was chosen as the snapshot where a vortex was encountered the earliest in the wake. A line was traced at the location of the first appearance of a vortex. This is not an exact measurement of the location at which they are formed because it is difficult to define when a vortex starts, but it permits a comparison between the different motion cases. The locations at which the lines are traced x_L are reminded in Table 5.6.

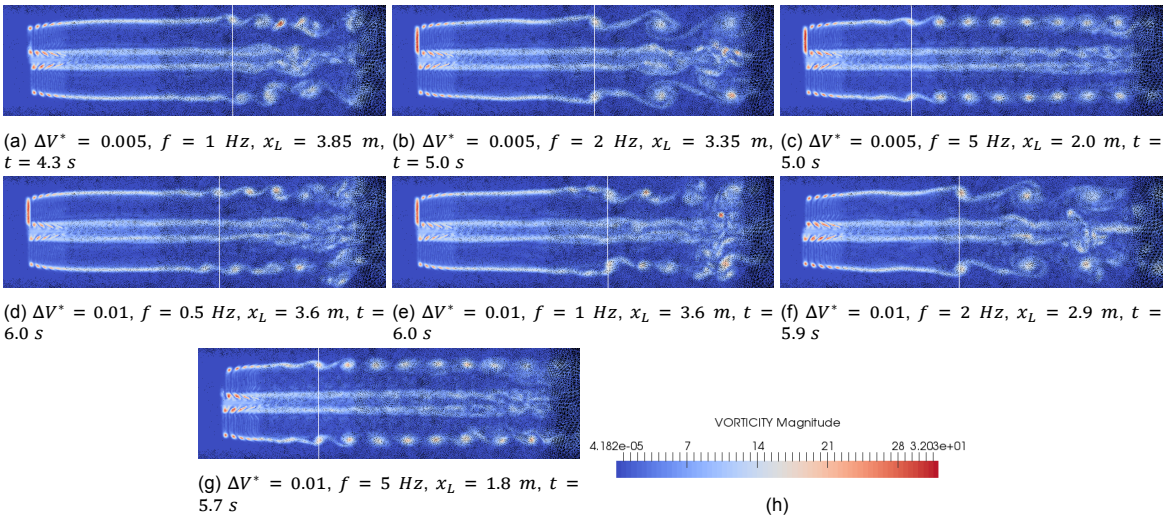

(a) $\Delta V^* = 0.005$, $f = 1\ Hz$, $x_L = 3.85\ m$, $t = 4.3\ s$

(b) $\Delta V^* = 0.005$, $f = 2\ Hz$, $x_L = 3.35\ m$, $t = 5.0\ s$

(c) $\Delta V^* = 0.005$, $f = 5\ Hz$, $x_L = 2.0\ m$, $t = 5.0\ s$

(d) $\Delta V^* = 0.01$, $f = 0.5\ Hz$, $x_L = 3.6\ m$, $t = 6.0\ s$

(e) $\Delta V^* = 0.01$, $f = 1\ Hz$, $x_L = 3.6\ m$, $t = 6.0\ s$

(f) $\Delta V^* = 0.01$, $f = 2\ Hz$, $x_L = 2.9\ m$, $t = 5.9\ s$

(g) $\Delta V^* = 0.01$, $f = 5\ Hz$, $x_L = 1.8\ m$, $t = 5.7\ s$

(h)

Figure 5.15: Vorticity fields in the $x = 0$ plane

In addition, in order to visualise those three-dimensional vortical structures, iso-contours of the Q-criterion are plotted Figure 5.16, coloured by the velocity magnitude. They are plotted for $Q = 20\ s^{-2}$

Case	ΔV^*	f [Hz]	x_L [m]
(a)	0.05	1	3.85
(b)	0.05	2	3.35
(c)	0.05	5	2.0
(d)	0.1	0.5	3.6
(e)	0.1	1	3.6
(f)	0.1	2	2.9
(g)	0.1	5	1.9

Table 5.6: Location of the first appearance of a vortex in the wake for the different motion cases

and at the same time step $t = 5.0\ s$. The Q-criterion is defined as:

$$Q = \frac{1}{2}\left(||\Omega||^2 - ||S||^2\right) \tag{5.3}$$

Wherein Ω is the vorticity tensor and S the rate-of-strain tensor. Therefore, positive Q regions correspond to areas where the rotational component dominates over the stretching component in deformation. It is widely used in CFD as it permits the formation of envelopes around vortical structures. For wind turbine applications, it is often used to visualise the development of tip vortices.

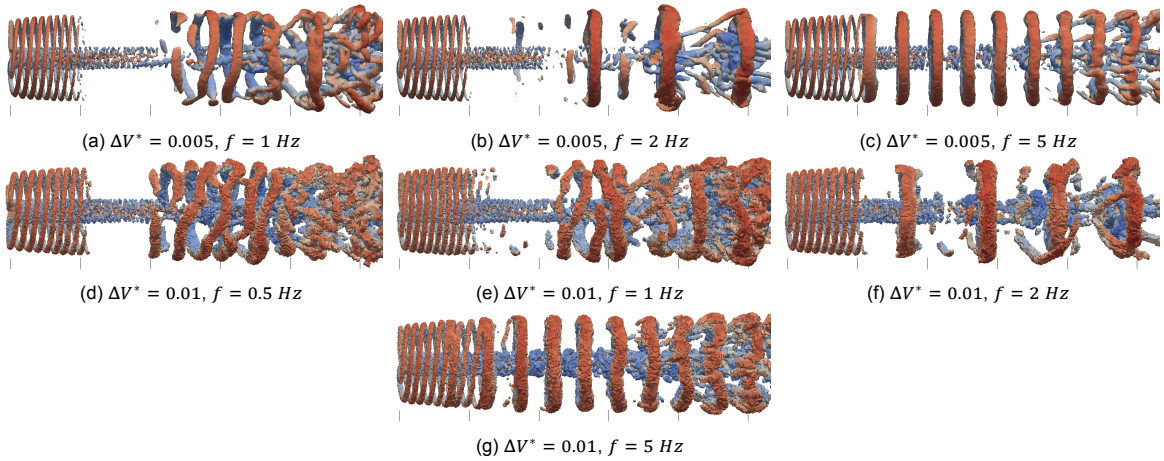

(a) $\Delta V^* = 0.005$, $f = 1\ Hz$ (b) $\Delta V^* = 0.005$, $f = 2\ Hz$ (c) $\Delta V^* = 0.005$, $f = 5\ Hz$

(d) $\Delta V^* = 0.01$, $f = 0.5\ Hz$ (e) $\Delta V^* = 0.01$, $f = 1\ Hz$ (f) $\Delta V^* = 0.01$, $f = 2\ Hz$

(g) $\Delta V^* = 0.01$, $f = 5\ Hz$

Figure 5.16: Iso-contours of Q-criterion= 20 at $t = 5.0\ s$, coloured by velocity magnitude

Therefore, the vortices identified in the vorticity field of the previous case can also be identified in the cases for $f = 2\ Hz$ and $f = 5\ Hz$. From the Q-criterion iso-contours, it appears that those vortices are the footprints on the $x = 0$ plane of three-dimensional vortex rings, enveloping the wake. For both $f = 2\ Hz$ and $f = 5\ Hz$, these vortex rings are formed at surge frequency. On the vorticity fields, it seems that these vortices are bigger for $f = 2\ Hz$. However, the isosurfaces of the Q-criterion, delimiting the vortex rings, have comparable sizes.

From Table 5.6, one can note that the first vortex rings are formed earlier in the wake for $f = 5\ Hz$ than for $f = 2\ Hz$. Looking at the iso-contours, one sees that, in the former case, they are directly formed from tip vortices, while in the latter case, they form later after the tip vortices dissipate. The impact of the reduced velocity on the formation of those vortices is more subtle. Yet, it results in them being formed slightly earlier as the reduced velocity increases.

For the lowest frequencies, $f = 0.5\ Hz$ and $f = 1\ Hz$, vortex rings cannot be clearly identified. Vortical structures are formed later in the wake but do not form rings, and the flow is more chaotic. In addition, the vortices are not formed at the corresponding surge frequencies.

In their work, Duan et al. [42] also observe the formation of similar vortex rings during surge motion. Similarly, they noted a significant impact of the frequency of motion, but only a subtle one for the amplitude (hence the reduced velocity). Nevertheless, they made an apparent opposite observation, noticing a formation of clear ring vortices at low frequencies but not at high frequencies. However, their work has considered the motion of reduced frequencies $f_r = 0.56, 1.11$ and 2.23, while this present

work has considered the motion of reduced frequencies $f_r = 0.15, 0.3, 0.6$ and 1.5. Therefore, the conclusions are not contradictory, but it seems like vortex rings are only formed within a certain range of surge frequencies. Yet, it should be mentioned that their work was performed on a bigger rotor, at a lower wind speed, and the motions investigated mostly correspond to higher reduced velocities (between 0.03 and 0.83). They also observed the vortex rings to form earlier in the wake.

In their work, they also stated that the break-down of these vortex rings was initiated by the expansion of the central vortices, interacting with the outer structures. Such a phenomenon seems to occur in the Figure 5.16 as the expansion of the central vortices can be observed in the far wake. However, the vortex rings also seem to be deformed, probably due to differences in velocities all around the ring. In addition, the flow in the far wake should be looked at with caution, as the mesh resolution is quite low in this area.

The comments made on the wake development should be compared and qualified with respect to the surge case ($\Delta V_S^* = 0.1$, $f_s = 5\ Hz$) investigated with the high resolution mesh (see Table 5.2.4). In particular, for this surge case, the finer mesh permits checking whether vortex rings are still observed with a higher resolution.

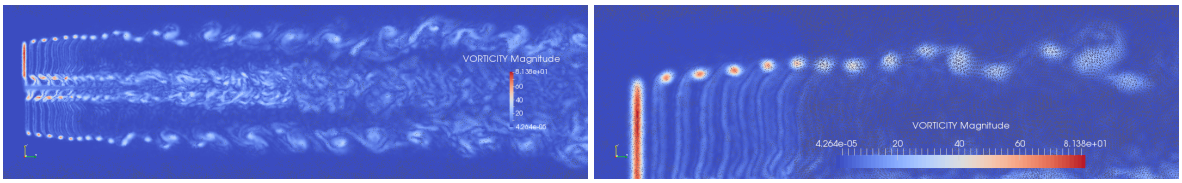

(a) (b)

Figure 5.17: Vorticity field in the $x = 0$ plane for the surge case with high resolution mesh, zoomed on the tip vortices in (b)

The vorticity field is given in Figure 5.17 with a zoom on the upper part of the near wake, where tip vortices are formed. In addition, iso-contours of the Q-criterion (=50) are plotted in Figure 5.18.

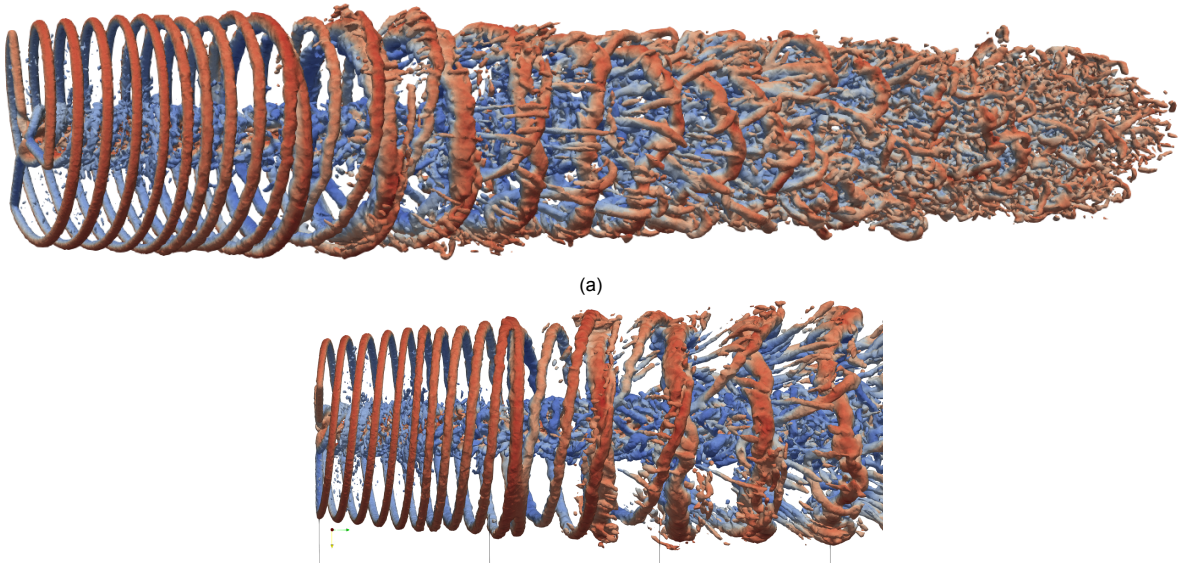

(a)

(b)

Figure 5.18: Iso-contours of Q-criterion= 50 coloured by velocity magnitude, zoom on the near wake in (b) with black lines every $z = 1D$

First, looking at the vorticity field, it appears that vortices are still formed at regular intervals in the wake. However, their resolution is increased here, and their geometry is better described. They are not represented as simple circular areas of high vorticity in the plane anymore. In addition to the wake being extended, one can notice a slight vertical meandering in the wake delimited by the lines of vortices. Looking more closely at the near wake, the slight undulation of the tip vortices before the formation of the first large vortex is retrieved. However, the tip vortices are better described and dissipate later than

in the regular mesh. This permits one to notice a variation in the distance between two consecutive tip vortices, a consequence of the surge motion combined with the circulation of the vortices.

Observing the iso-contours now, what strikes first is the higher number of three-dimensional vortical structures represented, even though the Q-criterion was increased (Q-criterion$= 50$). In the near wake, the tip vortices are clearly visible. The root vortices, on the other hand, are mixing very early in the near wake. Similarly to the results on the regular mesh, one can observe tip vortices colliding and changing trajectories after $z = 1D$. Around $z = 1.7D$, a first vortex ring is formed. Due to the increased number of vortical structures represented, it is less visible, but it is still possible to identify a closed ring. Then, other rings can be identified, but they more rapidly dissipate as they mix with the rest of the tip vortices and with the root vortices that have now evolved in a growing central region of high turbulence. As the development of the wake continues, the vortex rings break, and more and more streamwise vortical structures are formed.

In brief, using a higher resolution still permits identification of vortex rings in this surge case. However, a better description leads to the early dissipation of these structures as they interact with more other vortices.

Finally, the previous findings also echo the work of Schliffke [96]. Using a porous disc under imposed surge motion, he found that the surge motion leaves a clear signature in the wake when the amplitude or frequency is sufficiently large. Here, the previous results suggest that this statement holds for the frequency, but the amplitude has a less significant impact. For low frequencies, not only are vortex rings not formed, but the spectral analysis of the flow in the wake does not permit a clear identification of the surge motion frequency.

5.5. Extreme cases

As explained earlier, a possible explanation for the discrepancies at high frequencies between the numerical and experimental results, in which QST no longer holds, is the low amplitude of motion compared to the mesh thickness. In order to further investigate this hypothesis, two new cases are considered with the same high frequency $f_s = 5\ Hz$, but with higher amplitudes. This results in very high reduced velocities ($\Delta V_s^* = 0.75$ and $\Delta V_s^* = 1$), which is why they are called extreme cases. In addition, for each reduced velocity, an additional case was considered at a lower frequency in order to compare and see if the results were still in accordance with the quasi-steady theory. The frequency of these additional cases was chosen as the minimum frequency for which the rotor remains in the rotor's refinement region during the motion (high amplitudes are achieved).

5.5.1. Loads

Again, the temporal evolution of thrust and power was obtained and plotted, respectively for $\Delta V_s^* = 0.75$ and $\Delta V_s^* = 1$, in Figure 5.19 and Figure 5.20.

First, both load quantities do not follow a nice sinusoidal temporal distribution as in the previous cases, but they are still periodic at motion frequency. For $\Delta V_s^* = 0.75$ (Figure 5.19), the loads first increased as the rotor was moving downwind, similarly to the previous results. Then, the loads are expected to keep growing until the rotor comes back to its initial position, but they reach a maximum and decrease until this position. Then, they increase again before catching up with the previous results and decreasing before the rotor reaches its most upwind position. Then, it is similar to the previous results as the loads decrease until the rotor comes back to its initial position and the cycle starts again. The power experienced a larger decrease between the two peaks than the thrust. For the larger reduced velocity $\Delta V_s^* = 1$ (Figure 5.20), similar trends are experienced except that the loads increase and decrease again between the two peaks.

In order to continue discussing on the loads evolution, more details are given in Table 5.7. The amplitude of variation Δ is calculated as the half of the difference between the maximum and the minimum encountered during one period of motion. The minimal value is also given in the table, as the extremes are not centred around the average anymore.

Therefore, negative power values are reached in all cases, and negative thrust values are reached in the two cases with the highest reduced frequency. This will later be commented on in the next subsection.

On the mean values now, a significant decrease is observed for both power and thrust in all cases compared to the static values. This decrease is accentuated with the higher reduced velocity, par-

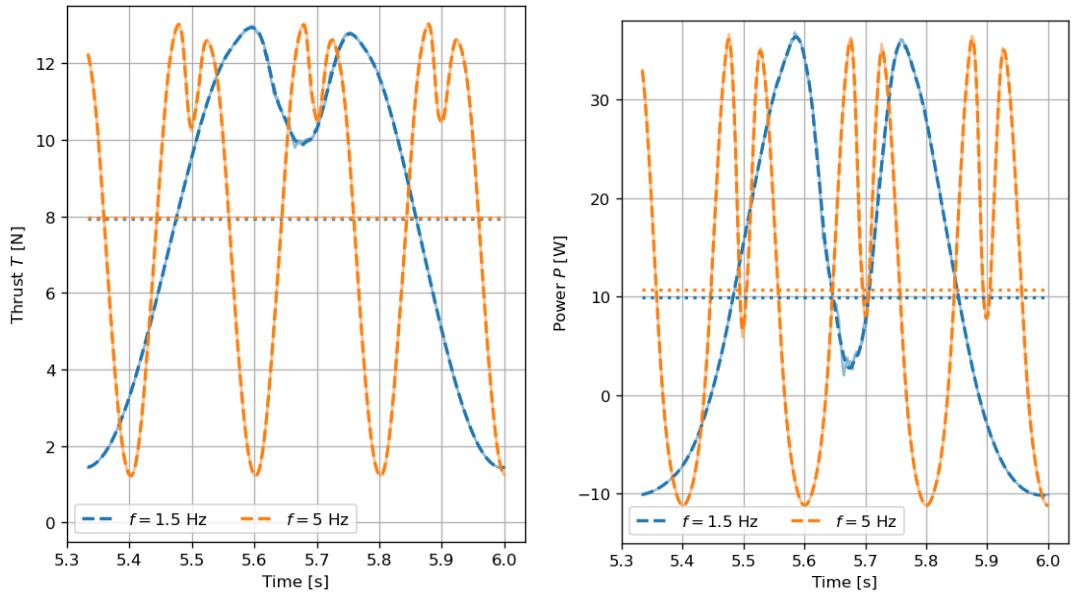

(a) Thrust (b) Power

Figure 5.19: Thrust and power for surge case of different frequencies but same reduced velocity $\Delta V_s^* = 0.75$, including the filtered ('–') and the averaged solutions over one motion period ('..')

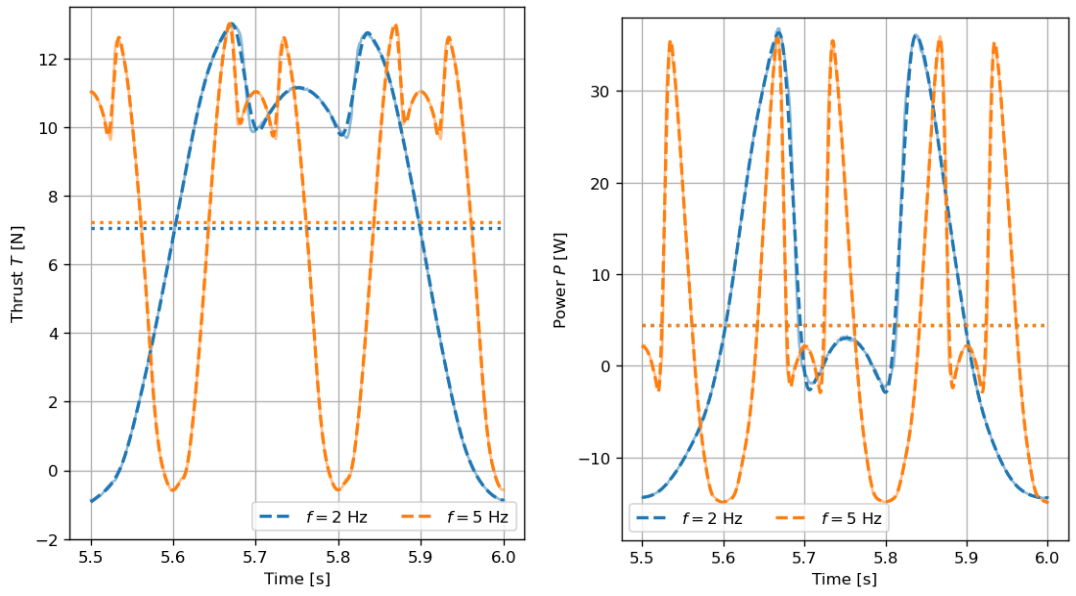

(a) Thrust (b) Power

Figure 5.20: Thrust and power for surge case of different frequencies but same reduced velocity $\Delta V_s^* = 1$, including the filtered ('–') and the averaged solutions over one motion period ('..')

ticularly for the power. This decrease in mean loads is also accentuated at low frequencies but the differences remain small.

Then, as expected, the amplitudes of variation increase with the reduced velocity. For $\Delta V_s^* = 0.75$, the amplitude grows with the frequency, and the opposite is observed for $\Delta V_s^* = 1$. Yet, the impact of the frequency remains slight again.

Finally, the phase shift keeps oscillating around the theoretical $\phi = -90°$ value.

In brief, the results show little difference between each pair of cases with identical reduced velocities. The facts that the impact of the frequency is only slight and the phase shift stays close to its theoretical

value suggest that the quasi-steady theory still holds. Yet, both the thrust and the power follow a peculiar temporal evolution, which can be explained by looking at the loads on the blade's scale.

ΔV_s^*	f_s [Hz]	$\overline{T}$ [N]	ΔT [N]	$\min T$ [N]	ϕ_T [deg]	$\overline{P}$ [W]	ΔP [W]	ϕ_P [deg]	$\min P$ [W]
0.75	1.5	7.93	5.75	-93.0	1.43	9.93	23.24	-90.9	-10.15
0.75	5	8.14	5.89	-88.8	1.22	11.28	23.75	-90.9	-11.22
1	2	7.07	6.95	-89.9	-0.93	4.42	25.37	-85.5	-14.39
1	5	7.20	6.79	-86.8	-0.57	4.5	25.31	-84.5	-14.87

Table 5.7: Comparison of rotor loads for extreme surge cases

Thus, the temporal distribution of the angle of attack and the lift and drag coefficients at four radial locations are plotted in Figure 5.21 and Figure 5.22. They are plotted respectively for $\Delta V_s^* = 0.75$ and $\Delta V_s^* = 1$, both at $f_s = 5\ Hz$. Only the high-frequency cases were plotted since, once again, very few discrepancies were found with the low-frequency ones.

Therefore, one can see that the unexpected decrease in the loads is caused by the angle of attack that exceeds the static stall limit (around $\alpha = 11°$). As the airfoils experience stall, the lift drops and the drag increases significantly, causing the particular load evolution observed before at the rotor's scale. This is particularly important in the inner sections.

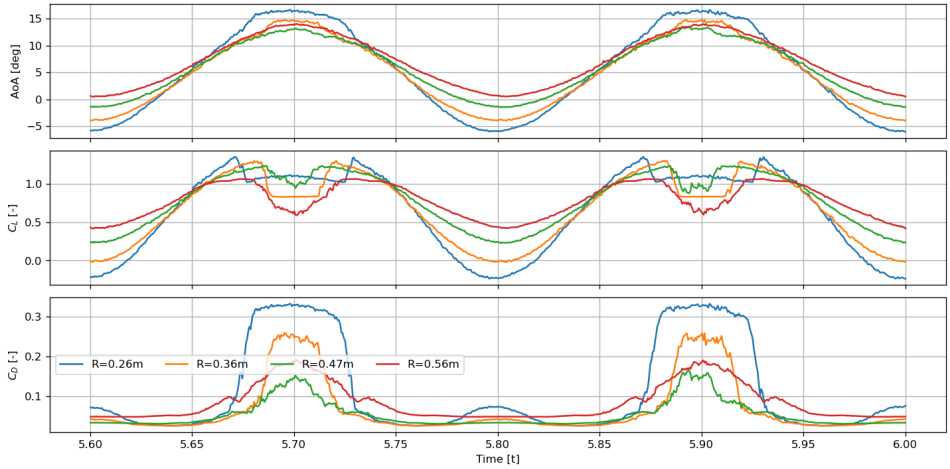

Figure 5.21: Temporal evolution of the angle of attack and the corresponding loads at four radial positions, extreme surge case $\Delta V_s^* = 0.75$, $f_s = 5\ Hz$

5.5.2. Rotor working states

As quickly mentioned before, negative values of power are experienced in these four surge cases, and negative values of thrust are experienced as well when $\Delta V_s^* = 1$. This suggests that changes in rotor working states may occur during those extreme surge cases.

In addition, by looking at the wake, the rotor seems to interact with its tip vortices during motion, which could trigger the vortex ring or turbulent states. Iso-contours of the Q-criterion are plotted for one case ($\Delta V_s^* = 1$, $f_s = 2\ Hz$) in Figure 5.23 in order to visualise the three-dimensional vortical structures. They are plotted for five time steps during one motion period, explaining that the first and last ones are very similar. The rotor's initial position is marked with the black line. In the first and last snapshots, the rotor, as it is moving downwind at its highest velocity, seems to encounter and interact with its tip vortices, forming a large vortex ring that later progresses in the wake.

In the literature, the interaction of the rotor with its own tip vortices is frequently connected with the possibility for the rotor to work in a vortex ring state. The occurrence of this state can easily be checked, as it is associated with flow reversal on part of the blades. The streamwise component of the velocity at the rotor is plotted in Figure 5.24 for five time steps during one surge period.

Therefore, flow reversal is never encountered as the streamwise component of the velocity always remains positive. In addition, the smallest values of U_z were expected at $t = 5.5\ s$ and $t = 5.99\ s$, when

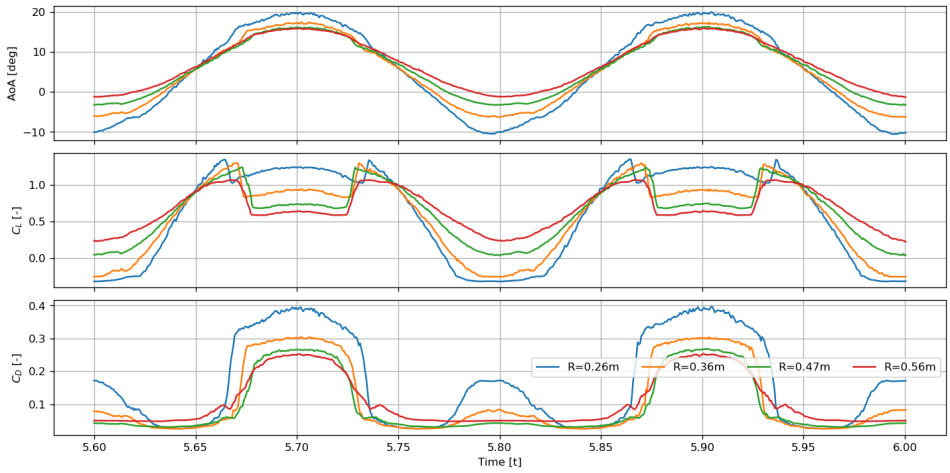

Figure 5.22: Temporal evolution of the angle of attack and the corresponding loads at four radial positions, extreme surge case $\Delta V_s^* = 1$, $f_s = 5\ Hz$

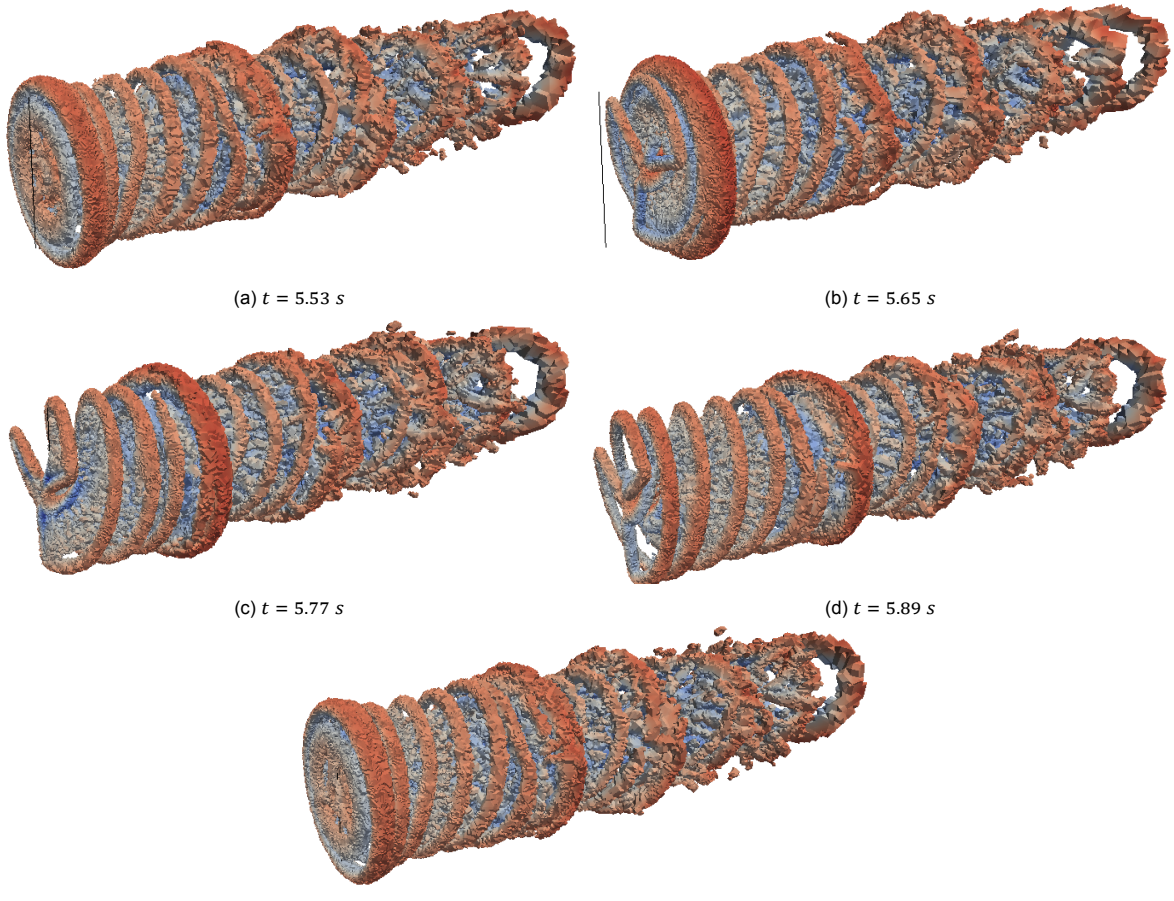

(a) $t = 5.53\ s$ (b) $t = 5.65\ s$

(c) $t = 5.77\ s$ (d) $t = 5.89\ s$

(e) $t = 6.00\ s$

Figure 5.23: Time evolution of iso-contours of Q-criterion= 50, extreme case $\Delta V_s^* = 1$, $f_s = 2\ Hz$

the rotor moves upwind at its highest velocity. Actually, the velocity at the rotor is even almost uniform at those time steps. Anyway, the wind keeps passing the rotor in the same direction, indicating that the vortex ring state is not encountered during this motion.

In comparison, Dong and Viré [55] investigated surge motion of similar reduced velocity ($\Delta V_s^* = 1.04$) but higher reduced frequency ($f_r = 2.2$) and clearly observed flow reversal at the rotor.

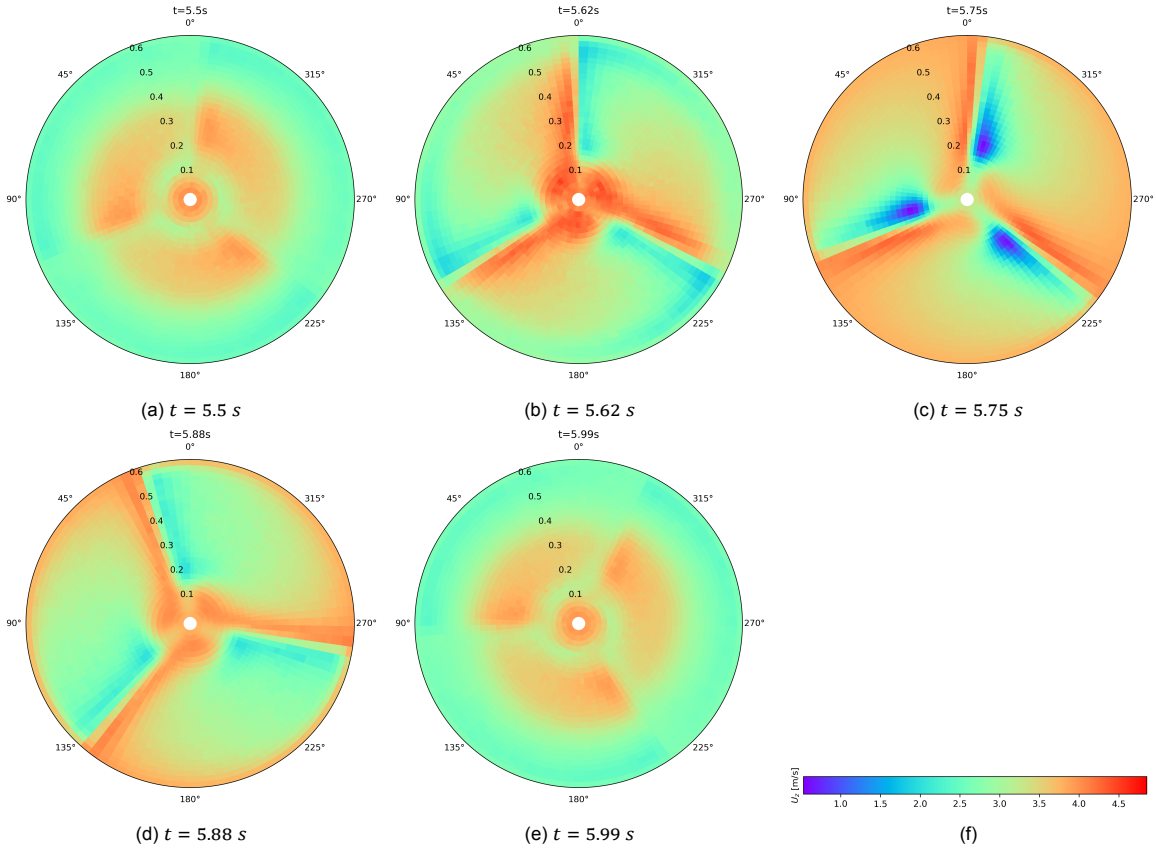

(a) $t = 5.5\ s$ (b) $t = 5.62\ s$ (c) $t = 5.75\ s$

(d) $t = 5.88\ s$ (e) $t = 5.99\ s$ (f)

Figure 5.24: Time evolution of U_z at the rotor, extreme case $\Delta V_s^* = 1$, $f_s = 2\ Hz$

Coming back to load variations, Kyle and Früh [58] investigated the changes in rotor states during surge motion with similar reduced velocities ($0.68 \leq \Delta V_s^* \leq 1.55$). They used the sign of the thrust and power coefficients. They identified changes from windmill and turbulent working states ($T > 0$, $P > 0$), to a so-called braking state ($T > 0$, $P < 0$), to a propeller mode ($T < 0$, $P < 0$), and finally to the vortex ring state ($T < 0$, $P > 0$). The last one, however, was only encountered at the lowest freestream velocity. The third one was also only very slightly encountered at the highest freestream velocity. Here, the same process is observed with changes between phases 1 and 2 experienced at $\Delta V_s^* = 0.75$, and between phases 1, 2 and 3 at $\Delta V_s^* = 1$. This suggests that, in both configurations, the rotor enters the so-called braking state and that, for the highest reduced velocity, the propeller working state is encountered.

However, during the propeller working state, the flow is expected to contract at the rotor and not expand as in the windmill state (see Figure 2.5). This should happen at $t = 6\ s$ for the case $\Delta V_s^* = 1$, $f_s = 2\ Hz$ as both the power and the thrust are at their minimal negative values. The streamlines in the plane $x = 0$ at this time step and for this case are represented Figure 5.25. Therefore, the flow still expands at the rotor, indicating that the rotor remains in windmill working state, even though power is added to the flow and a forward thrust is created.

Therefore, the rotor appears to work in propeller mode while the streamtube as a whole is actually still in windmill mode. Those results are in line with the discussion made in subsection 2.2.4. Indeed, the studies made in the literature, such as the work of Kyle and Früh [58], Dong and Viré [55] or Ferreira et al. [56], highlighted the difference between the classic definition of the working states for the streamtube and the local behaviour of the rotor. From the design point of view, the most important insight is that negative values of both thrust and power can be achieved under those motion configurations.

In conclusion, the impact of the frequency on the loads of these extreme surge cases was not found to be as significant as experienced in the experiment for lower reduced velocities. This suggests that the significant discrepancies compared to the experiment are not due to the low ratio between the amplitude of motion and cell width near the rotor. However, these extreme cases were simulated with

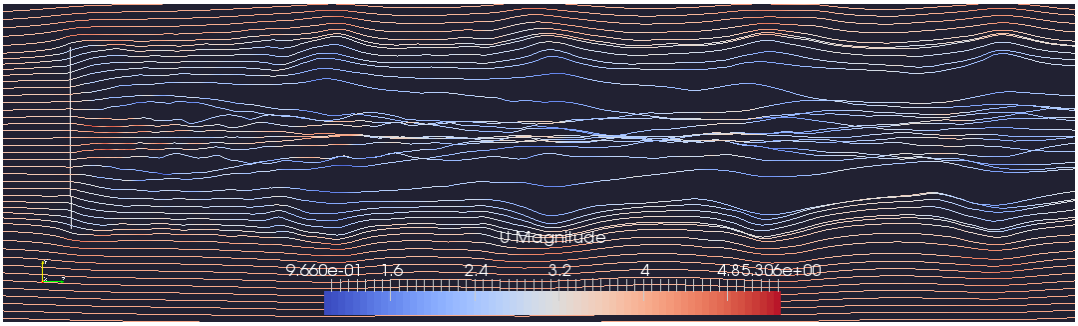

Figure 5.25: Velocity streamlines in the $x = 0$ plane at $t = 6\ s$, motion case $\Delta V^* = 0.05$, $f = 2\ Hz$

important limitations in the numerical model. First, stall was encountered, and the blades experienced high variations in angle of attack. Therefore, dynamic stall might play a significant role in these cases, but it was not taken into account in the simulations. Then, the polars are highly Reynolds-dependent and YALES2 cannot deal with such polars. During motions with such variations in apparent velocity, this constitutes a strong limitation. This issue can also be a cause to explain the discrepancies with the experimental results at high frequency for the lower reduced velocity cases. In addition, the difference might not come from the aerodynamic model but rather from the structure of the tower and the blades, which experiences vibrations at these high frequencies.

Finally, a discussion on the rotor working states was made for these extreme cases. It should be considered carefully in light of the limitations of the numerical model just described.

6

1 DOF - Pitch imposed motion

In this chapter, one-degree-of-freedom harmonic pitch motions are now imposed.

6.1. Cases description

Here, the goal is not to perform a complete and thorough study of the turbine's response to imposed pitch motion, but rather to evaluate the case that will later be considered in 2 DOF motions.

Thus, only one reduced velocity was retained. In Delft's experimental campaign, different reduced velocities than fro surging were used. The closest one was retained: $\Delta V_p^* = 0.072$. The distance between the rotor centre and the hexapod centre, from which the displacements are imposed, is $1.16\ m$.

In addition, two frequencies were chosen: a low-frequency case $f_p = 1\ Hz$, and a high-frequency case $f_p = 5\ Hz$.

The pitch velocity at the rotor's centre is prescribed as follows:

$$V_{p,p} = A_p \left(2\pi f_p\right) \cos\left(2\pi f_p t\right) = \frac{\Delta V_p^* U_\infty}{H_t} \cos\left(2\pi f_p t\right) \tag{6.1}$$

The cases' information is gathered in the Table 6.1, in which the amplitude is also given (computed from the reduced velocity and frequency).

Case	ΔV_p^* [-]	f_p [Hz]	A_p [deg]
P005f1	0.072	1	2.25
P005f5	0.072	5	0.45

Table 6.1: Reduced velocity and frequency of the harmonic pitch motion cases investigated

6.2. Rotor loads - Thrust and Power

Again, the time evolution of the rotor loads, i.e. the thrust and the power, are looked at and plotted Figure 6.1. The average values, the amplitude of variations, and the phase shift with the pitch displacement are also given in Table 6.2. The comparison with the experimental results, when available, is also given.

Source	Frequency [Hz]	$\overline{T}$ [N]	ΔT [N]	ϕ_T [deg]	$\overline{P}$ [W]	ΔP [W]	ϕ_P [deg]
YALES2	$f = 1$ Hz	9.23	0.68	-91.8	14.04	3.42	-91.5
	$f = 5$ Hz	9.24	0.69	-92.5	14.08	3.42	-92.3
Exp.	$f = 1$ Hz	9.77	0.80	-94.4	10.14	3.39	-100.0
	$f = 5$ Hz	9.87	1.46	-76.6	10.65	/	/

Table 6.2: Comparison of rotor loads for pitch motion with $\Delta V_p^* = 0.072$

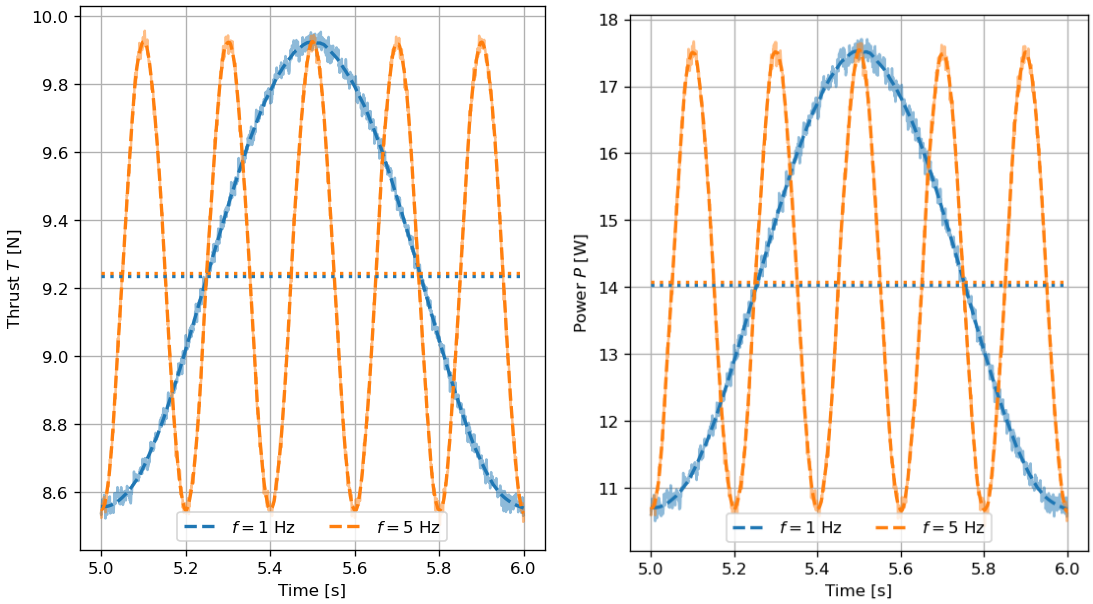

(a) Thrust

(b) Power

Figure 6.1: Thrust and power for pitch motions with $\Delta V_p^* = 0.072$, including the filtered ('–') and the averaged solutions over one motion period ('..')

Most of the comments made for surge motion also apply here for pitch. First, the numerical results show a slight decrease in mean thrust and mean power compared to static values. This decrease is slightly more important at low frequencies. On the other hand, the phase shift shows a little increase with motion frequency. More importantly, the results are again in quasi-steady theory, as the amplitudes of variations are similar for both frequencies. Again, this differs from the experimental results, in which the load variations significantly increased at high frequencies. Finally, if the numerical thrust (both average and variation amplitude) is again underestimated compared to the experimental one, the differences in power are, now, very slight.

Globally, the rotor shows a similar response in terms of loads for pitching than for surging.

6.3. Local loads

The angle of attack as well as the lift and drag coefficients are plotted at four radial positions in Figure 6.2 and Figure 6.3 respectively for $f = 1\ Hz$ and $f = 5\ Hz$. The four radial positions are the exact same as before (see Figure 5.8).

This time, a major difference appears between pitching and surging. Indeed, the load variations at the local level are not as nicely sinusoidal as before, but there are variations that are not occurring at motion frequency. During surging, a blade experiences the same difference in apparent freestream velocity as the rotor centre. Even if the blades are rotating, the plane of rotation always remains orthogonal to the freestream velocity and surge velocity. On the other hand, when the rotor is pitching, the plane of rotation is no longer orthogonal, and the blades no longer experience the same difference in velocity as the rotor centre. These additional variations happen on one blade, but they are compensated for when looking at the three blades. That is why these variations do not appear when looking at the rotor loads (thrust and power in the previous section).

In the work of Chen et al. [26], they also looked at the evolution of the loads at different span locations for both harmonic 1DOF pitch motion. If they also obtained sinusoidal variations for surge, the pitch response at blade's level was found to be more imperfect as well. Similarly to this study, they notably observed outputs with more triangular trends.

Other than that, the same comments can be made as for surge motion. As the angle of attack remains below stall, the lift coefficient remains in the quasi-linear region and shows a very similar trend to the AoA. Additionally, the variations in lift are stronger near the root. On the other hand, the variations in drag are more important in the region closer to the tip.

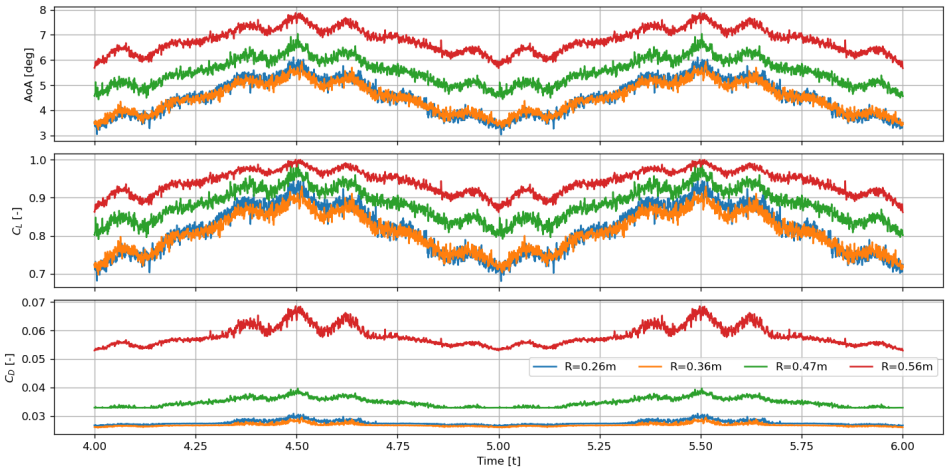

Figure 6.2: Time evolution of the local loads at four radial positions, $\Delta V_p^* = 0.072$, $f = 1\ Hz$

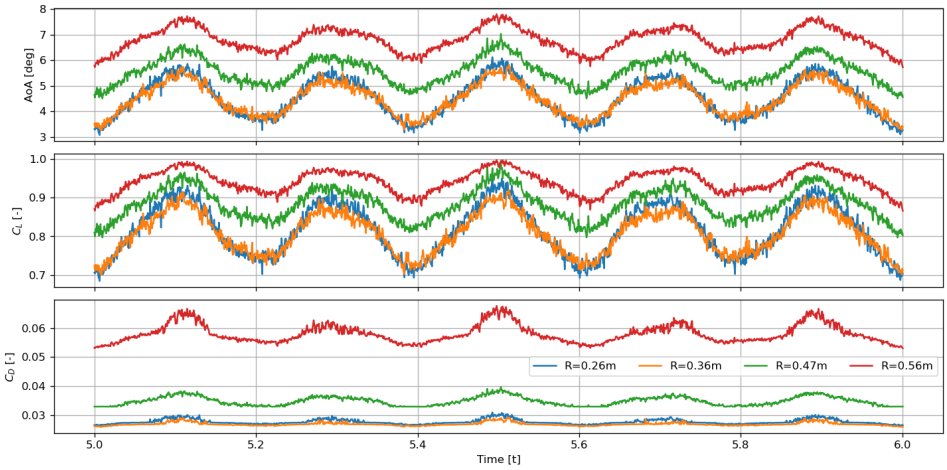

Figure 6.3: Time evolution of the local loads at four radial positions, $\Delta V_p^* = 0.072$, $f = 5\ Hz$

6.4. Wake behaviour

The two cases, with distinct frequencies, show very different wake development. Snapshots of the vorticity field in the $x = 0$ plane are provided in Figure 6.4. In order to visualise three-dimensional vortical structures, iso-contours of the Q-criterion are plotted as well in Figure 6.5.

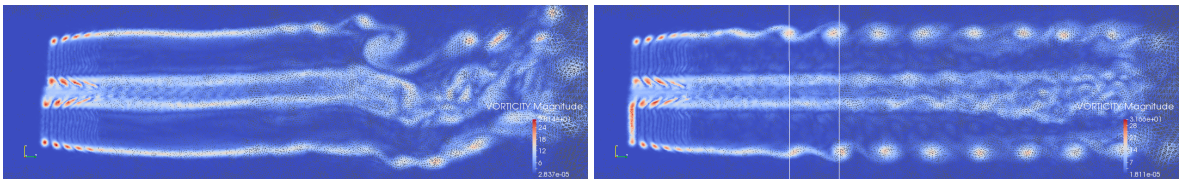

(a) $f = 1\ Hz$, $t = 5.3\ s$ (b) $f = 5\ Hz$, $t = 6.0\ s$

Figure 6.4: Vorticity fields in the $x = 0$ plane, pitch cases

For the high-frequency case, a similar phenomenon to the surge is experienced, with the development of vortex rings. However, from Figure 6.4b, it appears that the vortices are formed earlier in the upper part of the wake. The first line is traced at $z = 1.9\ m$ and the vortex at the upper part is formed, but the one at the lower part is just forming. This can be explained as the upper region experiences a motion of larger amplitude and larger motion velocity during pitch motion. It is also interesting to note that the first vortex is formed about the same distance from the rotor's initial position as the surge at

this frequency ($f = 5\ Hz$). For this high-frequency case, one can also observe in Figure 6.5b that the distance between two successive tip vortices varies in the near wake. This can even cause two vortices to collide. Such a phenomenon was also observed by Fang et al. [32] for pitch motion. However, in this case, it remains relatively small due to the amplitude and frequency considered.

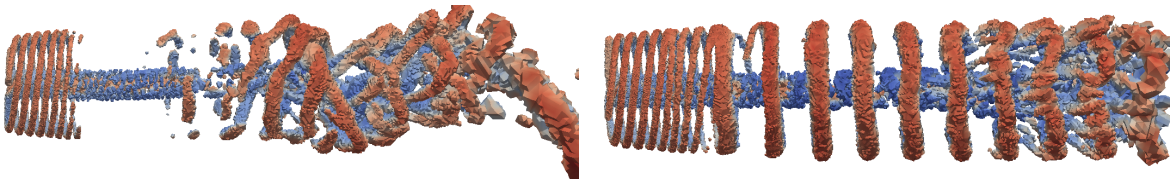

(a) $f = 1\ Hz$, $t = 5.3\ s$ (b) $f = 5\ Hz$, $t = 6.0\ s$

Figure 6.5: Iso-contours of Q-criterion = 20 coloured by velocity magnitude, pitch cases

In the low-frequency case, no vortex ring can be observed. The flow, past the near wake, shows more chaotic behaviour. Yet, one particular phenomenon can be observed with the formation of a strong vortex in the upper part of the wake, at each period of motion. This vortex has the peculiarity of causing vertical meandering of the wake. Indeed, by looking at Figure 6.4a or Figure 6.5a, one can clearly see the wake deflecting downward right after the vortex, and then upward. This meandering in the vertical direction can be observed more in detail by looking at the temporal evolution of the wake centre's height y_C plotted in Figure 6.6 (the vertical meandering of the high frequency case, as well as the horizontal one for both cases are not shown because they are not significant). Therefore, one can see the deflection downward of the wake caused by the vortex, which moves downwind before a new vortex is formed one period of motion later. As a reaction to the deflection downward of the wake, the wake centre seems to oscillate later downwind. This finding echos the work of Johlas et al. [21], [22] who also observed vertical meandering during pitching. However, this is observed here only for the low-frequency case, which has a larger amplitude than the high-frequency one.

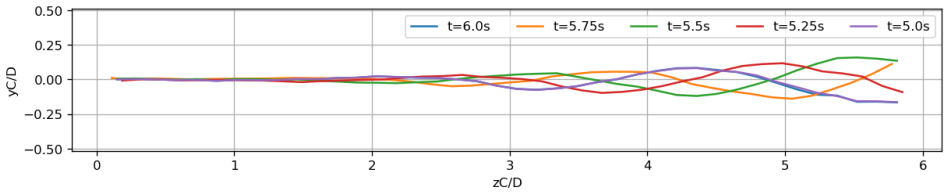

Figure 6.6: Dimensionless wake centre height at 5 five time steps during pitch motion, $\Delta V_p^* = 0.072$, $f_p = 1\ Hz$

Finally, one can identify differences between the low and high frequency cases in the velocity deficit as well. The average $z-$ component of the velocity is plotted on several probe lines along the wake in Figure 6.7. The mean values are obtained by averaging over the complete simulation, even though the wake has not converged at $t = 0\ s$. Yet, the simulation was found to be sufficiently long for this issue not to introduce any significant errors. Then, if the velocity deficit is very similar in the near wake, it starts to differentiate later downwind. In particular, the velocity gradient caused by the root vortices that create a region of high velocity, is reduced earlier at low frequencies. It seems that the chaotic flow and the strong vortex causing deflection of the wake at low frequency accelerate the recovery of the wake compared to the high frequency situation. In the last probe line at far wake, the velocity gradient is much lower for $f = 1\ Hz$ but the region where the velocity is reduced compared to the freestream velocity is extended.

Schliffke [96], who also investigated one degree-of-freedom pitch motion with his porous disc, could not find a clear signature of pitch motion in the wake. Here, whether it is the vortex rings or the strong vortex causing periodic deflection, both forming at pitch motion frequency, the footprint of the motion on the wake is clear.

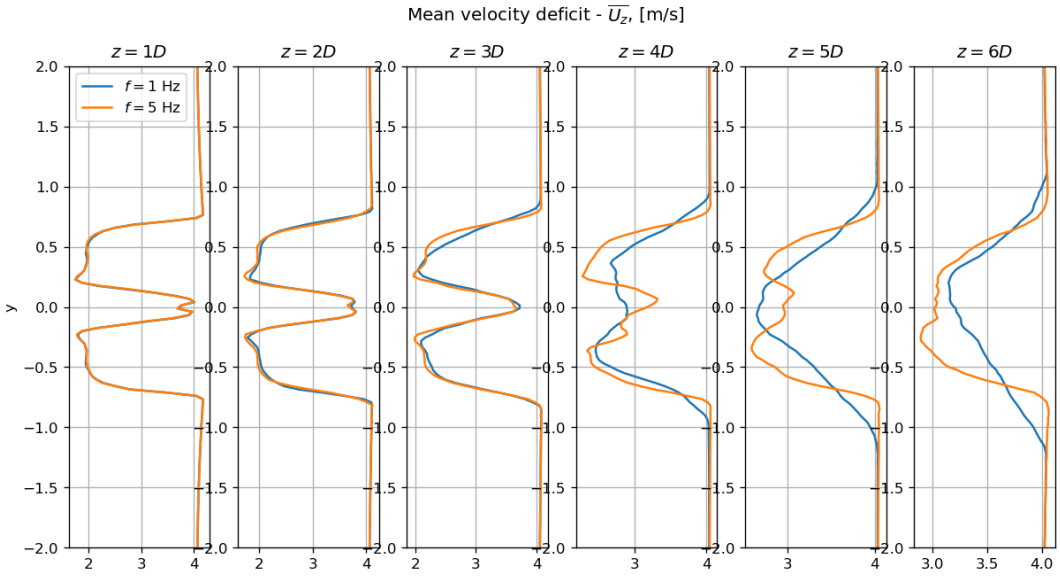

Figure 6.7: Comparison of mean velocity deficit for pitch cases, (averaged over the entire simulation).

7

2 DOF - Coupled motions

FOWT are often subjected to complex motions in multiple directions. In this chapter, the complexity of the motions is increased with coupled pitch/surge motions being investigated.

7.1. Cases description

Harmonic motions are still considered in this chapter, but they combine pitching and surging. Both motions are defined the very same way as before, with the only difference being the introduction of a phase parameter $\Delta\Phi$ in the pitch motion in order to enable a phase shift between the two motions.

The combined motion velocity at the rotor's centre is:

$$V_p = \Delta V_s^* U_\infty \cos(2\pi f_s t) + \frac{\Delta V_p^* U_\infty}{H_t} \cos\left(2\pi f_p t + \Delta\Phi\right) \tag{7.1}$$

Three configurations were considered: low frequency for both surge and pitch, high frequency for both, and a last one with low frequency for surge and high frequency for pitch. For each configuration, the motions have been considered both in phase and out-of-phase with $\Delta\Phi = 90°$.

The cases investigated are summarised in Table 7.1.

Case	ΔV_p^* [-]	f_p [Hz]	A_p [deg]	ΔV_s^* [-]	f_s [Hz]	A_s [cm]	$\Delta\Phi$ [deg]
PS005f1f1p0	0.072	1	2.25	0.05	1	3.18	0
PS005f1f1p90	0.072	1	2.25	0.05	1	3.18	90
PS005f5f5p0	0.072	5	0.45	0.05	5	0.64	0
PS005f5f5p90	0.072	5	0.45	0.05	5	0.64	90
PS005f5f1p0	0.072	5	0.45	0.05	1	3.18	0
PS005f5f1p90	0.072	5	0.45	0.05	1	3.18	90

Table 7.1: Reduced velocity and frequency of the harmonic 2 DOF motion cases investigated

7.2. Rotor loads - Thrust and Power

For coupled 2-DOF motions, it is not as evident as before to identify whether the loads obtained are in accordance with the quasi-steady theory. However, one can use the results obtained for single motions and linearly add them up. The quasi-steady prediction of the thrust becomes:

$$T_{QST} = T_0 + \Delta T_s \sin(2\pi f_s t + \phi_s) + \Delta T_p \sin\left(2\pi f_p t + \phi_p + \Delta\Phi\right) \tag{7.2}$$

Wherein $\Delta T_x = K_{VT}\Delta V$ with K_{VT} being defined in Equation 2.4 and obtained from the single DOF motions. For example, amplitudes of thrust variation $\Delta V_s = 0.48\ N$ and $\Delta V_s = 0.96\ N$ were found for, respectively, $\Delta V^* = 0.05$ and $\Delta V^* = 0.1$. This results in $K_{VT_s} = 2.40$, and the expected thrust variation due to surge can be computed with the surge reduced velocity. The phase shifts ϕ_x are again $-90°$

in QST. The same applies for pitch, where only the phase shift between the DOFs $\Delta\Phi$ is added. The same procedure is also used for the power.

Therefore, for each case considered, it is possible to plot the loads obtained in comparison with the quasi-steady predictions and see how well they match. Thrust and power time variations during one full period of motion and for all cases are plotted in Figure 7.1, Figure 7.2 and Figure 7.3. In addition, the amplitude of variations and mean values are given in the Table 7.2. The experimental results are also given for comparison. However, the two cases with different frequencies were not tested.

First, considering the configurations with both motions at low frequencies (Figure 7.1), what strikes first is the very good agreement between the QST prediction and the numerical results. Signal amplitudes are very similar and almost perfectly in phase. Because the motions have the same frequency, the loads are still sinusoidal, but with larger amplitudes, particularly when the two motions are in phase. One can still note a small offset in the thrust, with the numerical results being shifted downward. The same observation was made for single-DOF motions. The mean thrust is, thus, also slightly reduced compared to the static case. So is the mean power. In comparison with the experimental results, the same order of error is obtained as for single DOF motion, except for the mean power, which is greatly overestimated in numerical simulations.

Then, in the high-frequency cases, the same comments apply. However, the variations found experimentally are much larger, as the loads are again found to break down the quasi-steady theory at these frequencies.

Finally, for the two cases with low surge frequency and high pitch frequency, the response is no longer sinusoidal. Yet, one can clearly recognise the two sinusoidal responses superimposed. Again, the agreement with QST is found to be very good, with only a small offset for the thrust. This time, the two signals with different phase shifts have quite similar total amplitudes of variations.

In all cases, and particularly at low frequencies, the average power was found to be slightly reduced. Such a reduction was also found by Chen et al. [26] who imposed pitch/surge motions as well. However, they did not obtain a nice sinusoidal response when imposing motions of the same frequency.

On the other hand, Ramponi [11] who used FAST to impose a wide range of motions, including coupled pitch/surge, obtained an increase in average power in most cases without a controller. He also found that the potential gain in mean power, for motion of identical frequencies, was reduced for $\Delta\Phi = 90°$ compared to in-phase motions. The power is also found to be reduced with $\Delta\Phi = 90°$ here. However, the differences are less significant than in his work. Similarly, Lin et al. [25] also highlighted the great impact of the phase difference between the two motions on the power fluctuations.

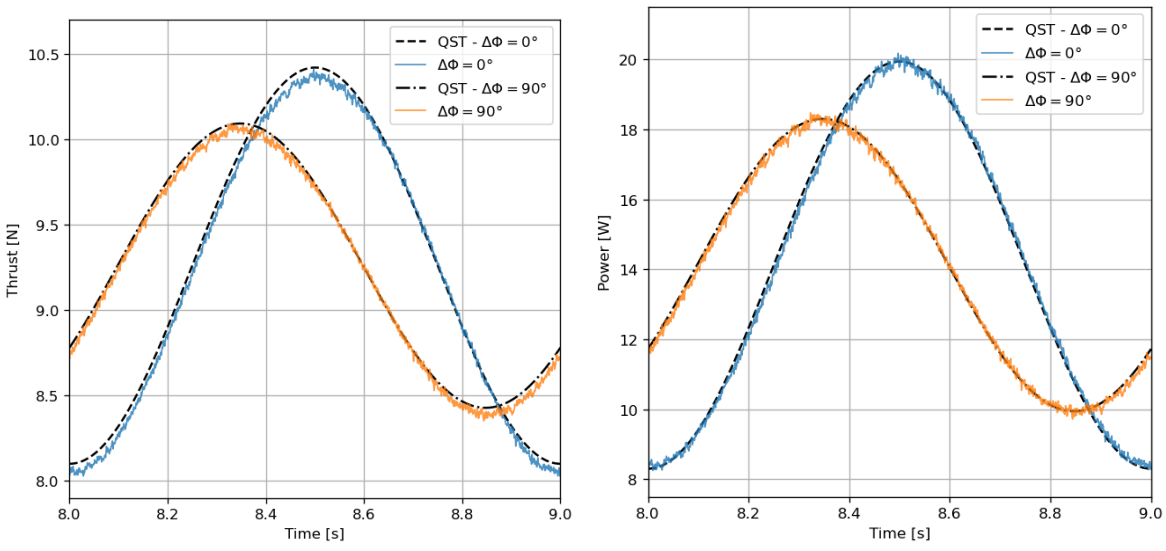

(a) Thrust (b) Power

Figure 7.1: Thrust and power for coupled motions with $f_s = f_p = 1\ Hz$

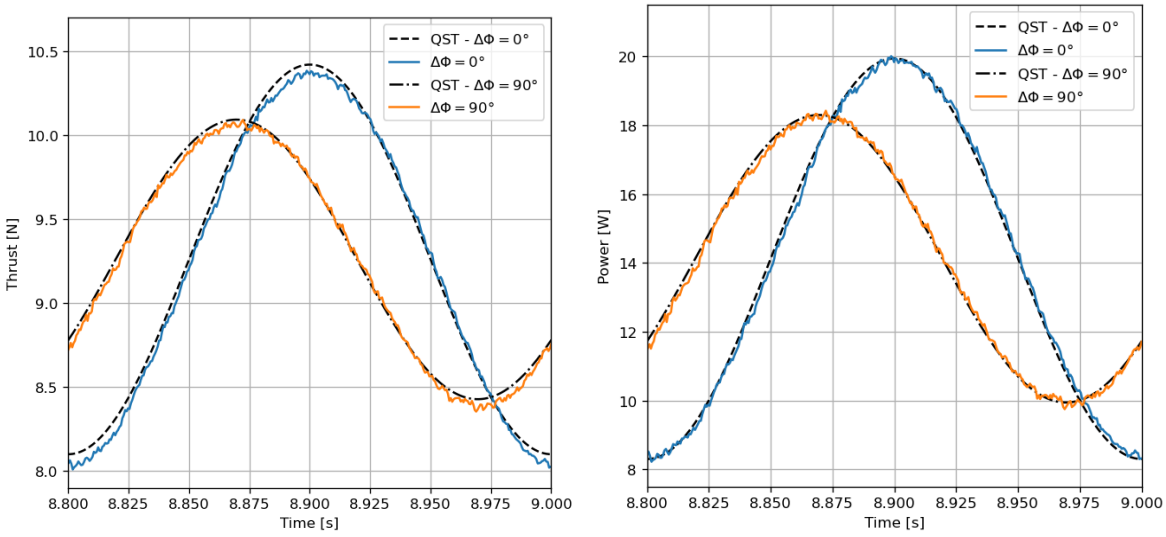

(a) Thrust (b) Power

Figure 7.2: Thrust and power for coupled motions with $f_s = f_p = 5\ Hz$

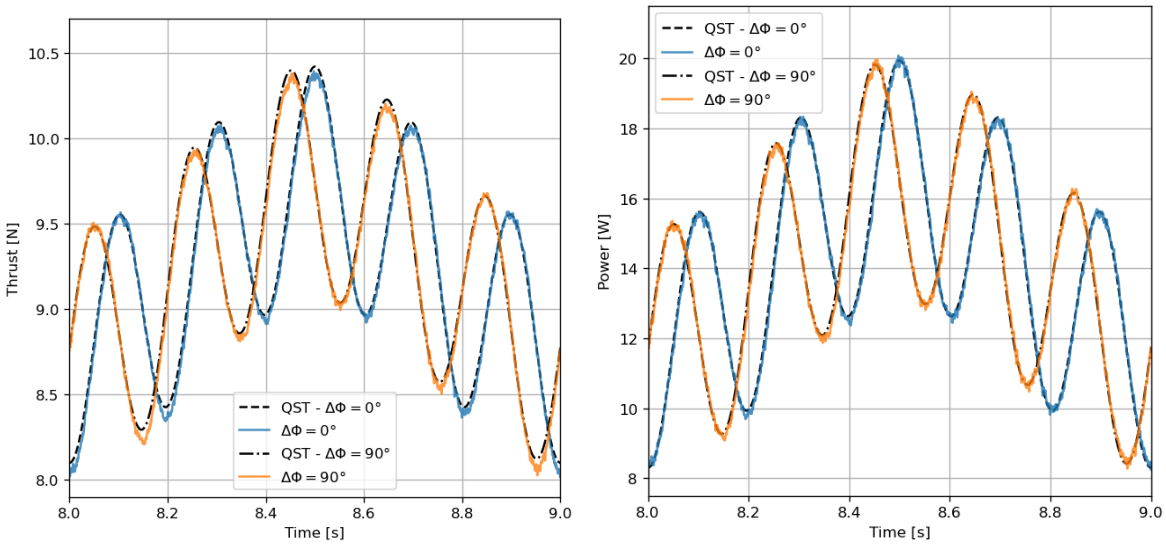

(a) Thrust (b) Power

Figure 7.3: Thrust and power for coupled motions with $f_s = 1\ Hz$, $f_p = 5\ Hz$

7.3. Local loads

Again, the same four probes along the blade span are used in order to obtain insights on the loads at the blade's level. For each case investigated, the angle of attack and the lift and drag coefficients are plotted with respect to time in Figure 7.4, Figure 7.5 and Figure 7.6.

In the very first case, with low-frequency motions in phase, the results are very similar to the ones obtained for low-frequency pitching only. The shapes of the plots are almost identical, with only the amplitude being increased by the additional surge motion. When pitch and surge are out of phase, the signals remain alike but are shifted.

The same comments apply for the high-frequency coupled motions. Again, the temporal evolution is very similar to the pitch-only one. This is also true for the low-frequency surge and high-frequency pitch cases.

Since the rotor loads were found to be well in accordance with the quasi-steady theory and to be a superimposition of the two single motion responses, it is only logical that this applies for the local loads

Source	Case	$\overline{T}$ [N]	ΔT [N]	$\overline{P}$ [W]	ΔP [W]
YALES2	PS005f1f1p0	9.22	1.16	14.06	5.80
	PS005f1f1p90	9.23	0.83	14.04	4.17
	PS005f5f5p0	9.23	1.16	14.11	5.76
	PS005f5f5p90	9.24	0.84	14.09	4.16
	PS005f5f1p0	9.24	1.16	14.07	5.79
	PS005f5f1p90	9.24	1.15	14.07	5.71
Exp.	PS005f1f1p0	9.35	1.36	9.69	5.96
	PS005f1f1p90	9.32	0.94	9.45	4.20
	PS005f5f5p0	9.32	2.72	9.66	/
	PS005f5f5p90	9.13	1.33	8.64	/

Table 7.2: Comparison of rotor loads for 2 DOF coupled motions

as well.

Finally, it should be noted that, despite the increased amplitude of variation for the angle of attack, the blades remain out of the stall region.

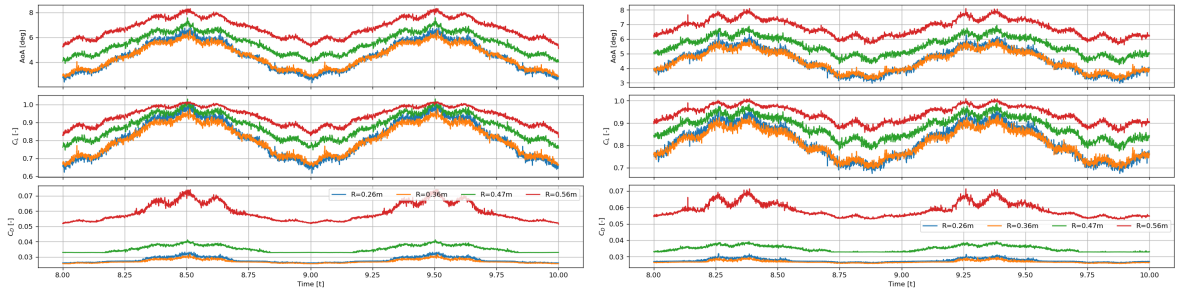

(a) $\Delta\phi = 0°$ (b) $\Delta\phi = 90°$

Figure 7.4: Local loads at four span locations for $f_s = f_p = 1\ Hz$

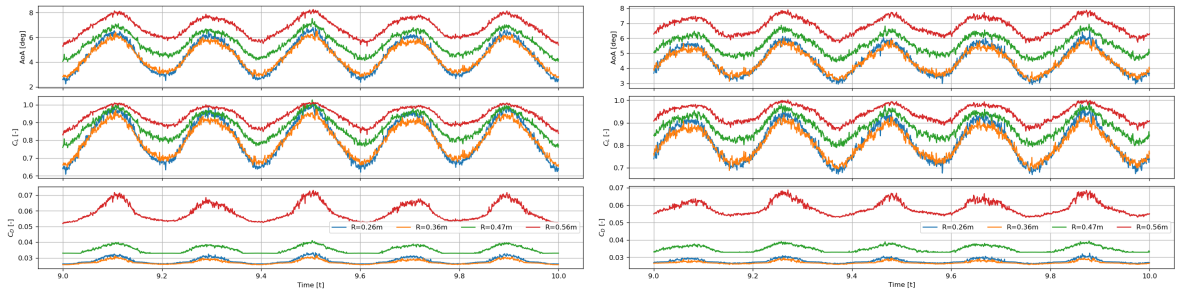

(a) $\Delta\phi = 0°$ (b) $\Delta\phi = 90°$

Figure 7.5: Local loads at four span locations for $f_s = f_p = 5\ Hz$

7.4. Wake behaviour

After the loads at the rotor and blade scales, this section investigates the impact of the coupled motion on the turbine's wake.

7.4.1. Vortical structures

Previous chapters have highlighted the formation of vortex rings when the frequency of surge or pitch was sufficiently large. In order to see if particular vortical structures are formed in 2DOF motions, the vorticity fields in the $x = 0$ plane and at $t = 0\ s$ are given for every case in Figure 7.7. In addition, iso-contours of the Q-criterion are plotted to identify three-dimensional structures in Figure 7.8.

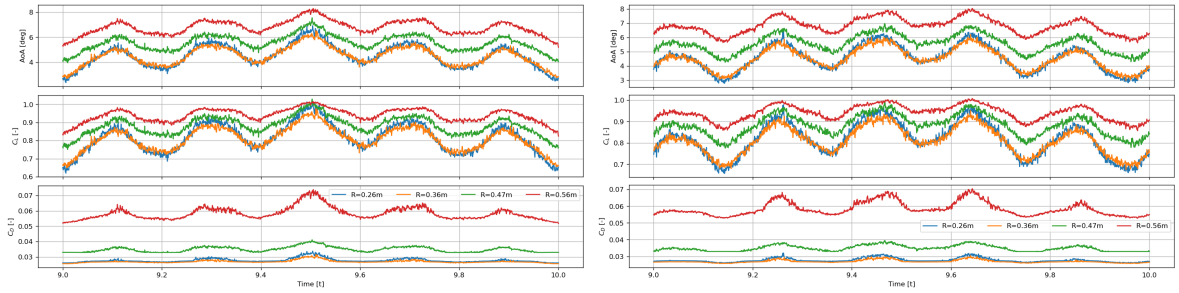

(a) $\Delta\phi = 0^\circ$ (b) $\Delta\phi = 90^\circ$

Figure 7.6: Local loads at four span locations for $f_s = 1\ Hz$, $f_p = 5\ Hz$

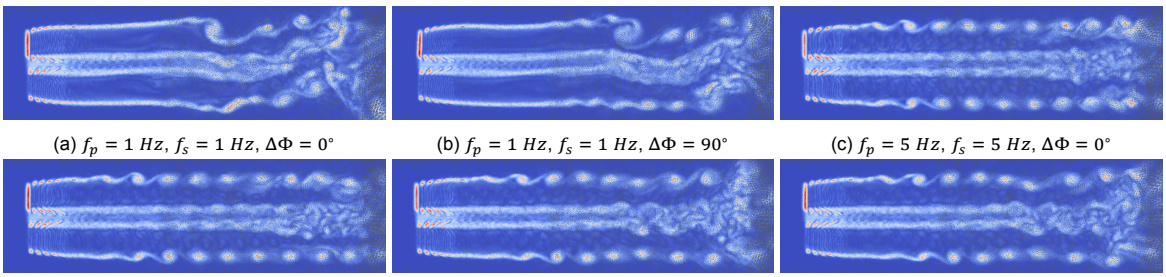

(a) $f_p = 1\ Hz$, $f_s = 1\ Hz$, $\Delta\Phi = 0^\circ$ (b) $f_p = 1\ Hz$, $f_s = 1\ Hz$, $\Delta\Phi = 90^\circ$ (c) $f_p = 5\ Hz$, $f_s = 5\ Hz$, $\Delta\Phi = 0^\circ$

(d) $f_p = 5\ Hz$, $f_s = 5\ Hz$, $\Delta\Phi = 90^\circ$ (e) $f_p = 5\ Hz$, $f_s = 1\ Hz$, $\Delta\Phi = 0^\circ$ (f) $f_p = 5\ Hz$, $f_s = 1\ Hz$, $\Delta\Phi = 90^\circ$

Figure 7.7: Vorticity fields in the $x = 0$ plane for 2DOF motions at $t = 10\ s$

First, concerning the cases at low pitch and surge frequencies, the wake is very similar to the one obtained for pitch only at this frequency. Indeed, a similar large vortex is formed in the upper part of the wake and about the same distance from the rotor as for pitch only. Again, this vortex creates a vertical undulation in the wake. The in-phase and out-of-phase cases are comparable, they are simply at a different stage of development since they are plotted for the same time step with a phase shift in pitch motion. Between the two motions, pitching appears to be the dominant one for the behaviour of the wake at these frequencies.

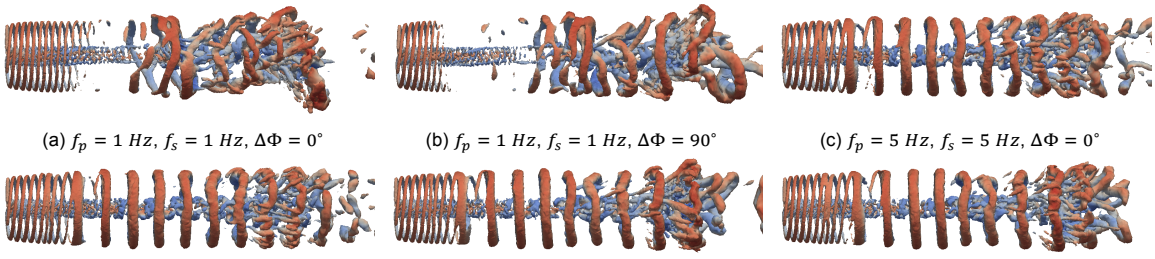

(a) $f_p = 1\ Hz$, $f_s = 1\ Hz$, $\Delta\Phi = 0^\circ$ (b) $f_p = 1\ Hz$, $f_s = 1\ Hz$, $\Delta\Phi = 90^\circ$ (c) $f_p = 5\ Hz$, $f_s = 5\ Hz$, $\Delta\Phi = 0^\circ$

(d) $f_p = 5\ Hz$, $f_s = 5\ Hz$, $\Delta\Phi = 90^\circ$ (e) $f_p = 5\ Hz$, $f_s = 1\ Hz$, $\Delta\Phi = 0^\circ$ (f) $f_p = 5\ Hz$, $f_s = 1\ Hz$, $\Delta\Phi = 90^\circ$

Figure 7.8: Iso-contours of Q-criterion= 20 at $t = 10.0\ s$, coloured by velocity magnitude, 2DOF coupled motions

At high frequencies, vortex rings were formed for both single-pitch and single-surge motions. In pitch/surge with motions of the same high frequencies, vortex rings also appear in the wake. In addition, they form about the same distance from the rotor as in 1-DOF motions. A noticeable difference between 1-DOF pitch and surge was the absence of symmetry between the upper part and lower part of the wake in pitch. Indeed, if the vorticity field was almost perfectly symmetrical in surge motion, the vortices were formed later downwind in the lower part in pitch motion. Here, for coupled motions, the symmetry is broken again, but the difference between the upper vortex and the lower one at a certain z location is less significant than for pitch. Later in the wake, the vortex rings seem to break down earlier due to the coupled motions than in the 1-DOF cases. In contrast with the low-frequency cases, certain vortices collide in the near wake. Again, the phase shift $\Delta\Phi$ do not create any major difference in the wake behaviour.

Finally, vortex rings are also formed in configurations with low surge and high pitch frequencies. The wake flow is comparable with the one obtained for high-frequency 1-DOF pitch, with a break in symmetry between the upper and lower parts of the wake. Once again, the wake flow in 2DOF seems principally driven by the pitch motion. Collisions between the tip vortices in the near wake are also experienced. However, a difference between the 1-DOF pitch case and the previous high-frequency 2-DOF motions, is that the vortices constituting the vortex rings are no longer aligned in the $z-$ direction. A certain undulation in the boundaries of the wake starts to appear. In particular, this causes a vortex ring to contract at the upper part and causes an earlier breakdown of these vortical structures.

In order to further investigate this phenomenon, the vorticity fields are given for several time steps during one full period of motion in Figure 7.9 for the case: $f_p = 5\ Hz$, $f_s = 1\ Hz$, $\Delta\Phi = 90°$.

On the first snapshot (Figure 7.9a), at $t = 9\ s$, one can notice that a certain vortex in the upper part of the wake is going down and creates a space with the previous vortex downwind. As time passes and until about $t = 9.5\ s$ (Figure 7.9e), this vortex keeps going, and the gap with the previous vortex increases. The vortex going inside, it slows down its progression. Therefore, in the meantime, the distance to the next vortex upwind decreases. As the vortical structures become too close to each other, they collide, and the far wake structure blows up. Finally, on the last snapshot (Figure 7.9i), the cycle starts again.

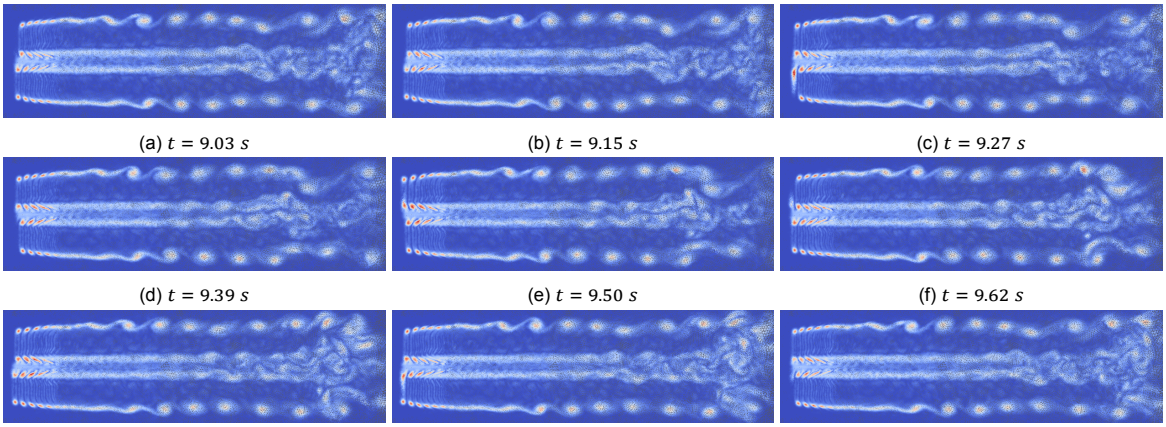

(a) $t = 9.03\ s$ (b) $t = 9.15\ s$ (c) $t = 9.27\ s$

(d) $t = 9.39\ s$ (e) $t = 9.50\ s$ (f) $t = 9.62\ s$

(g) $t = 9.74\ s$ (h) $t = 9.86\ s$ (i) $t = 9.97\ s$

Figure 7.9: Vorticity fields in the $x = 0$ plane during $T = 1\ s$, for the case $f_p = 5\ Hz$, $f_s = 1\ Hz$, $\Delta\Phi = 90°$

7.4.2. Velocity deficit

On the mean velocity, one can first compare the mean U_z profile along the wake and compare the different cases (see Figure 7.10). Again, it appears that the phase shift $\Delta\Phi$ has only a slight effect on this wake quantity. In addition, the motions with identical high pitch frequencies, no matter the surge frequency, have similar velocity deficits. Once again, it seems that the pitch motion is dominant in determining the wake behaviour (keeping in mind that the actual reduced velocity corresponding to pitching is larger than for surging). The cases with low pitch and surge frequencies present the best wake recovery on average, with, in particular, the velocity gradient being less steep.

However, when looking at the temporal evolution of the velocity deficit and not the average for these cases (see Figure 7.11), one observes large temporal differences. It can also be observed that the two time steps separated by one period of motion are almost identical, stating that the impact of the motion is clearly visible, even at the furthest locations downwind. In addition, the undulation of the wake created by the large vortex discussed previously, can be retrieved in the velocity deficit as the symmetry is broken at certain time steps. This is particularly true for the configuration in which the two motions are in phase.

In comparison, the velocity deficit for the high-frequency cases (Figure 7.12) shows much less temporal dependency. However, the profiles separated by one period of motion are less comparable. The symmetry of the wake, on the other hand, is well conserved, even if, again, bigger differences appear when the motions are in phase.

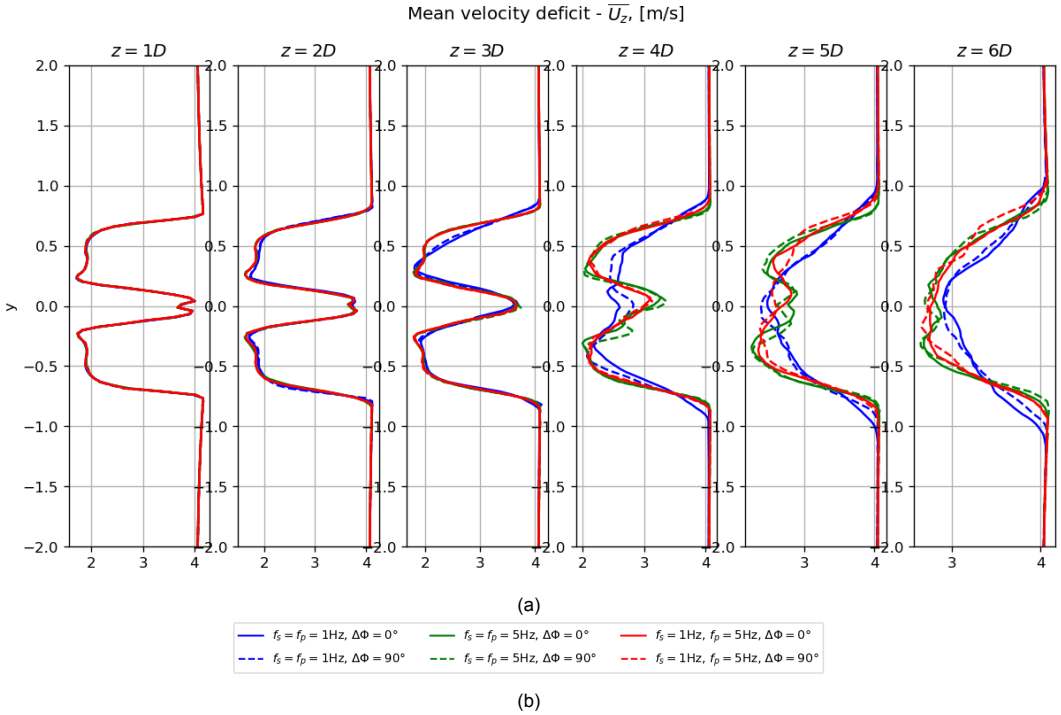

Figure 7.10: Mean profile of U_z at six locations along the wake for the 2DOF motions, averaged over the total simulation duration

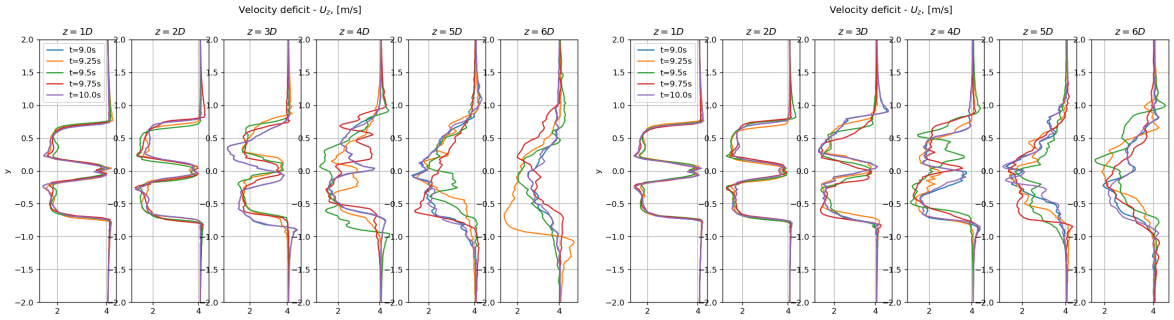

Figure 7.11: Instantaneous U_z at six locations along the wake for several time steps, $f_p = 1\ Hz$, $f_s = 1\ Hz$

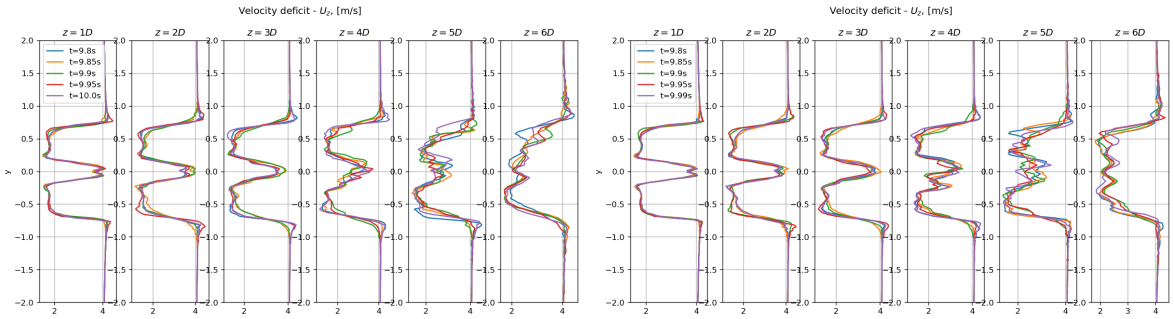

Figure 7.12: Instantaneous U_z at six locations along the wake for several time steps, $f_p = 5\ Hz$, $f_s = 5\ Hz$

Finally, the profiles of the streamwise component of velocity U_z for the cases with different pitch and surge frequencies are plotted in Figure 7.13. If the the mean profiles were very similar to the high-

frequency cases, the differences between the time steps are, on the other hand, significant, as in the low-frequency cases. In addition, one can note that the symmetry is pretty well conserved and that the profiles separated by $T = 1\ s$ are very similar. Therefore, if the mean profiles suggested that the wake deficit is mostly determined by the pitch motion, it now appears that the low-frequency surge motion still has a significant impact on the wake.

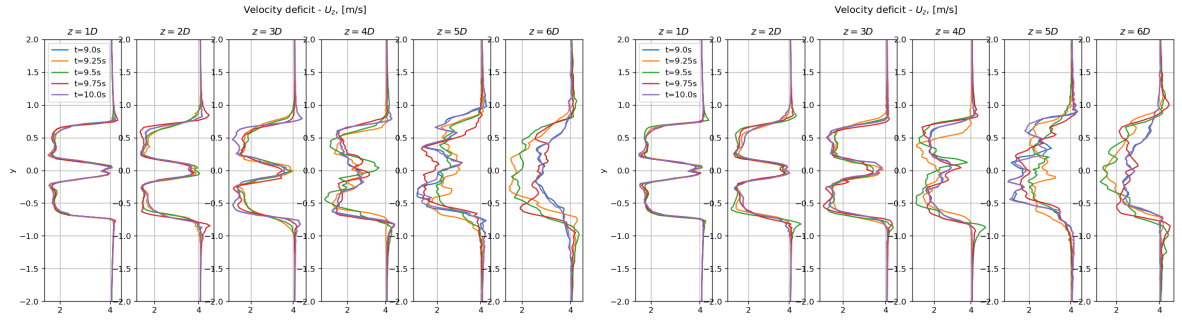

(a) $\Delta\Phi = 0°$ (b) $\Delta\Phi = 90°$

Figure 7.13: Instantaneous U_z at six locations along the wake for several time steps, $f_p = 5\ Hz$, $f_s = 1\ Hz$

7.4.3. Motion signature in the wake

In order to further investigate the question of whether a signature of the motion can be retrieved in the wake, one should do a spectral analysis and look at the peaks corresponding to the motion frequencies.

For this purpose, the velocity along the different probe lines will, once again, be used. However, certain temporal variations are visible in the vertical or horizontal direction (vortex in $x = 0$ plane), while others are in the wind direction. Therefore, it is looked at the sum of the perturbations, defined as the difference between the velocity component and its average:

$$\sqrt{\sum_{i=x,y,z} U_i'^2} = \sqrt{(U_x - \overline{U_x})^2 + (U_y - \overline{U_y})^2 + (U_z - \overline{U_z})^2} \tag{7.3}$$

In order to look globally at the wake and not at one precise location, this quantity is integrated along each probe line (between $y = -2\ m$ and $y = +2\ m$). The power spectral density is then taken.

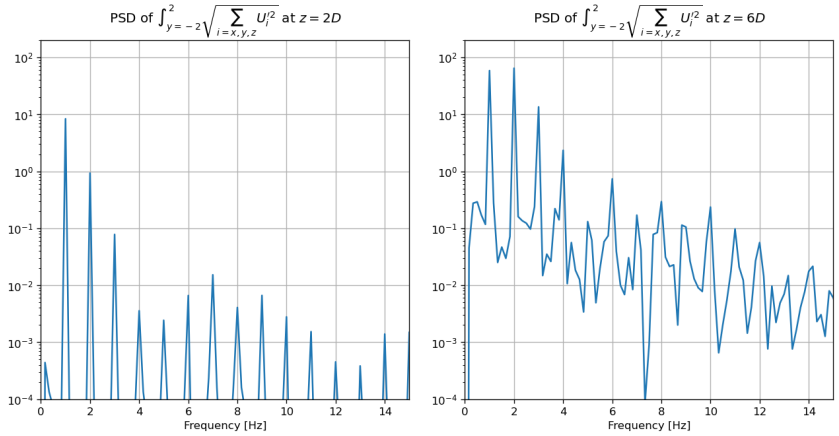

(a) $z = 2D$ (b) $z = 6D$

Figure 7.14: PSD for $f_p = 1\ Hz$, $f_s = 1\ Hz$ and $\Delta\Phi = 0°$ at two wake locations

First, the PSD analysis for the two low-frequency cases is given in Figure 7.14 and Figure 7.15 for, respectively, $\Delta\Phi = 0°$ and $\Delta\Phi = 90°$. Only two probe lines are given: $z = 2D$ in the near wake and $6D$ in the far wake. At $z = 2D$, the peak at motion frequency $f = 1\ Hz$ is clearly visible, for both phase shift

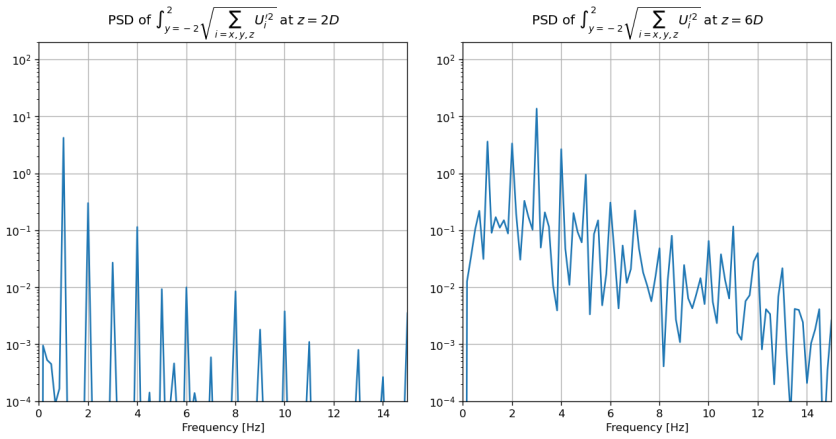

(a) $z = 2D$ (b) $z = 6D$

Figure 7.15: PSD for $f_p = 1\ Hz$, $f_s = 1\ Hz$ and $\Delta\Phi = 90°$ at two wake locations

values. However, further downstream at $z = 6D$, it is more difficult to find the signature of the wake, particularly when the two motions are out of phase.

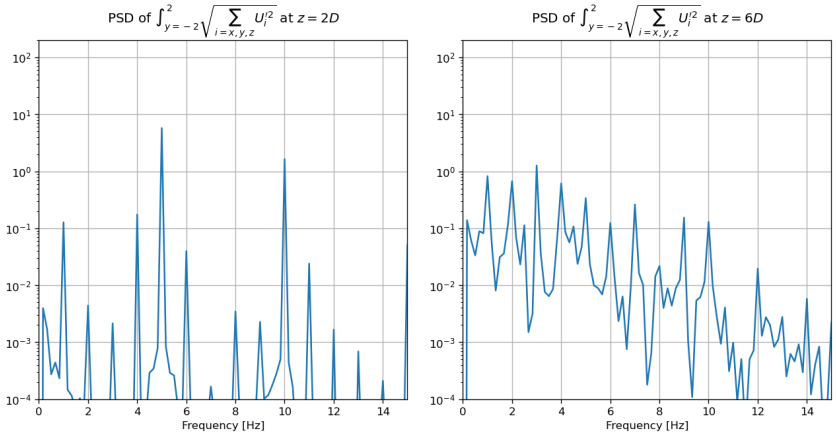

(a) $z = 2D$ (b) $z = 6D$

Figure 7.16: PSD for $f_p = 5\ Hz$, $f_s = 5\ Hz$ and $\Delta\Phi = 0°$ at two wake locations

Then, the same outputs are plotted for the high-frequency cases in Figure 7.16 and Figure 7.17. Again, the motion frequency is clearly recognisable at the near wake location, without any significant difference between the two phase shift configurations. In addition, the high-frequency peak is not more visible in the far wake than in the previous cases. However, this time, the signature is slightly more significant when the motions are out of phase.

Finally, for the motions with different surge and pitch frequencies, the same outputs are plotted at every probe line. This is plotted in Figure 7.18 for $\Delta\Phi = 0°$ and in Figure 7.19 for $\Delta\Phi = 90°$.

Comparing the two phase shift configurations, it appears that there are barely any discrepancies in the near wake ($z = 1D$, $2D$ and $3D$). Then some differences appear, but they are not particularly significant for the two peaks of interest ($f = 1\ Hz$ and $f = 5\ Hz$). Then, the following comments apply for both phase shift values:

In the near wake ($z = 1D$, $2D$ and $3D$), the two peaks are clearly recognisable and are the dominant ones. The high-frequency one, corresponding to pitch motion, is particularly powerful. Further downstream in the wake ($z = 4D$, $5D$ and $6D$), the high frequency peak fades out, but the low frequency one, corresponding to the surge, is still dominant. This is a difference with the configurations with the motion at the same frequencies, in which the motion did not leave a clear signature in the far wake.

In comparison, Schliffke [96] was not able to experimentally identify a clear signature in the wake

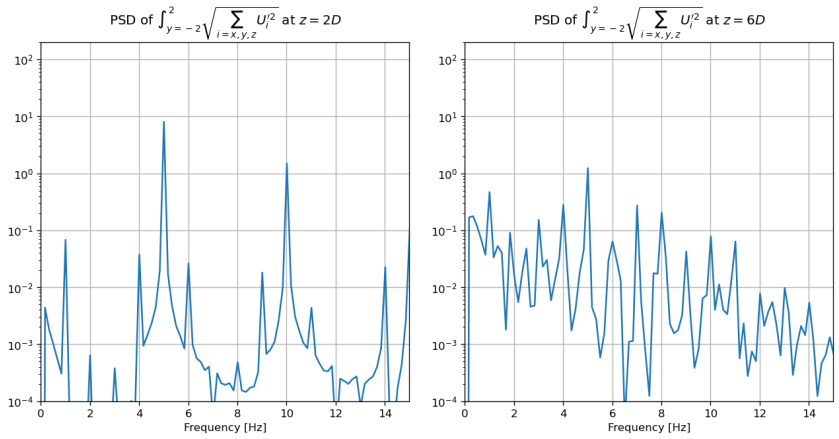

(a) $z = 2D$ (b) $z = 6D$

Figure 7.17: PSD for $f_p = 5\ Hz$, $f_s = 5\ Hz$ and $\Delta\Phi = 90°$ at two wake locations

with 3 DOF (additional heave motion) or more realistic motions. However, this was attributed to the low amplitudes of motion investigated for these motions.

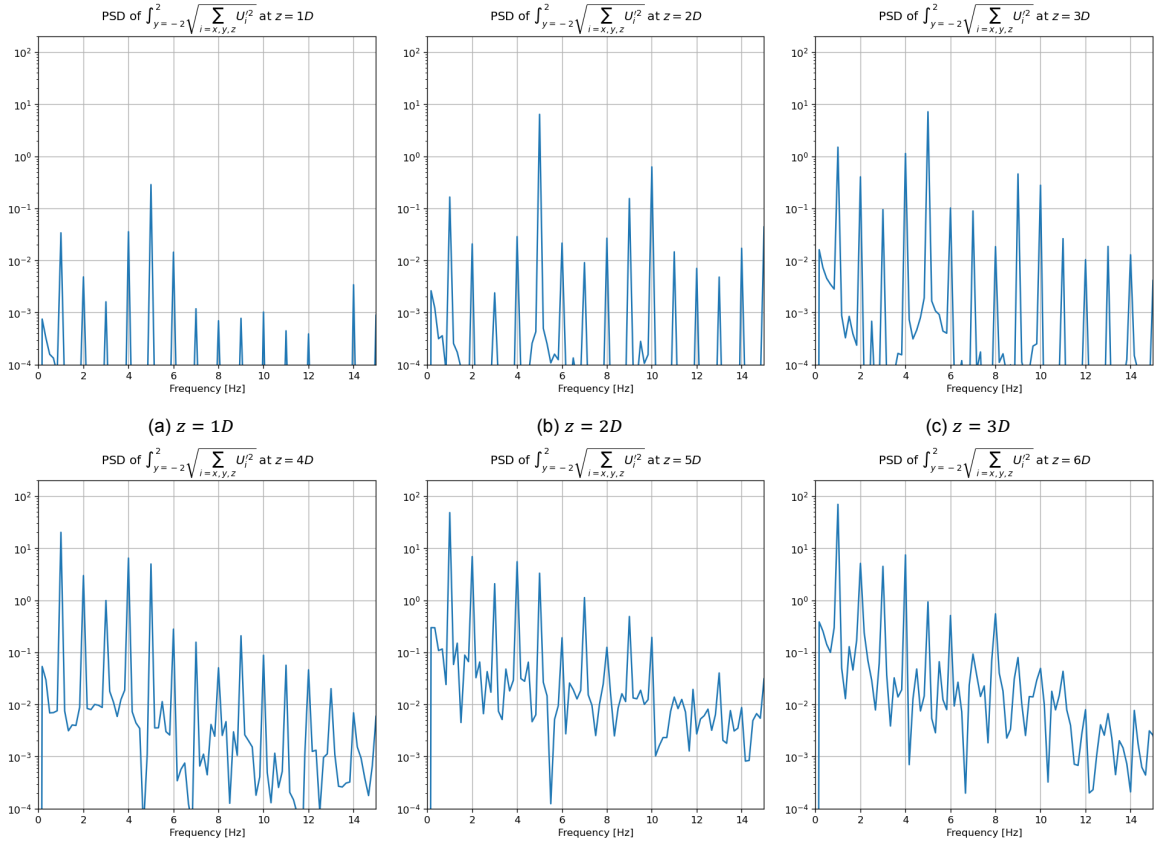

(a) $z = 1D$ (b) $z = 2D$ (c) $z = 3D$

(d) $z = 4D$ (e) $z = 5D$ (f) $z = 6D$

Figure 7.18: PSD for $f_p = 5\ Hz$, $f_s = 1\ Hz$ and $\Delta\Phi = 0°$ at six wake locations

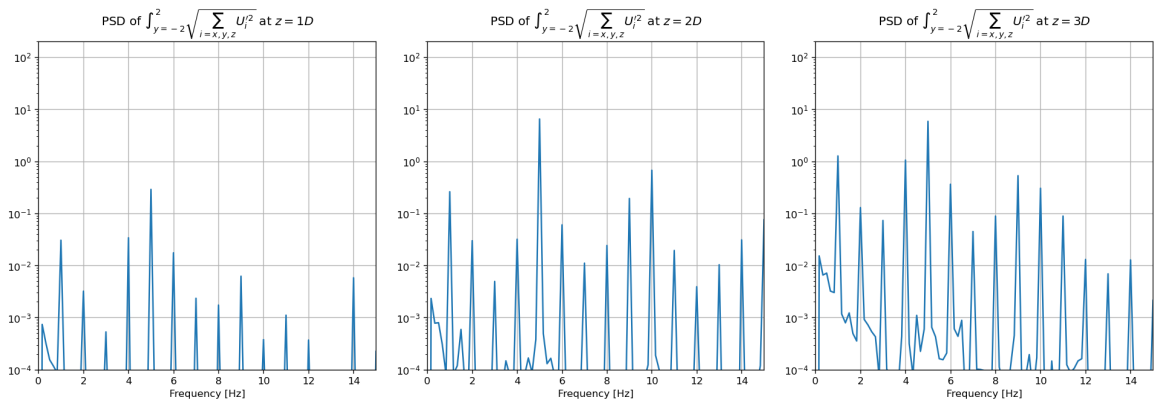

(a) $z = 1D$ (b) $z = 2D$ (c) $z = 3D$

(d) $z = 4D$ (e) $z = 5D$ (f) $z = 6D$

Figure 7.19: PSD for $f_p = 5\ Hz$, $f_s = 1\ Hz$ and $\Delta\Phi = 90°$ at six wake locations

8

Conclusion and outlook

8.1. Conclusion

In this present work, the large-eddy simulation code YALES2 implemented with an actuator line approach has been used to study the response of a scale rotor of the DTU 10MW subject to floating motion. Both one-degree-of-freedom and two-degrees-of-freedom harmonic motions in the surge and pitch directions have been imposed. Different frequencies and normalised motion velocities were considered.

A special focus was placed on comparing the computed rotor loads in terms of thrust and power with those of an experimental campaign run on this scale rotor at TU Delft. The time variations of the loads at scale level were also looked at. Finally, it was researched and commented on how the wake behaved in reaction to these motions, especially in the area around the rotor.

In the introduction, five sub-questions were advanced to address the main research question; here is their response, summarising the conclusions made in this work:

- *Is it feasible to model FOWTs subjected to coupled floating motions with large-eddy simulations using YALES2 in combination with an actuator line approach?*

  Two-degrees-of-freedom motions were successfully imposed using the ALM code developed by Ricardo Amaral. It is capable of dealing with motions from 1 to 6 DOFs by only prescribing a certain velocity as a function of time for each degree-of-freedom considered. This is a great advantage of the actuator line approach, in comparison with blade-resolved LES, in which it is more complicated to account for the motion (motion of the mesh, etc.). As will be discussed later in the next section, some improvements could still be made to the code. For instance, the capacity of the model to deal with Reynolds-dependent polars could significantly improve the accuracy of the results, especially for large motions.

  Yet, a possible limitation in the use of ALM with imposed motions of moderate amplitude was highlighted. ALM permits increasing the cell width near the rotor and lowering the number of cells and computational cost of LES. However, when the amplitude of motion is too small in comparison with the cell width, the blade elements do not travel across a sufficient number of cells, and this is believed to alter the results. Some tests were performed on this particular matter but did not highlight significant differences. Yet, it is difficult to say how the results were altered by this issue, and a more thorough study is needed.

- *What are the discrepancies between large-eddy simulations and low- to mid-fidelity models for the behaviour of a FOWT subjected to coupled floating motions?*

  On the scale model considered, the results were compared with AeroDyn's results (BEM, lower fidelity) only in the static cases. If very low differences were found in the thrust, much larger ones appeared in the torque and power. In addition, these discrepancies are increasing with decreasing freestream velocity; it is not only an offset.

Concerning the 2-DOF cases, the work of Ramponi [11] provides some insights on the impact of such motions on the loads without a controller. If he observed a significant increase in the mean power of the rotor subject to coupled pitch/surge motions, much smaller differences were obtained in this present work. Yet, the same trend of the potential gain in power being reduced for $\Delta\Phi = 90°$ was noticed. However, it is difficult to directly compare the results obtained as the rotor under consideration is different. In addition, some uncertainty exists about the use of correction models at the tips for both the BEM and ALM approaches.

- *How well are large-eddy simulation results comparable with experimental results for the unsteady behaviour of FOWTs?*

  First, concerning the mean loads, the same observation is made as for the comparison with FAST results. Indeed, low differences are identified for the mean trust but much larger ones for the mean power. The experimental mean power measured is significantly lower. This is true for both 1-DOF surging and pitching, as well as for coupled motions.

  In this study, particular interest was given to the amplitude of the temporal variations of the loads. This is a key measure to estimate the degree of unsteadiness of the loads. If a pretty good agreement is obtained at low frequencies, significant differences appear at high frequencies. Indeed, the numerical results are always in accordance with the quasi-steady theory, while a significant increase in the amplitude of oscillations was observed in the experiment. This represents a key issue and will later need to be further investigated.

- *Is it possible to obtain local and detailed insight into the airflow at blade level using actuator lines in combination with LES?*

  The angle of attack and the local loads were successfully obtained at various locations along the blades. This is an advantage of using actuator lines, as many flow information are available at each blade element. This is important information when studying control strategies, for example.

  For 1-DOF pitching, local variations at the rotor's frequency were highlighted in contrast with 1-DOF surging. On coupled motions, temporal variations at frequencies different from those of motion were also observed.

- *Can the near-wake behaviour and its main features be captured in response to the imposed motions?*

  In the numerical setup, a fine mesh resolution was kept in the near- and mid- wake. This permitted to capture the development of the wake in these regions. In particular, the formation of vortex rings was observed at high frequencies for both 1-DOF surge and pitch motions. A test on a surge case with a higher resolution was made, and the same characteristics were obtained.

  On the coupled motions, a focus was given to the impact of each degree-of-freedom along the wake. Surging and pitching were found to both have an impact on the wake, depending on their frequency, and also depending on whether the mean or perturbation characteristics are considered.

Finally, the main research question was:

How do high-fidelity large-eddy simulations compare with experimental and low- to mid-fidelity models for the aerodynamic behaviour of a FOWT subjected to two degrees of freedom floating motions?

In brief, the numerical results compared pretty well with the BEM's results available and the experimental ones, even though significant differences can appear for the power in particular. Yet, major discrepancies were observed at high frequencies, as a breakdown in quasi-steady theory was observed in the experiment and not in the simulations. This constitutes the main question future works should address to continue this study. Finally, the use of large-eddy simulations combined with an actuator line approach, permitted the acquisition of further information, such as local loads or insights on the wake.

8.2. Outlook - Future developments

This section discusses the possible upgrades and potential follow-up tasks that might be accomplished to carry out this investigation further.

First, the main issue highlighted in the present work is the significant difference between the numerical and experimental results at high frequency.

One of the main limitations of the code is its inability to deal with Reynolds-dependent polars. This issue could be an explanation for the significant discrepancies between the experiment and the simulations. Some work could be performed in order to include this feature in the code and check whether it has a significant impact.

At high frequency, unsteady phenomena are also encountered at the blade's level with time variations in angle of attack. In these conditions, the relation between the lift coefficient, in particular, and the angle of attack is no longer linear. YALES2 already has some dynamic stall models implemented, but there is not much literature available or explanation on how they actually operate. Some work could be done to check how using such a dynamic stall model can possibly increase the accuracy of the results.

Another possible explanation advanced is the potential vibrations experienced by the blades and/or the tower. Even if the natural frequencies of these elements are far from the motion frequencies, this could be thoroughly checked in the experiment or accounted for in the numerical model using a FSI approach.

Continuing on the possible improvements to the code YALES2, some work is currently being done by Ricardo Amaral in order to improve the actuator line approach to specifically account for the tower and the nacelle. Once this is done, it can be pertinent to take them into account and see if they induce significant differences both in the loads and in the wake behaviour.

Regarding the cases investigated, only 1-DOF and 2-DOF harmonic motions have been imposed. It could be interesting to impose on the rotor more realistic motions. In particular, complex 6-DOF temporal sequences were imposed in the experiment, and the results could be compared.

It could also be chosen to move aside from the experimental campaign and subject the rotor to more realistic flow conditions. For example, turbulent and/or sheared inflows could be considered. In addition, control strategies could be tested and the results qualified, with the power being limited to a maximum value, for instance.

Finally, concerning the wake, the results obtained were compared with other results from numerical simulations. It could be pertinent to validate the observations made with experimental results as well. Yet, it can be very difficult and expensive to design an experiment with the purpose of observing three-dimensional vortical structures.

On the numerical model, the resolution of the wake could be extended to the far-wake in order to properly estimate the wake recovery and provide insightful information for wind farm considerations.

Bibliography

[1] IPCC, “Climate change 2022: Mitigation of climate change,” The Intergovernmental Panel on Climate Change, 2022.

[2] IRENA, “World energy transitions outlook 2022: 1.5°c pathway,” International Renewable Energy Agency, 2022.

[3] R. Williams, F. Zhao, and J. Lee, “Global offshore wind report 2022,” Global Wind Energy Council, (GWEC), Jun. 29, 2022.

[4] GWEC, “Floating offshore wind – a global opportunity,” Global Wind Energy Council, (GWEC), Mar. 2022.

[5] G. E. Barter, A. Robertson, and W. Musial, “A systems engineering vision for floating offshore wind cost optimization,” *Renewable Energy Focus*, vol. 34, pp. 1–16, Sep. 1, 2020. DOI: 10.1016/j.ref.2020.03.002.

[6] C. Maienza, A. M. Avossa, F. Ricciardelli, D. Coiro, G. Troise, and C. T. Georgakis, “A life cycle cost model for floating offshore wind farms,” *Applied Energy*, vol. 266, p. 114 716, May 15, 2020. DOI: 10.1016/j.apenergy.2020.114716.

[7] M. Barooni, T. Ashuri, D. V. Sogut, S. Wood, and S. G. Taleghani, “Floating offshore wind turbines: Current status and future prospects,” pp. 1–28, 2022, Publisher: MDPI.

[8] D. Micallef and A. Rezaeiha, “Floating offshore wind turbine aerodynamics: Trends and future challenges,” *Renewable and Sustainable Energy Reviews*, vol. 152, p. 111 696, Dec. 1, 2021. DOI: 10.1016/j.rser.2021.111696.

[9] P. Benard, A. Viré, V. Moureau, *et al.*, “Large-eddy simulation of wind turbines wakes including geometrical effects,” *Computers & Fluids*, vol. 173, pp. 133–139, Sep. 2018. DOI: 10.1016/j.compfluid.2018.03.015.

[10] S. Cioni, F. Papi, L. Pagamonci, *et al.*, “On the characteristics of the wake of a wind turbine undergoing large motions caused by a floating structure: An insight based on experiments and multi-fidelity simulations from the OC6 phase III project,” Fluid mechanics/Wind turbine aerodynamics, preprint, Mar. 6, 2023. DOI: 10.5194/wes-2023-21.

[11] R. Ramponi, “Investigation of the effect of prescribed coupled motions in the power production of a floating offshore wind turbine,” Ph.D. dissertation, 2022.

[12] J. M. Jonkman, “Dynamics of offshore floating wind turbines—model development and verification,” *Wind Energy*, vol. 12, no. 5, pp. 459–492, 2009. DOI: 10.1002/we.347.

[13] D. Hu, L. Deng, and L. Zeng, “Study on the aerodynamic performance of floating offshore wind turbine considering the tower shadow effect,” *Processes*, vol. 9, no. 6, p. 1047, Jun. 2021, Number: 6 Publisher: Multidisciplinary Digital Publishing Institute. DOI: 10.3390/pr9061047.

[14] T. Sebastian and M. Lackner, “Characterization of the unsteady aerodynamics of offshore floating wind turbines,” *Wind Energy*, vol. 16, no. 3, pp. 339–352, 2013. DOI: 10.1002/we.545.

[15] A. J. Goupee, B. J. Koo, R. W. Kimball, K. F. Lambrakos, and H. J. Dagher, “Experimental comparison of three floating wind turbine concepts,” *Journal of Offshore Mechanics and Arctic Engineering*, vol. 136, no. 2, Mar. 24, 2014. DOI: 10.1115/1.4025804.

[16] A. N. Robertson, F. Wendt, J. M. Jonkman, *et al.*, “OC5 project phase II: Validation of global loads of the DeepCwind floating semisubmersible wind turbine,” *Energy Procedia*, 14th Deep Sea Offshore Wind R&D Conference, EERA DeepWind’2017, vol. 137, pp. 38–57, Oct. 1, 2017. DOI: 10.1016/j.egypro.2017.10.333.

[17] Y. Liu, Q. Xiao, A. Incecik, C. Peyrard, and D. Wan, “Establishing a fully coupled CFD analysis tool for floating offshore wind turbines,” *Renewable Energy*, vol. 112, pp. 280–301, Nov. 1, 2017. DOI: 10.1016/j.renene.2017.04.052.

[18] P. Cheng, Y. Huang, and D. Wan, “A numerical model for fully coupled aero-hydrodynamic analysis of floating offshore wind turbine,” *Ocean Engineering*, vol. 173, pp. 183–196, Feb. 1, 2019. DOI: 10.1016/j.oceaneng.2018.12.021.

[19] Z. Yu, Q. Ma, X. Zheng, K. Liao, H. Sun, and A. Khayyer, “A hybrid numerical model for simulating aero-elastic-hydro-mooring-wake dynamic responses of floating offshore wind turbine,” *Ocean Engineering*, vol. 268, p. 113 050, Jan. 15, 2023. DOI: 10.1016/j.oceaneng.2022.113050.

[20] J. Wang, C. Wang, O. D. Castañeda, F. Campagnolo, and C. L. Bottasso, “Large-eddy simulation of scaled floating wind turbines in a boundary layer wind tunnel,” *Journal of Physics: Conference Series*, vol. 1037, no. 7, p. 072 032, Jun. 2018, Publisher: IOP Publishing. DOI: 10.1088/1742-6596/1037/7/072032.

[21] H. M. Johlas, L. A. Martínez-Tossas, D. P. Schmidt, M. A. Lackner, and M. J. Churchfield, “Large eddy simulations of floating offshore wind turbine wakes with coupled platform motion,” *Journal of Physics: Conference Series*, vol. 1256, no. 1, p. 012 018, Jul. 2019, Publisher: IOP Publishing. DOI: 10.1088/1742-6596/1256/1/012018.

[22] H. M. Johlas, L. A. Martínez-Tossas, M. A. Lackner, D. P. Schmidt, and M. J. Churchfield, “Large eddy simulations of offshore wind turbine wakes for two floating platform types,” *Journal of Physics: Conference Series*, vol. 1452, no. 1, p. 012 034, Jan. 2020, Publisher: IOP Publishing. DOI: 10.1088/1742-6596/1452/1/012034.

[23] S. Xu, N. Wang, D. Wan, and S. Strijhak, “Large eddy simulations for floating wind turbine under complex atmospheric inflow,” 2022.

[24] A. F. P. Ribeiro, D. Casalino, and C. S. Ferreira, “Nonlinear inviscid aerodynamic effects of floating offshore wind turbine motion,” Jan. 23, 2023. DOI: 10.5194/wes-2023-3.

[25] L. Lin, K. Wang, and D. Vassalos, “Detecting wake performance of floating offshore wind turbine,” *Ocean Engineering*, vol. 156, pp. 263–276, May 15, 2018. DOI: 10.1016/j.oceaneng.2018.03.028.

[26] Z. Chen, X. Wang, Y. Guo, and S. Kang, “Numerical analysis of unsteady aerodynamic performance of floating offshore wind turbine under platform surge and pitch motions,” *Renewable Energy*, vol. 163, pp. 1849–1870, Jan. 1, 2021. DOI: 10.1016/j.renene.2020.10.096.

[27] T. T. Tran and D. H. Kim, “The aerodynamic interference effects of a floating offshore wind turbine experiencing platform pitching and yawing motions,” *Journal of Mechanical Science and Technology*, vol. 29, no. 2, pp. 549–561, Feb. 1, 2015. DOI: 10.1007/s12206-015-0115-0.

[28] T. Tran, D.-H. Kim, and B. Nguyen, “Aerodynamic interference effect of huge wind turbine blades with periodic surge motions using overset grid-based computational fluid dynamics approach,” *Journal of Solar Energy Engineering, Transactions of the ASME*, vol. 137, no. 6, 2015. DOI: 10.1115/1.4031184.

[29] C. Lienard, R. Boisard, and C. Daudin, “Aerodynamic behavior of a floating offshore wind turbine,” *AIAA Journal*, vol. 58, no. 9, pp. 3835–3847, Sep. 2020. DOI: 10.2514/1.J059255.

[30] X. Shen, J. Chen, P. Hu, X. Zhu, and Z. Du, “Study of the unsteady aerodynamics of floating wind turbines,” *Energy*, vol. 145, pp. 793–809, Feb. 15, 2018. DOI: 10.1016/j.energy.2017.12.100.

[31] R. Amaral, K. Laugesen, M. Masciola, and A. Vire, “A frequency-time domain method for annual energy production estimation in floating wind turbines,” p. 10, 2022.

[32] Y. Fang, L. Duan, Z. Han, Y. Zhao, and H. Yang, “Numerical analysis of aerodynamic performance of a floating offshore wind turbine under pitch motion,” *Energy*, vol. 192, p. 116 621, Feb. 1, 2020. DOI: 10.1016/j.energy.2019.116621.

[33] F. Porté-Agel, M. Bastankhah, and S. Shamsoddin, “Wind-turbine and wind-farm flows: A review,” *Boundary-Layer Meteorology*, vol. 174, no. 1, pp. 1–59, Jan. 2020. DOI: 10.1007/s10546-019-00473-0.

[34] A. Fontanella, I. Bayati, R. Mikkelsen, M. Belloli, and A. Zasso, “UNAFLOW: A holistic wind tunnel experiment about the aerodynamic response of floating wind turbines under imposed surge motion,” *Wind Energy Science*, vol. 6, no. 5, pp. 1169–1190, Sep. 9, 2021, Publisher: Copernicus GmbH. DOI: 10.5194/wes-6-1169-2021.

[35] S. Rockel, E. Camp, J. Schmidt, J. Peinke, R. Cal, and M. Hölling, “Experimental study on influence of pitch motion on the wake of a floating wind turbine model,” *Energies*, vol. 7, no. 4, pp. 1954–1985, Mar. 27, 2014. DOI: 10.3390/en7041954.

[36] D. Matha, M. Schlipf, and U. Stuttgart, “Challenges in simulation of aerodynamics, hydrodynamics, and mooring-line dynamics of floating offshore wind turbines,” 2011.

[37] M. Ye, H.-C. Chen, and A. Koop, “High-fidelity CFD simulations for the wake characteristics of the NTNU BT1 wind turbine,” *Energy*, vol. 265, p. 126 285, Feb. 15, 2023. DOI: 10.1016/j.energy.2022.126285.

[38] Z. Li, G. Dong, and X. Yang, “Onset of wake meandering for a floating offshore wind turbine under side-to-side motion,” *Journal of Fluid Mechanics*, vol. 934, A29, Mar. 10, 2022. DOI: 10.1017/jfm.2021.1147.

[39] L. P. Garcia, B. Conan, S. Aubrun, *et al.*, “Experimental analysis of the wake meandering of a floating wind turbine under imposed surge motion,” *Journal of Physics: Conference Series*, vol. 2265, no. 4, p. 042 003, May 2022, Publisher: IOP Publishing. DOI: 10.1088/1742-6596/2265/4/042003.

[40] N. Coudou, M. Moens, Y. Marichal, J. Van Beeck, L. Bricteux, and P. Chatelain, “Development of wake meandering detection algorithms and their application to large eddy simulations of an isolated wind turbine and a wind farm,” *Journal of Physics: Conference Series*, vol. 1037, p. 072 024, Jun. 2018. DOI: 10.1088/1742-6596/1037/7/072024.

[41] B. Schliffke, S. Aubrun, and B. Conan, “Wind tunnel study of a “floating” wind turbine’s wake in an atmospheric boundary layer with imposed characteristic surge motion,” *Journal of Physics: Conference Series*, vol. 1618, no. 6, p. 062 015, Sep. 2020, Publisher: IOP Publishing. DOI: 10.1088/1742-6596/1618/6/062015.

[42] L. Duan, Q. Sun, Z. He, and G. Li, “Wake topology and energy recovery in floating horizontal-axis wind turbines with harmonic surge motion,” *Energy*, vol. 260, p. 124 907, Dec. 1, 2022. DOI: 10.1016/j.energy.2022.124907.

[43] R. Santos Pereira, “Aerofoil aerodynamics of wind energy devices,” in *Handbook of Wind Energy Aerodynamics*, B. Stoevesandt, G. Schepers, P. Fuglsang, and S. Yuping, Eds., Cham: Springer International Publishing, 2020, pp. 1–22. DOI: 10.1007/978-3-030-05455-7_14-1.

[44] J. G. Leishman, “Challenges in modelling the unsteady aerodynamics of wind turbines,” *Wind Energy*, vol. 5, no. 2, pp. 85–132, Apr. 2002. DOI: 10.1002/we.62.

[45] M. R. Visbal and D. J. Garmann, “Analysis of dynamic stall on a pitching airfoil using high-fidelity large-eddy simulations,” *AIAA Journal*, vol. 56, no. 1, pp. 46–63, Jan. 2018. DOI: 10.2514/1.J056108.

[46] I. Bayati, M. Belloli, L. Bernini, *et al.*, “UNAFLOW project: UNsteady aerodynamics of FLOating wind turbines,” *Journal of Physics: Conference Series*, vol. 1037, no. 7, p. 072 037, Jun. 2018, Publisher: IOP Publishing. DOI: 10.1088/1742-6596/1037/7/072037.

[47] I. Bayati, M. Belloli, L. Bernini, and A. Zasso, “A formulation for the unsteady aerodynamics of floating wind turbines, with focus on the global system dynamics,” presented at the ASME 2017 36th International Conference on Ocean, Offshore and Arctic Engineering, American Society of Mechanical Engineers Digital Collection, Sep. 25, 2017. DOI: 10.1115/OMAE2017-61925.

[48] V. Leble and G. Barakos, “10-MW wind turbine performance under pitching and yawing motion,” *Journal of Solar Energy Engineering*, vol. 139, no. 4, p. 041 003, Aug. 1, 2017. DOI: 10.1115/1.4036497.

[49] T. Sebastian and M. Lackner, “Analysis of the induction and wake evolution of an offshore floating wind turbine,” *Energies*, vol. 5, no. 4, pp. 968–1000, Apr. 17, 2012. DOI: 10.3390/en5040968.

[50] S. Mancini, K. Boorsma, M. Caboni, *et al.*, “Characterization of the unsteady aerodynamic response of a floating offshore wind turbine to surge motion,” *Wind Energy Science*, vol. 5, no. 4, pp. 1713–1730, Dec. 10, 2020. DOI: 10.5194/wes-5-1713-2020.

[51] G. Schepers, “Pragmatic models: BEM with engineering add-ons,” in *Handbook of Wind Energy Aerodynamics*, B. Stoevesandt, G. Schepers, P. Fuglsang, and S. Yuping, Eds., Cham: Springer International Publishing, 2020, pp. 1–44. DOI: 10.1007/978-3-030-05455-7_19-1.

[52] J. N. Sørensen, W. Z. Shen, and X. Munduate, "Analysis of wake states by a full-field actuator disc model," *Wind Energy*, vol. 1, no. 2, pp. 73–88, 1998. DOI: 10.1002/(SICI)1099-1824(199812)1:2<73::AID-WE12>3.0.CO;2-L.

[53] J. Dong and A. Viré, "Comparative analysis of different criteria for the prediction of vortex ring state of floating offshore wind turbines," *Renewable Energy*, vol. 163, pp. 882–909, Jan. 1, 2021. DOI: 10.1016/j.renene.2020.08.027.

[54] J. Cruz and M. Atcheson, Eds., *Floating Offshore Wind Energy: The Next Generation of Wind Energy*, Green Energy and Technology, Cham: Springer International Publishing, 2016. DOI: 10.1007/978-3-319-29398-1.

[55] J. Dong and A. Viré, "The aerodynamics of floating offshore wind turbines in different working states during surge motion," *Renewable Energy*, vol. 195, pp. 1125–1136, Aug. 2022. DOI: 10.1016/j.renene.2022.06.016.

[56] C. Ferreira, W. Yu, A. Sala, and A. Viré, "Dynamic inflow model for a floating horizontal axis wind turbine in surge motion," *Wind Energy Science*, vol. 7, no. 2, pp. 469–485, Mar. 8, 2022, Publisher: Copernicus GmbH. DOI: 10.5194/wes-7-469-2022.

[57] R. Kyle, Y. C. Lee, and W.-G. Früh, "Propeller and vortex ring state for floating offshore wind turbines during surge," *Renewable Energy*, vol. 155, pp. 645–657, Aug. 1, 2020. DOI: 10.1016/j.renene.2020.03.105.

[58] R. Kyle and W.-G. Früh, "The transitional states of a floating wind turbine during high levels of surge," *Renewable Energy*, vol. 200, pp. 1469–1489, Nov. 1, 2022. DOI: 10.1016/j.renene.2022.10.034.

[59] R. Bergua, A. Robertson, J. Jonkman, *et al.*, "OC6 project phase III: Validation of the aerodynamic loading on a wind turbine rotor undergoing large motion caused by a floating support structure," *Wind Energy Science Discussions*, pp. 1–33, Aug. 23, 2022, Publisher: Copernicus GmbH. DOI: 10.5194/wes-2022-74.

[60] J. N. Sōrensen and W. Z. Shen, "Numerical modeling of wind turbine wakes," *Journal of Fluids Engineering*, vol. 124, no. 2, pp. 393–399, Jun. 1, 2002. DOI: 10.1115/1.1471361.

[61] F. Houtin-Mongrolle, L. Bricteux, P. Benard, G. Lartigue, V. Moureau, and J. Reveillon, "Actuator line method applied to grid turbulence generation for large-eddy simulations," *Journal of Turbulence*, vol. 21, no. 8, pp. 407–433, Aug. 2, 2020, Publisher: Taylor & Francis _eprint: https://doi.org/10.1080/14685248.2020.1803495. DOI: 10.1080/14685248.2020.1803495.

[62] R. Stanly, L. A. Martínez-Tossas, S. H. Frankel, and Y. Delorme, "Large-eddy simulation of a wind turbine using a filtered actuator line model," *Journal of Wind Engineering and Industrial Aerodynamics*, vol. 222, p. 104 868, Mar. 1, 2022. DOI: 10.1016/j.jweia.2021.104868.

[63] W. Z. Shen, R. Mikkelsen, J. N. Sørensen, and C. Bak, "Tip loss corrections for wind turbine computations," *Wind Energy*, vol. 8, no. 4, pp. 457–475, 2005. DOI: 10.1002/we.153.

[64] L. A. Martínez-Tossas and C. Meneveau, "Filtered lifting line theory and application to the actuator line model," *Journal of Fluid Mechanics*, vol. 863, pp. 269–292, Mar. 25, 2019. DOI: 10.1017/jfm.2018.994.

[65] Z. Gao, Y. Li, T. Wang, *et al.*, "Modelling the nacelle wake of a horizontal-axis wind turbine under different yaw conditions," *Renewable Energy*, vol. 172, pp. 263–275, Jul. 2021. DOI: 10.1016/j.renene.2021.02.140.

[66] H. Sarlak, C. Meneveau, and J. N. Sørensen, "Role of subgrid-scale modeling in large eddy simulation of wind turbine wake interactions," *Renewable Energy*, vol. 77, pp. 386–399, May 1, 2015. DOI: 10.1016/j.renene.2014.12.036.

[67] M. J. Churchfield, S. Lee, J. Michalakes, and P. J. Moriarty, "A numerical study of the effects of atmospheric and wake turbulence on wind turbine dynamics," *Journal of Turbulence*, vol. 13, N14, Jan. 2012. DOI: 10.1080/14685248.2012.668191.

[68] S. Lee, M. Churchfield, F. Driscoll, *et al.*, "Load estimation of offshore wind turbines," *Energies*, vol. 11, no. 7, p. 1895, Jul. 20, 2018. DOI: 10.3390/en11071895.

[69] S. Xiao and D. Yang, “Large-eddy simulation-based study of effect of swell-induced pitch motion on wake-flow statistics and power extraction of offshore wind turbines,” *Energies*, vol. 12, no. 7, p. 1246, Apr. 1, 2019. DOI: 10.3390/en12071246.

[70] M. Lin and F. Porté-Agel, “Large-eddy simulation of a wind-turbine array subjected to active yaw control,” *Wind Energy Science*, vol. 7, no. 6, pp. 2215–2230, Nov. 8, 2022, Publisher: Copernicus GmbH. DOI: 10.5194/wes-7-2215-2022.

[71] J. Smagorinsky, “GENERAL CIRCULATION EXPERIMENTS WITH THE PRIMITIVE EQUATIONS: I. THE BASIC EXPERIMENT,” *Monthly Weather Review*, vol. 91, no. 3, pp. 99–164, Mar. 1, 1963, Publisher: American Meteorological Society Section: Monthly Weather Review. DOI: 10.1175/1520-0493(1963)091<0099:GCEWTP>2.3.CO;2.

[72] M. Germano, U. Piomelli, P. Moin, and W. H. Cabot, “A dynamic subgrid□scale eddy viscosity model,” *Physics of Fluids A: Fluid Dynamics*, vol. 3, no. 7, pp. 1760–1765, Jul. 1991. DOI: 10.1063/1.857955.

[73] D. K. Lilly, “A proposed modification of the germano subgrid□scale closure method,” *Physics of Fluids A: Fluid Dynamics*, vol. 4, no. 3, pp. 633–635, Mar. 1992, Publisher: American Institute of Physics. DOI: 10.1063/1.858280.

[74] F. Nicoud, H. B. Toda, O. Cabrit, S. Bose, and J. Lee, “Using singular values to build a subgrid-scale model for large eddy simulations,” *Physics of Fluids*, vol. 23, no. 8, p. 085 106, Aug. 2011. DOI: 10.1063/1.3623274.

[75] F. Nicoud and F. Ducros, “Subgrid-scale stress modelling based on the square of the velocity gradient tensor,” *Flow, Turbulence and Combustion*, vol. 62, no. 3, pp. 183–200, Sep. 1, 1999. DOI: 10.1023/A:1009995426001.

[76] A. W. Vreman, “An eddy-viscosity subgrid-scale model for turbulent shear flow: Algebraic theory and applications,” *Physics of Fluids*, vol. 16, no. 10, pp. 3670–3681, Oct. 2004, Publisher: American Institute of Physics. DOI: 10.1063/1.1785131.

[77] U. Ciri, M. V. Salvetti, K. Carrasquillo, C. Santoni, G. V. Iungo, and S. Leonardi, “Effects of the subgrid-scale modeling in the large-eddy simulations of wind turbines,” in *Direct and Large-Eddy Simulation X*, D. G. Grigoriadis, B. J. Geurts, H. Kuerten, J. Fröhlich, and V. Armenio, Eds., vol. 24, Series Title: ERCOFTAC Series, Cham: Springer International Publishing, 2018, pp. 109–115. DOI: 10.1007/978-3-319-63212-4_13.

[78] M. Abkar, “Impact of subgrid-scale modeling in actuator-line based large-eddy simulation of vertical-axis wind turbine wakes,” *Atmosphere*, vol. 9, no. 7, p. 257, Jul. 2018, Number: 7 Publisher: Multidisciplinary Digital Publishing Institute. DOI: 10.3390/atmos9070257.

[79] P. K. Jha, M. J. Churchfield, P. J. Moriarty, and S. Schmitz, “Guidelines for volume force distributions within actuator line modeling of wind turbines on large-eddy simulation-type grids,” *Journal of Solar Energy Engineering*, vol. 136, no. 3, p. 031 003, Aug. 1, 2014. DOI: 10.1115/1.4026252.

[80] Z. Li and X. Yang, “Large-eddy simulation on the similarity between wakes of wind turbines with different yaw angles,” *Journal of Fluid Mechanics*, vol. 921, A11, Aug. 25, 2021. DOI: 10.1017/jfm.2021.495.

[81] A. Sheidani, S. Salavatidezfouli, G. Stabile, and G. Rozza, “Assessment of URANS and LES methods in predicting wake shed behind a vertical axis wind turbine,” *Journal of Wind Engineering and Industrial Aerodynamics*, vol. 232, p. 105 285, Jan. 1, 2023. DOI: 10.1016/j.jweia.2022.105285.

[82] E. Daniele, “CFD for wind turbine simulations,” in *Handbook of Wind Energy Aerodynamics*, B. Stoevesandt, G. Schepers, P. Fuglsang, and S. Yuping, Eds., Cham: Springer International Publishing, 2021, pp. 1–53. DOI: 10.1007/978-3-030-05455-7_21-1.

[83] F. Taruffi, F. Novais, and A. Viré, “An experimental study on the aerodynamic loads of a floating offshore wind turbine under imposed motions,”

[84] L. E. M. Lignarolo, D. Ragni, C. Krishnaswami, Q. Chen, C. J. Simão Ferreira, and G. J. W. van Bussel, "Experimental analysis of the wake of a horizontal-axis wind-turbine model," *Renewable Energy*, Special issue on aerodynamics of offshore wind energy systems and wakes, vol. 70, pp. 31–46, Oct. 1, 2014. DOI: 10.1016/j.renene.2014.01.020.

[85] A. Fontanella, G. Da Pra, and M. Belloli, "Integrated design and experimental validation of a fixed-pitch rotor for wind tunnel testing," *Energies*, vol. 16, no. 5, p. 2205, Feb. 24, 2023. DOI: 10.3390/en16052205.

[86] V. Moureau, P. Domingo, and L. Vervisch, "Design of a massively parallel CFD code for complex geometries," *Comptes Rendus Mécanique*, High Performance Computing, vol. 339, no. 2, pp. 141–148, Feb. 1, 2011. DOI: 10.1016/j.crme.2010.12.001.

[87] S. Zeoli, G. Balarac, P. Bénard, G. Georis, F. Houtin-Mongrolle, and L. Bricteux, "Large eddy simulation of wind turbine wakes using adaptative mesh refinement," *Journal of Physics: Conference Series*, vol. 1618, no. 6, p. 062 056, Sep. 2020, Publisher: IOP Publishing. DOI: 10.1088/1742-6596/1618/6/062056.

[88] F. Houtin-Mongrolle, P. Benard, G. Lartigue, and V. Moureau, "A level-set framework for the wind turbine wake analysis: From high-fidelity unsteady simulations to 1d momentum theory," *Journal of Physics: Conference Series*, vol. 1934, no. 1, p. 012 011, May 2021, Publisher: IOP Publishing. DOI: 10.1088/1742-6596/1934/1/012011.

[89] S. Gremmo, E. Muller, F. Houtin-Mongrolle, B. Duboc, and P. Bénard, "Rotor-wake interactions in a wind turbine row: A multi-physics investigation with large eddy simulation," *Journal of Physics: Conference Series*, vol. 2265, no. 2, p. 022 020, May 2022, Publisher: IOP Publishing. DOI: 10.1088/1742-6596/2265/2/022020.

[90] A. S. M. Al-Obaidi and G. Madivaanan, "Investigation of the blockage correction to improve the accuracy of taylor's low-speed wind tunnel," *Journal of Physics: Conference Series*, vol. 2222, no. 1, p. 012 008, May 1, 2022. DOI: 10.1088/1742-6596/2222/1/012008.

[91] K. Takeda and M. Kato, "Wind tunnel blockage effects on drag coefficient and wind-induced vibration," *Journal of Wind Engineering and Industrial Aerodynamics*, vol. 42, no. 1, pp. 897–908, Oct. 1, 1992. DOI: 10.1016/0167-6105(92)90096-S.

[92] C. Geuzaine and J.-F. Remacle, "Gmsh: A three-dimensional finite element mesh generator with built-in pre- and post-processing facilities," 2009.

[93] S. B. Pope, "Ten questions concerning the large-eddy simulation of turbulent flows," *New Journal of Physics*, vol. 6, pp. 35–35, Mar. 16, 2004. DOI: 10.1088/1367-2630/6/1/035.

[94] N. D. Katopodes, "Viscous fluid flow," in *Free-Surface Flow*, Elsevier, 2019, pp. 324–426. DOI: 10.1016/B978-0-12-815489-2.00005-8.

[95] E. Mercker and J. Wiedemann, "On the correction of interference effects in open jet wind tunnels," *SAE Transactions*, vol. 105, pp. 795–809, 1996, Publisher: SAE International.

[96] B. Schliffke, "Experimental characterisation of the far wake of a modelled floating wind turbine as a function of incoming swell," Ph.D. dissertation, 2021.

Acknowledgements

First, I want to thank my supervisor Axelle Viré for her availability and her essential feedback during this work, but also for this great opportunity of working on such an compelling topic.

It was very interesting to exchange with Federico and Felipe on the experiment and the discrepancies with my numerical results. I want to particularly thank Federico for giving of his time and providing quality insights.

My thanks also go to Ricardo for his precious help on the code and its difficult installation on the cluster.

I would also like to express my gratitude towards Dominic von Terzi for his substantial feedback during the mid-term meeting and for chairing the committee, and to Stefan Hickel for examining the defence.

I am also grateful to TU Delft and the FPT department for enabling such an opportunity and granting access to the cluster, and to the CORIA laboratory for providing access to the YALES2 code.

Finally, I want to thank my friends and particularly Guillaume, Grégoire and Etienne, for their support and for making those months of focused work much more enjoyable.